CARDIFF UNIVERSITY
SCHOOL OF ENGINEERING

Non-Aqueous Shale Gas Recovery System

By
Zaid Maan H. Al-Dulaimi

Institute of Energy

Supervisors:
Prof Philip J Bowen
Dr Agustin Valera-Medina

`A Thesis submitted to Cardiff University`
`For the Degree of Doctor of Philosophy`
`In Mechanical Engineering, 2017`

DECLARATION

This work has not been submitted in substance for any other degree or award at this or any other university or place of learning, nor is being submitted concurrently in candidature for any degree or other award.

Signed ……………………………………. (Candidate)   Date …............................

STATEMENT 1

This thesis is being submitted in partial fulfilment of the requirements for the degree of PhD

Signed ……………………………………. (Candidate)   Date …............................

STATEMENT 2

This thesis is the result of my own independent work/investigation, except where otherwise stated, and the thesis has not been edited by a third party beyond what is permitted by Cardiff University's Policy on the Use of Third Party Editors by Research Degree Students. Other sources are acknowledged by explicit references. The views expressed are my own.

Signed ……………………………………. (Candidate)   Date …............................

STATEMENT 3

I hereby give consent for my thesis, if accepted, to be available online in the University's Open Access repository and for inter-library loan, and for the title and summary to be made available to outside organisations.

Signed ……………………………………. (Candidate)   Date …............................

ACKNOWLEDGMENTS

First and foremost, I would like to praise and thank **Allah** for helping me to complete all requirements for the degree.

I would like to express my sincere gratitude to my supervisors, **Prof. Philip Bowen** and **Doctor Agustin Valera-Medina** for their continuous support and guidance through this study.

My great thanks to all technicians of the workshop for their help and technical support. Special recognition to **Mr Malcolm Seaborne**, whose technical knowledge contributed to the successful completion of this work.

I would like to thank the staff of School of Engineering, the staff of the Gas Turbine Research Centre (GTRC), and the staff of the Research Office, for all the help over the last few years. Big thanks to my friends **Dr Luay Al-Ansari** and **Mr Noor Al-Hasnawi**, University of Kufa, for their help and valuable feedback and ideas through my works. Thanks and gratitude are also given to my friends and colleagues who provide a very enjoyable and motivating environment.

The completion of my degree would have been impossible without the help and support of the **Iraqi Government**, and many thanks to the staff of the **Iraqi cultural attaché** in London.

My deepest thanks, love and gratitude for all of my family, parents, brothers, sisters and extraordinary thanks for my **wife** and my lovely children, **Mohammed**, **Sarah** and **Lina** for their understanding and support.

ABSTRACT

High European energy demands, the difference in prices amongst Europe and ambitious gas producers, have produced a scenario of high competition in a region that suffers a lack of fossil resources still required for energy generation. Therefore, other sources are under the scope of various countries to mitigate these issues. Shale gas is one fuel that presents a scenario that would decrease European dependence on imported gas. Although shale gas production is unlikely to give the energy security desired to the whole Europe, it would make a difference for the communities that will adopt it. However, shale gas has acquired a bad reputation with the public, mainly because of its extraction methods. This bad reputation is attributed to hydraulic fracturing, technology well-known as fracking, and its risks associated towards air and water pollution. Therefore, companies, institutions and governments are looking for other alternative methods of extraction with more environmentally friendly processes.

Producing extensive high-pressure pulse waves at the base of the wellbore by using detonation is a promising potential technique for shale gas extraction. A fundamental study of deflagration to detonation transition using recirculated shale gas formation with pure oxygen as an oxidiser has been studied to design a system with lower DDT distance and higher pressure waves.

Three proposed cases of UK shale gas composition were studied. Chemical equilibrium software GASEQ and chemical kinetic software CHEMKIN-PRO were used to estimate the product parameters. Results showed that the effect produced by diluents, such as carbon dioxide, are eliminated by the use of higher hydrogen content carbon-to-hydrogen species for the three cases proposed. OpenFOAM CFD was used to calculate the deflagration to detonation transition parameters in stoichiometric hydrogen air mixtures to evaluate different obstacle geometries on the transition phenomenon to improve the detonation process. The shape and layout of obstacles were found to have a significant effect on flame acceleration, and subsequent detonation propagation. The interaction of transverse pressure waves generated at the obstructions governs the propagation mechanism. The transverse waves and its frequency appear to play a pivotal role in supporting the detonation wave.

It was found that rectangular shape obstacles reduce the reaction time, while triangular ones achieved detonation with the minimum run-up distance. On the other hand, semi-circular shape obstacles generate the highest pressure in a detonation tube. The outcome from numerical calculations and CFD were the guide to construct an experimental rig of 21.2mm diameter and 1500mm length tube with different obstacle configurations to demonstrate the concept of pulse detonation for shale rock cracking.

Experimental work has been performed to determine the potential of shale gas production in the Dullais Valley, South of Wales. It was found through several tests using BS standard volatile analyses, Transmission Electron Microscopy and pyrolysis RockEval evaluation that the potential of extraction in this region is fair, with similar concentrations of pyrite but with low energy content compared to those resources located in the Midlands and Yorkshire. However, the use of controlled pulse detonation could be the ideal technology for extraction in Wales, as low sulphur (S) content will produce lower unwanted emissions, with a process that can promote opening of pores and further gasification of oil based molecular, with a subsequent increase in shale gas production, topic that requires further research.

Finally, a 2-dimensional simulation was performed using ANSYS Parameter Design Language (APDL) to investigate the effect of pressure pulse generated by the detonation tube on a pre-crack. Results showed that the layer close to the applied load will be displaced, which means that it will be smashed. The maximum Von Mises stresses were found to concentrate at the perforating hole corners, while the region immediately after the crack tip is susceptible to compression stresses. The Same behaviour was found for the stress intensity factor. According to that, it is believed that the cracks will propagate diagonally from the perforating hole base.

Therefore, the current work has theoretically demonstrated the technology for shale gas recovery, with an optimised geometry consistent of internal obstacles, for a region with potential for shale gas exploitation.

Table of Contents

List of Figures

List of Tables

Nomenclature

Alphabetic Symbols

a	Crack length	*m*
c	Speed of sound	*m/s*
E	Modulus of elasticity	*N/m*^{2}
h	Enthalpy	*kJ/kg*
HI	Hydrogen Index	-
K_I	Stress intensity factor	*Pa.m*$^{1/2}$
K_{IC}	Critical stress intensity factor (Fracture Toughness)	*Pa.m*$^{1/2}$
M	Mach Number	-
M_w	Molecular weight	*kg/mol*
p	Pressure	*Pa*
PI	Production Index	-
q	Heat release per unit mass	*kJ/kg*
r	Pipe radius	*m*
R	Gas constant	*kJ/kg.K*
S1	Amount of hydrocarbons released at initial heating	*mg HC/g rock*
S2	Amount of hydrocarbons produced upon pyrolytic degradation of the remaining organic matter in the rock	*mg HC/g rock*
S3	Amount of carbon dioxide generated during the pyrolysis	-
S_l	Laminar burning velocity	*m/s*
T	Temperature	*K*
t_{sphere}	Time when the flame front changes from spherical to finger shaped	*s*
t_{tulip}	Time when the tulip flame happens	*s*
$t_{\mathbf{wall}}$	Time when the flame reaches the pipe wall	*s*
u	Velocity	*m/s*
w	Perforating depth	*m*
Z_{wall}	Axial position of the flame front when it first touches the pipe side wall	*m*

Greek symbols

α	Thermal expansion ratio	-
γ	Specific heat ratio	-
λ	Detonation cell width	*m*
ν	Poisson's ratio	-
ρ	Density	*kg/m*$^{\mathbf{3}}$
σ	Nominal stress	*N/m*^{2}
σ_T	Tensile strength	*N/m*^{2}
τ	Shear stress	*N/m*^{2}
Φ	Equivalence ratio	-

List of abbreviations

APDL	ANSYS Parameter Design Language
BSP	British standard pipe
CFD	Computational fluid dynamics
C-J theory	The Chapman-Jouguet Theory
COD	Crack opening displacement
COSHH	Control of Substances Hazardous to Health
DDT	Deflagration to detonation transition
DSEAR	Dangerous Substance and Explosive Atmosphere Regulations
EDS	Energy Dispersive X-ray Spectrometry
EPS	Explosive/Propellant systems
GRI-Mech	Gas Research Institute mechanism
HAZOP	Hazard and Operability Study
HLLC	Harten-Lax-van Leer-Contact
HRTEM	High-Resolution Transmission Electron Microscope
HSE	Health and Safety Executive
LEFM	Linear elastic fracture mechanics
LEL	Lower explosive limit
LES	Large Eddy Simulation
MAWP	Mean allowing working pressure
NPT	National pipe tapered
OpenFOAM	Open Field Operation And Manipulation
P&ID	Piping and instrumentation diagrams
RANS	Reynolds Averaging Navier-Stokes
RAS	Reynolds-Average Stress
ROI	Return on investment
SDD	Silicon Drift Detector
SIF	Stress intensity factor
spf	Shoots per foot
STEM	Scanning transmission electron microscopy
tcf	Trillion (10^{12}) cubic feet
TOC	Total organic Carbon
UEL	Upper explosive limit
URANS	Unsteady Reynolds Averaging Navier-Stokes
ZND theory	Zeldovich , von Neumann and Doring theory

CHAPTER ONE

Introduction

1.1 General Introduction

The combination of horizontal drilling and hydraulic fracturing were the main reasons for the shale revolution overran United State over the last decade. Shale gas production increases have decreased both natural gas wholesale prices and dependability on imports, which led to a significant competitive to manufacturers.

Adoption of such technology in Europe could open many horizons. Economically, beside its direct impact on the prices, as it will lower wholesale prices and potentially lower household gas and electricity prices, shale gas industry could trigger the creation of significant new jobs. Europe’s economy could also benefit from domestic shale gas production as it generates vast sums of tax revenues. Environmentally, as reducing greenhouse gas emission is one of the most essential goal globally, natural gas extracted from shale will reduce emissions in a cost-competitive way.

Furthermore, the security of EU gas supply has been a priority since the last decade. Besides energy efficiency and completion of the internal energy market, the increase in domestic energy production in the EU will diversify supplier countries and routes. Shale gas could partially compensate for declining conventional gas production provided.

However, current technologies lead to the usage of fracking, a controversial hydraulic technique that has suffered considerable criticism in Europe. Therefore, companies and institutions are looking for other alternatives with more environmentally friendly processes. One of these processes uses Explosive/Propellant systems (EPS) to crack the rock avoiding waste by-products. However, using explosives in shale wells needs considerable improvement to achieve the production rates obtained with fracking. On the other hand, the detonation phenomenon is known since the end of the 19th century. This technique has high efficiencies compared to deflagration (combustion at low velocities) with high potential to compete with fracking in terms of shale recovery and EPS in its low environmental impact.

1.2 Natural Gas and Oil

Natural gas and oil share many similarities, these two hydrocarbons, which among others referred to as fossil fuels, are essential to modern lifestyle. Both of conventional gas and oil are less dense than water, this characteristic allows them pour up through earth's geological layers and being substituted by ground water until they found a geological layer consists of impermeable stones does not allow them to pass through. While oil, which is heavier and more complex carbon formation than natural gas, always comes out from the underground, natural gas comes from different sources. Often it is found associated with oil fields, also it is found in what is called natural gas fields by its own. Nevertheless, natural gas can be produced through natural processes.

On the other hand, divergence points between those hydrocarbons over their similarities. The place where the difference is most obvious is the compressibility. While oil is non-soluble, in either water or alcohol, unctuous flammable incompressible substance, gas is lightweight gasiform compressible fluid. The prices of gas beside its environmental impact made many industrials applications replacing oil with gas as main fuels. Gas is cheaper and more reliable in being imported from one place to other [1]. In addition, the gas can be regarded as less hazardous to the environment as it burns brighter, hotter and cleaner, so it is a smoke free heat and light source [2].

1.3 Why EU needs more gas?

There are many factors influencing fossil gas production. One of the most important factors is world energy demand, which is related mainly to population and income growth. Primary energy demand will increase by 41% between 2012 and 2035 according to Energy Outlook 2035. Industry represents the main sector for energy consumption. Residential, services and agriculture (referred as other) represent the second energy consumer with energy mainly consumed as electricity. The third sector represented by transport [3], as seen in figure 1.1.

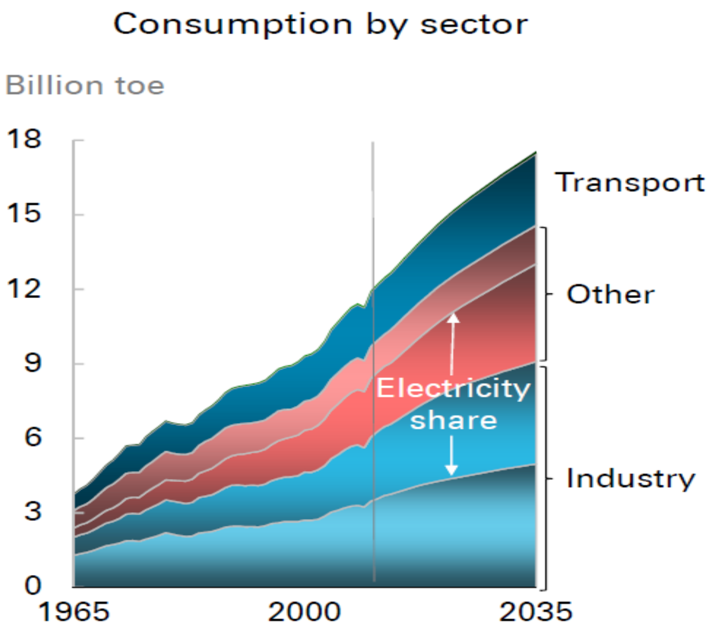

Figure 1.1. Energy consumption by sector [3]**.**

Another factor influencing gas production is the difference in prices between Europe and gas producer countries, which have a trading partnership with Europe. The European Commission paper states that the EU industrial gas prices are three to four times higher than those in the US or Russian prices, and 12% higher than in China [4]. This has been mainly driven by a shale gas revolution. The growth of shale gas production in addition to the global economic downturn at the beginning of twenty first century led to that difference in prices especially in the US, as it is illustrated in figure 1.2.

Undoubtedly, renewable energy constitutes an important solution for the EU energy. However renewable energy share represented only 8% of the total primary energy consumption in 2010 [5]. While this share is planned increase to 25% by 2030 [6], about 26% of Europe’s energy demands will be covered by gas by this time [3], figure 1.3.

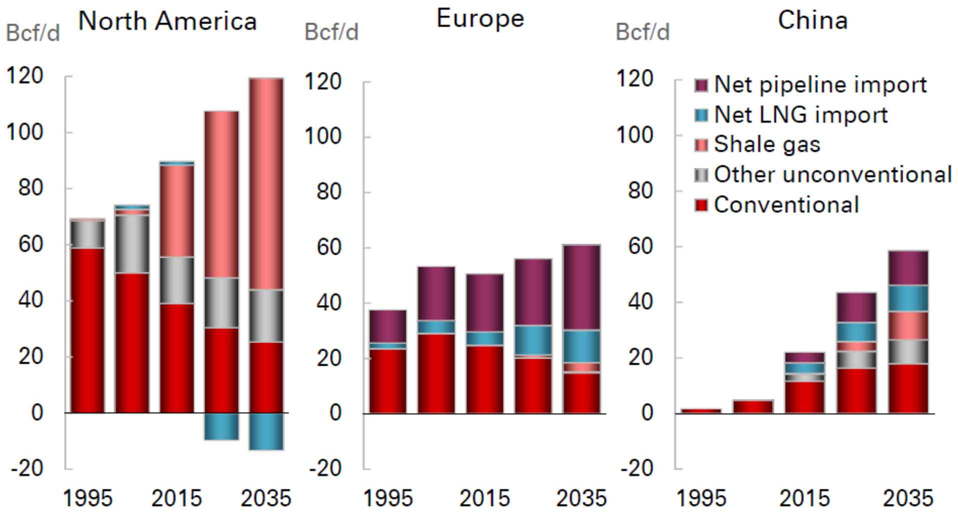

Figure 1.2. Source of gas supply for three different regions [3]**.**

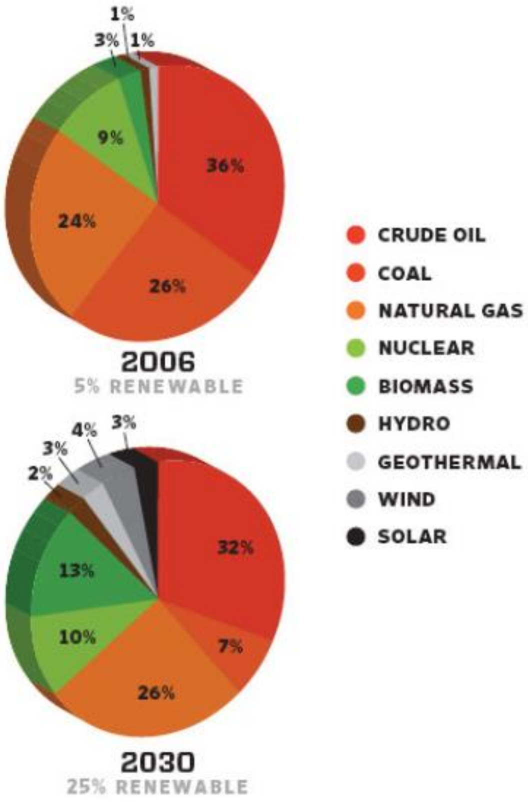

Figure 1.3. Primary energy consumption source [6]

1.4 Shale Gas

Generally speaking, gas has been divided into two types, the first is conventional gas and the second is unconventional gas. Conventional gas has been described as the gas that can be extracted by the wells' natural pressure. Natural gas, generally, could be considered as cleaner-burning when it's compared with coal and oil. The first commercial natural gas well was drilled in 1821 in the United States, this well produced gas until 1858. By the last decade of the nineteenth century, intrastate pipelines and municipal natural gas distribution systems have been developed[7].

Different techniques would probably be used when the wells' natural pressure go too low, after the consumption of fields, like injection of water or gas in the wells, but these wells will still produce conventional gas. When the drilling is not enough to make the gas flow up the well, and other recovery processes are required to extract the gas, that gas is called unconventional gas. Shale gas is natural gas trapped within shale formation deep underground. Shale rocks are fine-grained sedimentary rocks formed from deposits of mud silt, clay and organic matter.

Shale gas primarily consists of methane and small amounts of ethane, propane and butane with carbon dioxide and other gases. Shale gas extraction is linked to two key technologies, horizontal drilling and hydraulic fracturing, Fracking. Conventional and unconventional gas is essentially the same, the term unconventional simply refers to the extraction method and rock formation [8].

1.5 Economic Impact

The economic assessment of domestic shale gas production can be described into two parts. The first is the direct economic impact by reducing dependence on gas imports. In 2012, the Europe Union dependency rate on imported gas raised to 65.8% from only 50.9% a decade before [9]. As such dependability can rise to 89% by 2035, domestic production can reduce it to between 62% to 78% [10].

The other part of the domestic production is the indirect impacts. This part contains many positive aspects which are in the interest of communities that will host gas exploration and production, creating employment for the local work force as well as its impact on energy market [11]. Compared to new employment opportunities provided by the shale gas production in the US, which was about 600,000 in 2015 and expected to rise to 870,000 by 2035, similar opportunities have been estimated to be created in Europe. This might even be as high as 800,000 new jobs by 2035 and up to 1.1 million by 2050 [11]. The demand for infrastructure and construction services will be triggered by domestic gas production increase. This expansion will directly affect the gas extraction sector and indirectly most other industries, which will lead to create more employment opportunities [10].

Tax revenues are one of the indirect economic impacts of shale gas production. Taxes will be paid by the gas extraction industry when wells are drilled, pipelines are constructed, and production facilities are built and operated. In addition, taxes will be paid by labour force and through energy consumption [10].

Furthermore, energy prices in Europe will be affected by shale gas production. A 6% to 14% of gas prices and 3% to 8% of electricity prices could be reduced in the case of high shale gas production [10]. This, in turn, will influence Europe's business competitiveness, as it will reduce about 1% to 10% of industrial production costs, which represents the energy cost [11].

1.6 Environmental Impact

Nowadays, environment represents a major concern for all communities, especially when energy consumption and its accompanying pollutants emissions have increased substantially in recent decades. There are many different kinds of environmental pollution, but the ones related to fossil fuels exceed any other pollution sources. Greenhouse effects, acid rain, and air pollution are the most pollution issues related to fossil fuels burning [12].

The main pollutants emitted from fossil fuels combustion consist of carbon dioxide, carbon monoxide, nitrogen oxides, sulphur dioxide and other particulates like ashes particles. Natural gas is the cleanest burning of all fossil fuels, as it is shown in figure 1.4, remarkably lower levels of almost all pollutants are emitted by gas combustion, with virtually no ash or particulate matter [13].

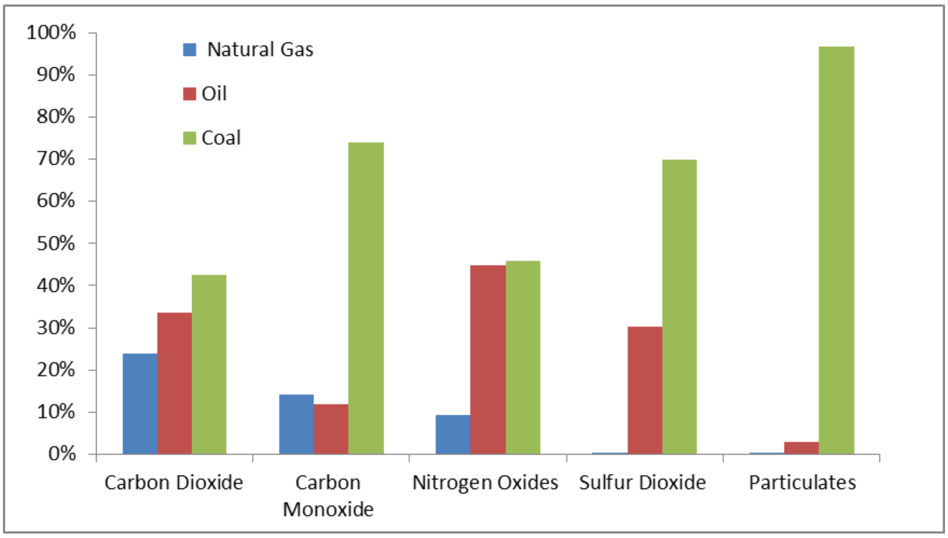

Figure 1.4. Fossil fuel emission levels [13]

1.6.1 Greenhouse

Greenhouse effects represent the main causes of climate change. Solar radiation is the main natural source of energy as it stems from the sun towards the Earth through atmospheric gases in the form of visible short-wave light, long heat waves and some of the ultraviolet waves that cannot be absorbed by the ozone. The ground absorbs this energy, which causes an increase in its temperature, and starts emitting it to the atmosphere as long thermal waves. The gases in the atmosphere absorb these waves and retain the heat, then it re-radiates it back to the Earth, leading to increased ground surface temperature [14].

The gases that absorb thermal waves are called greenhouse gases. Water vapour, carbon dioxide and ozone are the main greenhouse gases. Figure 1.5 shows the individual contribution of each greenhouse gas absorber. Water vapour contributes to the main part of the greenhouse effect with 60% share. The second most important greenhouse gas is carbon dioxide, which partakes of 26% [15]. Any hydrocarbon burning results in carbon dioxide and water vapour, and since this water vapour cannot be compared to the amount evaporated by oceans, then the crucial rules here are played by carbon dioxide emission [15].

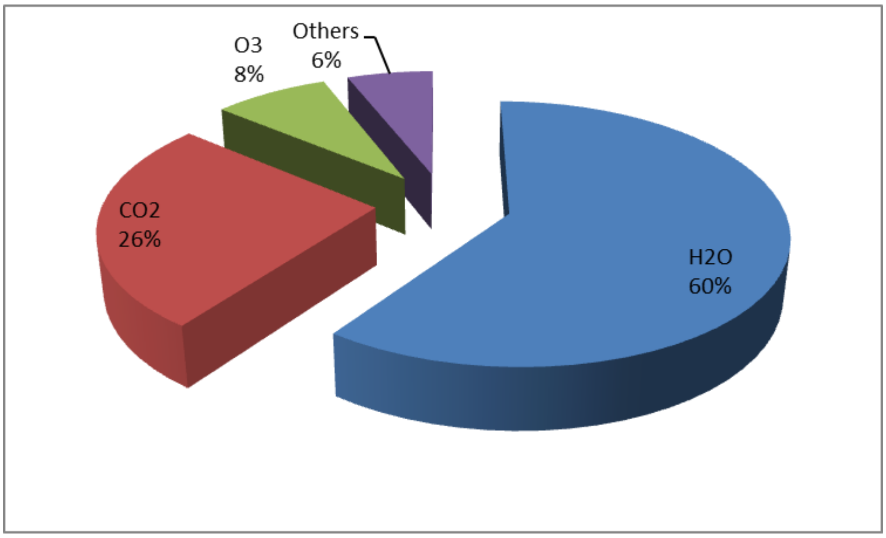

Figure 1.5 The individual contribution of each greenhouse gas absorber [15]

Natural gas combustion emits 29% less carbon dioxide than oil and 43% less than coal to produce the same amount of energy released [13]. In the United States, carbon dioxide emissions were in the lowest rates in 2012 since 1994, figure 1.6. Coal burning reduction was the main reason. Coal combustion based power generation were shifted to natural gas power generation due to declining prices, mainly because of shale gas production [16]. In Europe, the greenhouse gases emissions could be reduced (by 41% to 49%) in case that shale gas power generation substitute coal based generation[17].

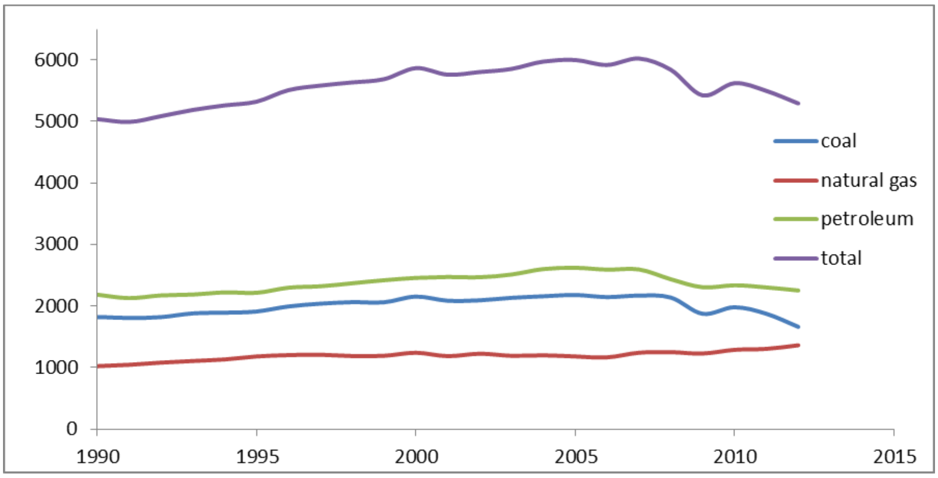

Figure 1.6 The Annual energy-related carbon emissions (metric tonnes of carbon dioxide) [16]

1.6.2 Acid Rain

Acid rain is produced from dissolved sulphuric acid and nitric acid in the atmospheric water droplets. Beside carbon dioxide and water vapour, hydrocarbons combustion, especially coal and oil, emit certain amounts of sulphur dioxide and nitrogen oxides. These two oxides undergo, in certain circumstances, chemical reactions with the atmospheric substances to become acids and dissolved in water droplets. These water droplets in turn eventually may fall to the ground as acidic rain [18].

The greatest effect of acid rain is its impact on bodies of water and aquatic environments, besides its impact on soil and plants. Acid rain dissolves aluminium out of the soil and releases it as aluminium sulphate or aluminium nitrate. These can be absorbed by the root of trees which cause direct damages to it, also preventing trees from absorbing calcium and magnesium, which are basic to the nutrition. Finally, these aluminium compounds find its way from soil to lakes and streams making the water toxic to aquatic animals [19].

As natural gas emits substantially no sulphur dioxide and about 17% nitrogen oxides of what oil or coal emit, then natural gas guarantees less pollutants emission caused by acid rain.

1.6.3 Air Pollution

Although the greenhouse effect influences environment and economic, and acid rain impacts aquatic life and plants, it takes greater media and environmental attention than air pollution which can play a pivotal role, in many direct ways, on human beings by making them suffering through illness.

In addition to the main greenhouse gases and the gases producing acid rain, there are other pollutants emitted by fossil fuels. Troposphere ozone, which is a major part of smog with fine particles, is responsible for a number of health issues especially the ones related to the respiratory system. It can also hurt plants and crops. Ozone is not a direct product of fossil fuel combustion, but is produced by mixing nitrogen oxides with organic chemicals that have a high vapour pressure at room temperature, known as volatile organic compounds. In the presence of sunlight, smog is formed with problems that are the worst in the summertime [20]. Volatile organic compounds are emitted to the atmosphere either naturally or human-induced. Fossil fuel deposits, volcanoes, vegetation and even trees represent natural sources of volatile organic compounds. Transportations exhaust, mainly gasoline and kerosene engines ones, with some building and household materials, like cleaners, disinfectants, paints and others, represent the main man-made sources of volatile organic compounds [21].

As it was mentioned above, natural gas emits only 17% of nitrogen oxides that coal and oil emit with substantially no particulate matter, so it does not contribute notably to smog creation [13]. Natural gas could be used instead of other more polluting fossil fuel in the summertime, when the temperature is higher and smog is more likely to be formed.

Carbon monoxide could be a fatal gas when it is highly concentrated, principally because it is unseen and non-sniffed. Carbon monoxide prevents the body to have enough oxygen making people feel dizzy and tired. Engines release carbon monoxide when burning fossil fuels. Emissions are higher if engines do not work properly and the mixture is rich with fuel. Natural gas emits more carbon monoxide than oil, 21% more, but it emits 81% less than what coal does [13].

1.7 Gas vs. Oil and Coal

Gas from either well or shale formation can enhance other dirtier fossil fuels applications in many sectors, particularly in electric generation and heating. The use of gas together with or replacing of other fossil fuel leads to a reducing of harmful pollutant emissions. Reburning, cogeneration, combined cycle generation and fuel cells, which are relatively new technologies associated with electric generation, can support this goal. Gas infrastructure represents the main obstacle in the proliferation of natural gas power plants. It is considerably easy to deal with and modify natural gas power plants once the infrastructure is in place. Using the above modern technologies can double power plant efficiency [13].

Renewable energy, such as wind turbines and solar power facilities, is the most environmental friendly power supply. However, these kinds of power do not supply a guaranteed and reliable energy. Nuclear energy, since Fukushima disaster, has been excluded from many international considerations too [8], [22], [23]. Therefore, other methods for gas usage improvement are required.

1.7.1 Reburning

Reburning is a process for injecting natural gas into other fossil fuel furnaces or boilers. This will lead to the reduction of nitrogen oxides and sulphur dioxide emissions. Air and fuel are divided and introduced to the combustion chamber from several points, ensuring the creation of several zones with different temperatures and stoichiometries.

Referring to figure 1.7, there are three stages, or zones, for reburning, in the first stage, which is called main combustion zone, about 80% of fuel is burned with as less as possible oxygen to keep the combustion almost complete (not 100%). In the second stage, the secondary fuel, which is preferred to be volatile to ensure well mixing and well burning, is injected without oxidizer to make fuel rich mixture. To achieve maximum nitrogen oxides reduction, it needs to maintain the stoichiometric ratio in this zone of about 0.9. In the third stage, also known as reducing zone, oxidiser is injected with a controlled rate to ascertain complete combustion of all fuel [24].

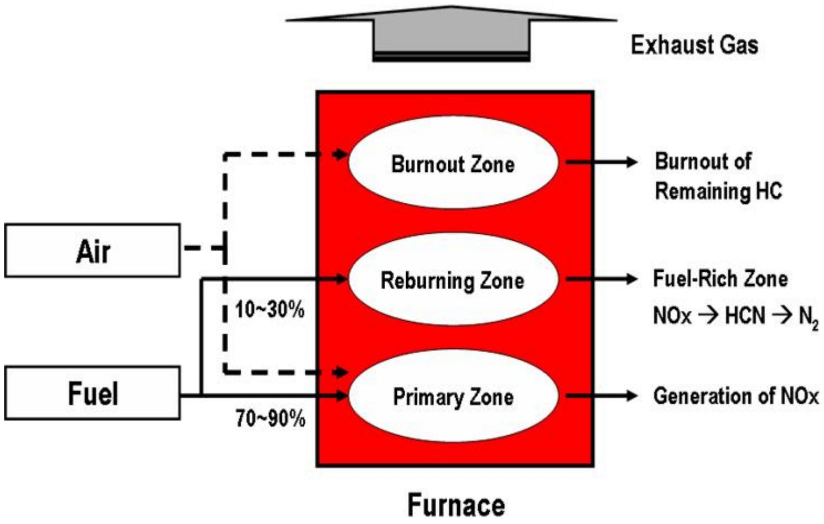

Figure 1.7 Schematic of reburning technology [25]

Reburning might lead to not-complete combustion, which in turn leads to carbon monoxide and soot emission. Hence, combustion control in the third zone is important to reduce any unburnt compound as well as nitrogen oxides reduction [26].

Natural gas is the most preferred reburning fuel, firstly because it is a volatile fuel and contains little amount of nitrogen. Besides it easily mixes with unburnt fuels from zone one and requires very small amounts of energy to reburn. Finally, using natural gas as a reburning fuel will reduce other fossil fuels by about 15%, that means other pollutants like sulphur dioxides and carbon monoxide are going being reduced in a direct proportion [27].

1.7.2 Combined Heat and Power Generation (Cogeneration)

Producing electric power and steam, either for heating or industrial purposes, is a merged technology called cogeneration. In other words, cogeneration is “designed to produce both heat and electricity from a single heat source” [16]. Thermal heat energy wasted in the exhaust gases by the turbine at the end of the generation cycle can be used to produce steam through a boiler for heating or cooling purposes. This technology is very efficient both economically and technically to increase efficiency and decrease thermal waste in the energy supply sector [27].

Cogeneration systems can be classified into two configurations, illustrated in figure 1.8:

- Gas turbine (or engine) based regenerator system: Natural gas or biogas are used in gas turbine to generate electricity, a heat recovery unit could be added to capture heat released through the exhaust stream of the combustion system and converted to steam or hot water. In this system, heat is a by-product of power generation [28].

- Steam turbine based regenerator system: unlike the first configuration, electricity generation in these systems is the by-product of heat generated by a boiler. Steam or hot water surplus can be recycled for other uses. This kind of systems is more convenient for solid fuels (biomass or coal) [28].

Aside from these benefits, cogeneration helps to burn less fuel, which is translated to fewer pollutants emission into the air. Natural gas power generation plants are more flexible and efficient where cogeneration concepts are applicable readily [29].

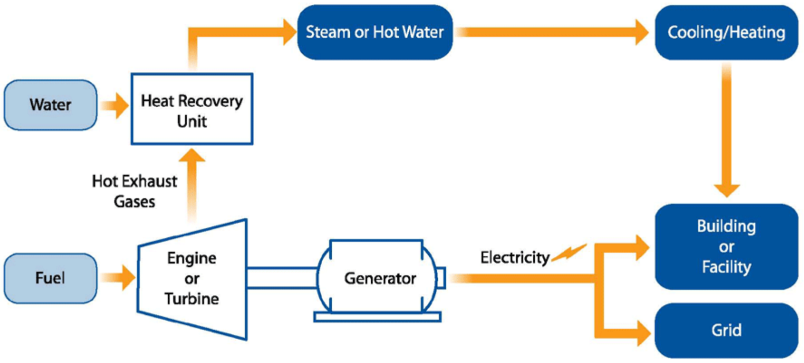

a. Gas turbine with heat recovery unit

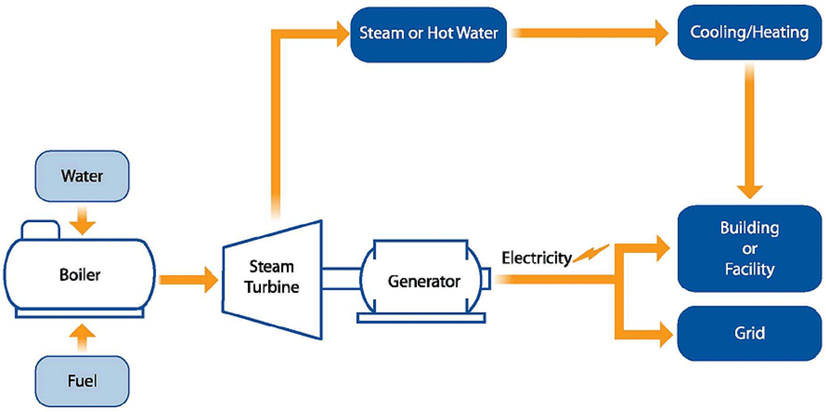

b. Steam boiler with steam turbine

Figure 1.8 Combined heat and power generation system configurations [28]

1.7.3 Combined Cycle Generation

In combined cycle generation configurations, a heat recovery steam generator is used to capture heat from hot exhaust gases released by gaseous or liquid fuel combustion turbines to generate steam in the boiler that feeds a steam turbine. Unlike cogeneration, in this system both combustion turbine and steam turbine are used to generate electricity. Sometimes more than one combustion turbine is used to drive one steam turbine. Thermal efficiency is almost doubled using this configuration. While it is about 30%-35% in a standard thermal power station, it can reach about 60% with stations using combined cycle generation. Combined cycle generation systems, like cogeneration, consume less fuel to produce more energy, thus it produces fewer emissions [22], [13], [17], [27].

In the foreseeable future, and because of the Fukushima disaster in 2011, combined gas cycle generation can be considered as the only viable strategy to fill nuclear power generation gap. Especially because of their relatively moderate capital costs and low fuel prices [8].

1.7.4 Fuel Cells

The chemical potential energy of the fuel is converted through an electrochemical reaction in the presence of an oxidizer directly into electricity or as a by-product into heat in fuel cells. Fuel cells can run indefinitely as long as they are supplied with fuel (hydrogen) and an oxidizer. Although there are different types of fuel cells, they all share the same principles. Two electrodes immersed in an electrolyte. Hydrogen atoms travel from the anode where it is divested from its electron by a chemical reaction and converted to ions. The later travels to the cathode through the electrolyte to combine with oxygen atoms and the returning electron from the electrical circuit to form water. Hydrogen for the cells can be obtained from natural gas [30].

Generally, fuel cells are classified into two categories, low-temperature fuel cells and high-temperature fuel cells. The high-temperature fuel cells do not require an external reformer to crack hydrogen rich fuels, as that could happen within the cell itself due to its high-temperature operation. This process, which is called internal reformer, would reduce fuel cell cost significantly [13], [31], [30].

1.8 Shale Gas in Europe

Europe is the third largest energy consumer in the world, after China and USA. About 40% of its energy is produced using imported fossil fuels. Europe is heavily dependent on imported natural gas, accounting about 24% of the total energy consumed in the continent [3], [32]. All the EU28 countries consume more fossil fuels than they export, as seen in figure 1.9. In fact, some of these countries produce essentially no fossil fuel and depend 100% on imported sources [33].

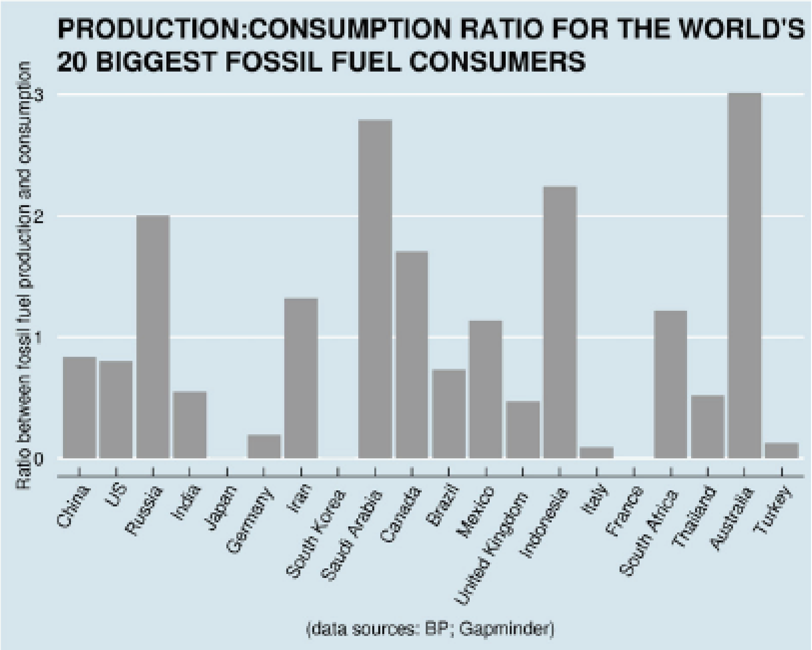

Figure 1.9 Production to consumption ratio for the biggest fossil fuel consumers in the world [32]

The European Commission determined the EU energy goals by economic competitiveness, security of supply and sustainability [34]. These goals are applicable in case Europe produced its own fossil fuel. Shale gas is one of the scenarios that would decrease Europe dependence on imported gas. Although shale gas production is unlikely to give the energy security desired for the whole Europe, it will make a difference for the communities that will adopt it. Because of lack in drilling tests, the volume of recoverable gas in Europe is widely varied. Based on the literature review, EU Joint Research Centres suggested three estimates, high with about 17.6 trillion cubic meters (tcm), best about 15.9tcm and low about 2.3tcm, spread over four large-scale onshore basins in Europe [35], these basins are shown in figure 1.10.

Figure 1.10 Unconventional natural gas resources in Europe [36]

1.9 Shale Gas Extraction

Shale gas is trapped in tiny pore spaces within the shale formation very deep underground, in depths ranging between 1,500-3,000 meters. The impermeable and highly compact nature of the rock containing shale gas makes very difficult to extract commercial quantities of gas in ordinary vertical drillings. Hence, production of vast quantities of shale gas from one well bore requires two specific techniques to be used in the field, horizontal drilling and fracturing.

Subsurface exploration is a very important factor in determining whether shale gas extraction has commercial potential or not. This process lasts for several years, and it includes several topics. It starts with an analysis of various rock samples taken from outcrops to estimate the area and thickness of the formation that contains shale gas. The composition of this rock formation is also required. The first two parameters will help with the reservoir dimensions and the third with its response to fracturing. Then one or two conventional vertical wells are drilled to take samples to measure porosity and permeability to estimate the amount of gas in place. Finally, it is time for horizontal drilling. It is preferred to drill one or two new wells rather than the wells used in the last step, and fracturing, mostly hydraulic, is applied. Production will continue for several weeks in order to assess the profitability and the impact on society and environment after fracturing. The encouraging results will stimulate the next steps [37], [38].

Drilling starts with a vertical well, much like any other conventional hydrocarbon well, but just before the drill reaches the shale formation it is diverted so that the well becomes horizontal and runs parallel to the ground through the shale layer until a target distance is reached. This allows more of the reservoir to come into contact with the well bore. Production casing is inserted into the wellbore, and cement is crammed between the casing and the wall of the hole all through the well [39].

Once drilling is completed, it is now time to perforate and frack the area. A perforating gun is lowered by wire line into the casing. An electrical current is sent down and sets off a charge that shoots small holes through the well bore side walls. Next, the well will have to be fracked. Hydraulic fracturing consists of pumping millions of gallons of water, sand, and an extensive list of manmade chemicals through the drilled hole. As the mixture is forced through, the shale is pressured to fracture. This creates a fairway connecting the reservoir to the well and allows the released gas to flow to the wellbore [39], [40], [41]. Figure 1.11 explain typical hydraulic fracturing operation.

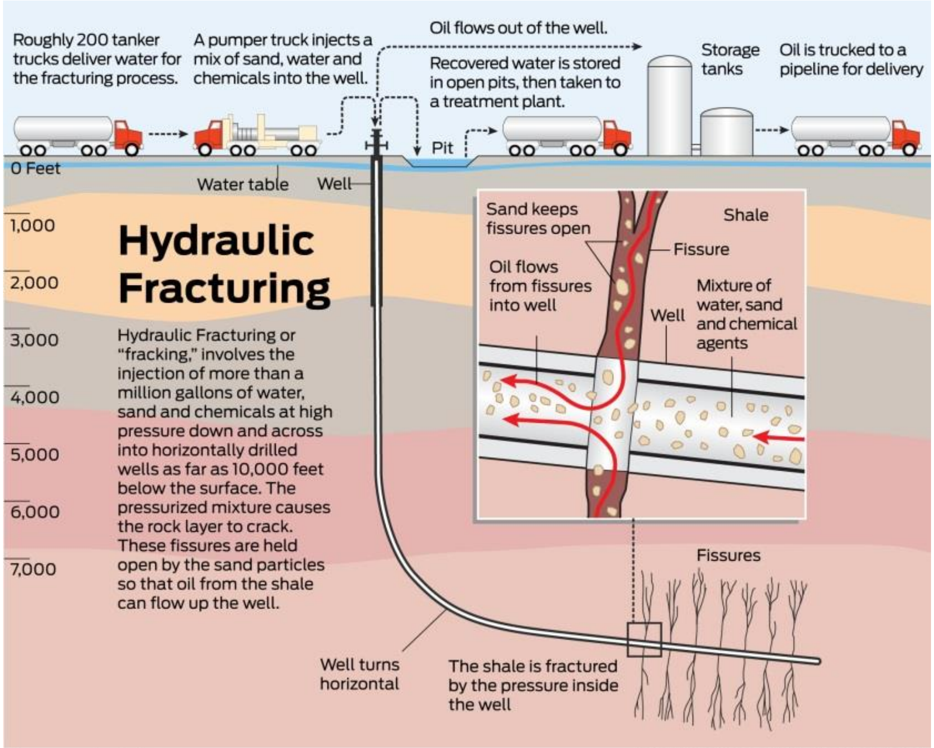

Hydraulic Fracturing or "fracking," involves the injection of more than a million gallons of water, sand and chemicals at high pressure down and across into horizontally drilled wells as far as 10,000 feet below the surface. The pressurized mixture causes the rock layer to crack. These fissures are held open by the sand particles so that oil from the shale can flow up the well.

Source: goodyearlake.org

FRANK VACULIN ● AVALANCHE JOURNAL

Figure 1.11 Typical hydraulic fracturing operation [39]

1.10 Fracture Technologies

The main concern of shale gas extracting is how to achieve it. Hydraulic fracturing technology has been used for hydrocarbon wells stimulation since the mid of the last century. However, this technology has become very common since shale gas started following this technology in conjunction with horizontal drilling [22], [42].

There are three main technologies of fracturing:

1. *i.* Hydraulic fracturing.
2. *ii.* Pneumatic fracturing.
3. *iii.* Dynamic loading fracturing.

Hydraulic fracturing uses liquid fluid to perform the fracturing of the formation. This technology can be subdivided according to the base fluid. Mainly, fracturing fluid consists of three parts, based fluid, additive chemicals and proppant. This technology is subdivided according to the based liquid fluid, but water based hydraulic fracturing is the most famous type. However, some alternative fluids might be used in certain circumstances, such as when water based fracturing is inefficacious or water sensitive formation. Table 1.1 below shows the essential base fluid types with their main composition and expected results [42], [43].

Pneumatic fracturing is used in shallow, brittle and water-sensitive unconventional oil and gas formation. This technique is used when remediation of contaminated soil and groundwater is demanded as it is found to be the most cost effective way to do that. Air or any other gas, like nitrogen, is injected with flow volumes exceeding the natural permeability of the rock and pressures higher than the formation natural strength. Due to gas compressibility effects, the injection pressure in pneumatic fracturing is double or triple to the injection pressure in hydraulic fracturing[42], [44].

Table 1.1 Fluids used for hydraulic fracturing [42], [43]**.**

Base fluid	Fluid type	Main composition	Used for
Water Based	Slickwater	Water + sand + chemical additives	lesser width and greater fracture length
	Linear fluids	Gelled water, Guar, HPG, HEC, CMHPG	Short fractures, low temperature
	Cross-linked fluid	Crosslinker + Guar, HPG, CMHPG, CMHEC	Long fractures, high temperature
	Viscoelastic surfactant gel fluids	Electrolite+surfactant	Moderate length fracture, moderate temperature
Foam Based	Water based foam	Water and Foamer + N2 or CO2	Low-pressure formations
	Acid based foam	Acid and Foamer + N2	Low-pressure, carbonate formations
	Alcohol based foam	Methanol and Foamer +N2	Low-pressure, water-sensitive formations
Oil Based	Linear fluids	Oil, Gelled Oil	Short fractures, water-sensitive formations
	Cross-linked fluid	Phosphate Ester Gels	Long fractures, water-sensitive formations
	Water Emulsion	Water + Oil + Emulsifiers	Moderate length fracture, good fluid loose control
Acid based	Linear	Guar or HPG	Short fracture, carbonate formations
	Cross-linked	Crosslinker + Guar or HPG	Long, wide fractures, carbonate formations
	Oil Emulsion	Acid + Oil + Emulsifiers	Moderate length fracture, carbonate formations
Alcohol based	Methanol/water mixes or 100% methanol	Methanol + water	
Emulsion based	Water-oil emulsions	Water + Oil	
	CO2-methanol	CO2 + water + methanol	
Cryogenic fluids	Liquid CO2	CO2	
	Liquid nitrogen	N2	
	Liquid helium	He	
	Liquid natural gas	LPG (butane and/or propane)	

Fracturing with dynamic loading, also known as dry fracturing, is a technique where no fluids are used. The fracturing occurs by inducing a dynamic loading, even by explosive propellant systems or electrical impulse at the bottom of the wellbore. The explosive propellant system consists of two stages. The first stage is a high accumulative detonation produced by a multistage propellant combustion. The second one is to create a multiple fractures in shale rock, this is achieved by a low explosive propellant which will generate high pressure gas at high rates. Even though the fractures made by dry fracturing are much smaller than the ones made by hydraulic fracturing, this technology has its own advantages. The solution for environmental concern is one of the main advantages in addition to the economic side. The dry fracturing technology can be a very economical alternative, as it requires much less on-site, specialised equipment and, in addition, it resolves many of the environmental problems associated with shale gas production in Europe. Also, it resolves some of the problems associated with waterbased hydraulic fracturing processes that may damage water sensitive shale formations or other gas-bearing formations [42], [45]. A brief comparison of hydraulic fracturing with dry fracturing is given in table 1.2.

Table 1.2 Comparison of fracturing technologies [45]

Consideration	Water Based	Dry Fracturing
Environmentally friendly	N	Y
Fluid availability	?	-
Fluid recycling	Y	-
Chemicals used	Y	N
Reservoir compatibility	?	Y
Fracture creation	Y	Y
Proppant carrying	Y	?
Recovery to pipeline	N	N
Heavy metals flowback	Y	N
Frack cost	1	<<1
Fluid left in formation	Y	-
Well clean up	Y	Instant production
Frack geometry predictability	N	Y
Tilting stress development	Y	N
Zone water in flux risk	1	>>>1
Fracture length	1	>>1
Active flow frack perforation	?	Y
Fracked well performance	1	>1
Local road damage risk	Y	N
Environmental risk	Y	Y
NOx and CO2 in pumping	Y	N
Return on investment	1	<<<1

1.11 Objective of The Work

Producing extensive high-pressure waves at the base of the well bore by using detonation is a potential technique for shale gas extraction. This technique might overcome both small distance cracking of dynamic loading fracturing and the environmental disadvantages for fracking. The detonation phenomenon is known since the end of the nineteenth century. Detonation waves have been defined as “shock wave with energy evolution inside the wave front”. The interaction of shock waves travelling ahead of the flame with the boundary layer formed by the precursor shock is the important factor to trigger the detonation. The crucial role is played by thermodynamic interactions and the induction time.

The main objectives of this study can be summarised in the next points:

- Designing an experimental rig to generate pressure pulse waves produced by detonation using natural gas and pure oxygen as combustible fuels for a range of equivalence ratio.

- Study the health and safety issues accompanied by detonation using hazard and operability study (HAZOP). In addition to making risk assessment to the system and the occupied environment.

- Numerically analyse the detonation products using 0-D and 1-D codes to predict the highest pressure, temperature and velocity for the purposes of design and to find the optimum equivalence ratios that can be used in experimental work.

- Investigate the influence of obstacle geometry on deflagration to detonation transition characteristics by simulating different obstacle geometries set inside a 1in outer diameter pipe proposed to carry out the experimental work.

- Study the effect of produced pressure pulse waves on cracking a perforated area of shale rock and find the crack propagation in that area.

1.12 Thesis Structure

This thesis is structured of nine chapters. These chapters are organised as follow,

- Chapter one is a general introduction review the impact of using natural gas as a substitution of other kinds of fossil fuels on various aspects. In addition to the shale gas resources in Europe and the way of its extraction.

- Chapter two starts with defining combustion phenomena and main flame propagation stages identified by researchers. Detonation models have been described along with the effect of confinement, obstruction and initiation modes, followed by a review of some previous work in deflagration to detonation transition for several types of fuels. Finally, the health and safety legislations in Britain and Europe have been addressed briefly. This chapter has finished by the HAZOP study requirements and procedures.

- Chapter three describes the design of proposed apparatus and its concept. Rig layout and setup was the subsequent section in this chapter along with the related detailed HAZOP study and risk assessment.

- Chapter four presents the 0-D and 1-D numerical analysis using GASEQ and CHEMKIN-Pro software. Results of these codes are drawn with respect to range of equivalence ratio to find the best configuration that will be used in experiments.

- Chapter five presents the results of 2-D CFD simulation of the deflagration to detonation transition of stoichiometric hydrogen/air mixture in the proposed experimental detonation tube. Several internal geometries, obstacles, shapes, etc., have been examined here.

- Chapter six is based on experimental tests obtaining some of the shale rock characteristics out of samples obtained from the Dulais Valley, South Wales, and compare them with some others obtained from the Bowland-Hodder area.

- Chapter seven is a two-dimensional study performed to predict the pressure pulse produced using detonation tube on a pre-crack propagation generated primarily by perforating.

- Chapter eight discusses all the obtained results from the last chapters comprehensively and highlights the major findings.

- Chapter nine draws together the conclusions from each of the previous chapters and suggests areas for further study.

CHAPTER TWO

From Deflagration to Detonation

2.1 Introduction

Self-propagating combustion waves are classified depending on flame velocity and pressure variation. Thus, they are classified into two types, Deflagration and Detonation. A brief description of deflagration and a more detailed description of detonation waves are discussed in this chapter. Detonation phenomenological description and the most famous theories applied to justify the enormous and sudden change in gas properties across the flow, as well as the boundary and initial conditions that effect this phenomenon are going to be addressed here. Also, this chapter will mention methods to analyse deflagration to detonation transition phenomena and discuss some experimental and numerical with fundamental governing equations for flow and flame characterisation.

The following part of this chapter talks about health and safety for deflagration to detonation transition, emphasizing hazard and operability studies (HAZOP) associated with detonation. After a brief discussion on some fuels used to generate detonation, the main purpose of using unconventional fuel, precisely shale gas, to initiate detonation is also discussed. This leads onto a justification for the rest of the work in this thesis.

2.2 Combustion Phenomena

When reactants ignited, by any mean of ignition source, a combustion wave is generated and propagates away from the ignition source. As the combustion wave passes through reactants, reactants are transformed into products by breaking the chemical bonds of their molecules and releasing the stored chemical energy. This energy is then converted to thermal and kinetic energy, which in turn significantly influence thermodynamics states of the substance across the combustion wave. Physical and chemical processes, which are generated by the gradient fields across the wave, lead the combustion wave to be self-sustained.

Depending on fuel and oxidiser mixing location, combustion is divided into premixed, diffusion and partially premixed combustion. While in premixed combustion the fuel and oxidiser are mixed outside the combustion chamber, the formers are introduced separately into the combustion chamber in diffusion, also known as non-mixed, combustion. Partially premixed combustion is a combination of the last two combustion types, where the fuel and oxidiser are not completely mixed before they are introduced into the combustion chamber[46].

Flame speed, which is the speed at which the flame front travels in an unburned mixture, is related to many factors such as equivalence ratio, dimensions and shape of the combustion chamber, presence of obstacles, and other factors. This speed will determine the flame propagation waves scenario as deflagration, deflagration to detonation transition DDT, or detonation [47].

Although deflagration and detonation are similar processes, they represent opposite limits of the spectrum of reactive flow phenomena. It is of importance to define and distinguish between deflagration and detonation combustion waves. The findings of Bertheldt [48] and Mallard and LeChatelier [49] in 1881 stimulated the study of chemical reaction in this important topic of combustion. The velocity propagation was measured a year later by Bertheldt and Vieille, who developed a theory to explain the experimental data [50]. Photographic techniques, using a rotating drum camera, enabled Mallard and LeChatelier [51] to notice the oscillatory movements of the flame front preceding the transformation from the initial uniform motion to high velocity combustion[51].

2.3 Flame Propagation

In the initial stage of flame propagation, just after ignition, the main source of the flame acceleration is the increasing surface area of the flame[52]. When the flame hits the back and side walls of the confinement pipe, the flame propagation will pass through four stages as distinguished by Clanet and Searby (1996)[53]. In the first stage, the pipe’s walls do not affect the flame front propagation, thus taking a hemispherical shape. In the second stage, as the pipe’s walls start to affect the flame propagation, the radial flame propagation velocity towards the walls is assumed to approach the laminar flame velocity. At the same time, as the flame surface area is enlarged and changes its shape to what is known as finger shaped flame, the axial velocity will boost and be much higher [54].

Clanet and Searby found empirical relations for the time when the flame reaches the pipe wall, t_{wall}, and for the time when the flame front changes from spherical to finger shaped, t_{sphere}, as following [53]:

$$\mathbf{t_{wall} = 0.26\left(\frac{r}{S_l}\right) \pm 0.02\left(\frac{r}{S_l}\right)} \qquad \textbf{Equation 2.1}$$

$$\mathbf{t_{spere} = 0.1\left(\frac{r}{S_l}\right) \pm 0.02\left(\frac{r}{S_l}\right)} \qquad \textbf{Equation 2.2}$$

where r is the pipe radius and S_l is the laminar burning velocity.

Also, depending on the time variation of the volume of the burned gases and equating it to the mass consumption rate of fresh gas, an analytical relation between t_{wall} and t_{sphere} can be driven:

$$\mathbf{t_{spere} = t_{wall} - \frac{r}{S_l}\frac{1}{2\alpha}\ln\left(\frac{Z_{wall}}{r}\right)} \qquad \textbf{Equation 2.3}$$

where α is the expansion ratio, and Z_{wall} is the axial position of the flame front when it first touches the pipe side wall. They have found that, the time when the flame reached the pipe wall is almost the time when experiments show the first rise in pressure, as indicated in figure 2.1.

The next stage of the flame propagation happens when the inversion to a tulip flame shape begins. The expression " tulip flame" was first called by Salamandra et al. in 1959 to describe the sudden change of flame shape from forward finger to backward cusp [55]. The increase of pressure before the flame front cause a flow in the direction opposite to the flame front propagation.

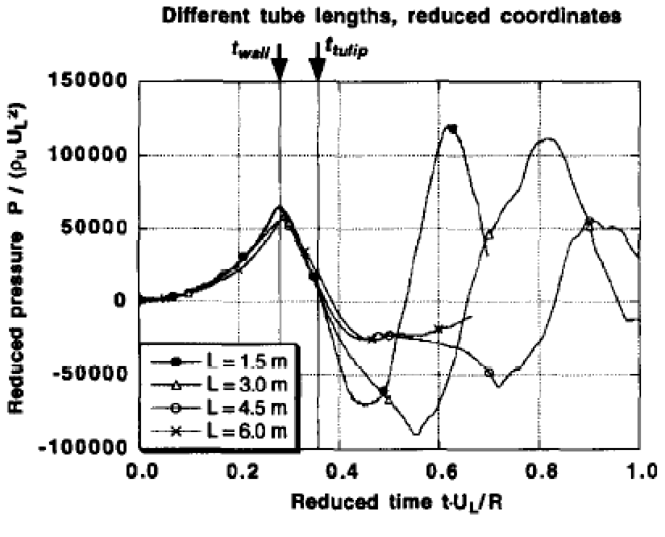

Figure 2.1 Pressure at the closed end of a shock tube for stoichiometric propane-air flames [56]

As in the two last stages, Clanet and Searby were able to develop empirically a linear function of radius to laminar burning velocity ratio to calculate the time when the tulip flame happens as:

$$\mathbf{t_{tulip}} = \mathbf{0.33}\left(\frac{\mathbf{r}}{\mathbf{S_l}}\right) \pm \mathbf{0.02}\left(\frac{\mathbf{r}}{\mathbf{S_l}}\right) \qquad \textbf{Equation 2.4}$$

From their experiments, Clanet and Searby concluded that the major cause of the tulip inversion is the Rayleigh-Taylor instability. This instability results from the pressure and density gradients in presence of an acceleration or deceleration at the burnt light fluid and unburnt denser mixture interface surface.

The last stage covers the flame propagation after the tulip inversion. The flame surface inversion leads to decrease in the surface area which in turn leads to flame deceleration. In such a case where the pipe is long enough and in absence of acoustic waves, this deceleration is followed by an acceleration that results from the increase of the flame surface area when the flame becomes concave towards the unburnt mixture again. Due to the new acceleration, the same mechanism of instability can generate a new tulip inversion, and the flame propagation is decelerated once again [9], [12]. Figure 2.2 shows these processes.

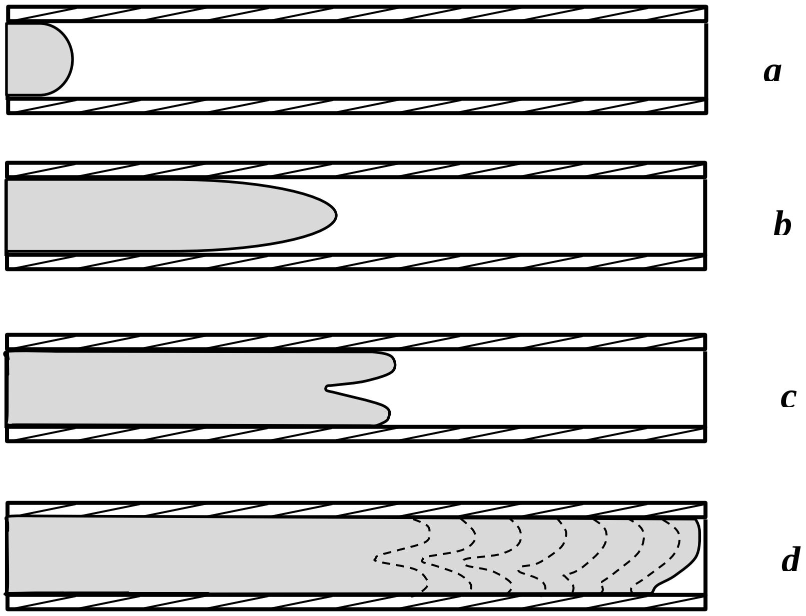

Figure 2.2 The four stages of flame propagation in confined geometry.

a. Hemispherical shape. b. Finger shaped. c. tulip flame. d. flame surface inversion.

2.4 Deflagration Waves

Deflagration waves are expansion waves that propagate at low subsonic velocity, the pressure falls across the reaction zone and the products move in a direction opposite to the wave propagating direction [57].

When an ignition source is ignited in a fuel-oxidiser medium, the flame initially propagates as a sphere outward from the ignition point. The relatively large increase of sphere surface area in all direction leads to high flame acceleration and propagation. If the medium is confined in a pipe, the flame will be quenched, as it reaches the confinement walls. This will allow the flame to propagate in one direction, when the ignition source is placed near one of the pipe’s ends, with a hemispherical shape[52].

Deflagration can be divided according to turbulence presented in the unburned gases into laminar or turbulent. If there is no initial turbulence presented in the unburned gases, deflagration undergoes laminar flames and their shape is modified depending on number of instabilities. When turbulent is presented, a variety of turbulent combustion propagation regimes will be presented due to the interaction between the flame and turbulence [58].

2.5 Detonation Waves

Detonation waves are compression waves, the density increases across it and the products move in the same direction of the wave motion. Detonation waves move at a supersonic velocity, the reactants ahead keep their initial conditions prior to detonation arrival, and therefore, the thermodynamics states across it increase precipitously.

The detonation phenomenon was discovered by the end of the nineteenth century when the diagnostic tools development by the time enabled observation of rapid combustion phenomena and measurement of combustion waves propagation velocity. A first theory predicts detonation velocity, which is based on Rankin and Hugoniot analysis of conservation equations across a shock wave. The theory was formulated independently by Chapman [59] and Jouguet [60] shortly after the discovery of the phenomenon. Zeldovich[61], vonNeuman [62] and Doring [63] took in to account the time that radicals take to form and initiate the reaction using Rankin-Hugoniot curves, thus developing another theory.

Although detonation wave speed has two possible solutions, strong and weak detonation, these two solutions converge when the speed of detonation goes to a minimum, and there is no solution provided for detonation below this minimum velocity. For the strong detonation, the flow downstream the detonation wave is subsonic and pressure and density are higher than those for weak detonation with supersonic downstream flow.

2.5.1 The Chapman-Jouguet Theory

The detonation wave in the C-J theory has been considered as a discontinuity with infinite reaction rates, with all energy added instantaneously in the chemical reaction zone that follows the shock. Both reactants and products are modelled as perfect gases.

C-J theory refers to the criterion for the choice of the detonation velocity for a given explosive mixture. While Chapman choose the minimum velocity solution based on experiments, Jouguet determined the entropy variation along the Hugoniot curve to locate the minimum value, which is noted to be corresponding to sonic condition downstream the detonation wave. However, it has been shown that the minimum velocity solution, just like the minimum entropy solution, gives sonic flow downstream of the detonation wave.

Mass, momentum and energy conservation laws are applied with a steady one-dimensional assumption across a control volume shown in figure 2.3.

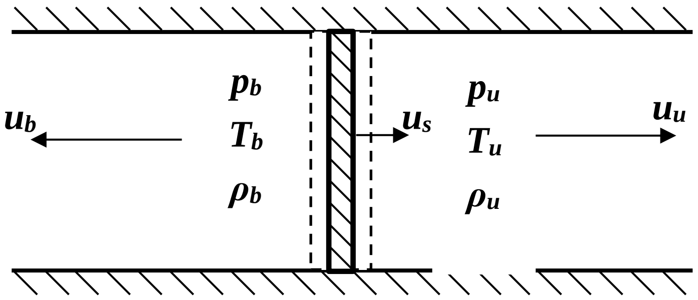

Figure 2.3 Control volume for a moving wave in combustible mixture.

The relative velocity of unburned and burned gases with respect to the shock wave velocity are denoted with the ‘prime’, and are given by:

$$\mathbf{u'_u = u_s - u_u} \qquad \textbf{Equation 2.5a}$$

$$u'_b = u_s - u_b$$ **Equation 2.5b**

where subscripts u, b and s are stand for unburned gases, burned gases and shock respectively. Hence, the continuity, momentum and energy equations are:

$$\boldsymbol{\rho_u u'_u = \rho_b u'_b}$$ **Equation 2.6**

$$\boldsymbol{p_u + \rho_u u'^2_u = p_b + \rho_b u'^2_b}$$ **Equation 2.7**

$$\boldsymbol{\frac{\gamma}{\gamma-1}\frac{p_u}{\rho_u} + \frac{1}{2}u'^2_u + q = \frac{\gamma}{\gamma-1}\frac{p_b}{\rho_b} + \frac{1}{2}u'^2_b}$$ **Equation 2.8**

where u is velocity, ρ is density, p is pressure, q is the heat release per unit mass of reactants due to chemical reaction, and γ ratio of the specific heat of the gas

When unburned gases are in stagnation, the equations above can be written as:

$$\boldsymbol{\rho_u u_s = \rho_b (u_b - u_s)}$$ **Equation 2.9**

$$\boldsymbol{p_u + \rho_u {u_s}^2 = p_b + \rho_b (u_b - u_s)^2}$$ **Equation 2.10**

$$\boldsymbol{\frac{\gamma}{\gamma-1}\frac{p_u}{\rho_u} + \frac{1}{2}u^2_s + q = \frac{\gamma}{\gamma-1}\frac{p_b}{\rho_b} + \frac{1}{2}(u_b - u_s)^2}$$ **Equation 2.11**

Combining mass conservation with momentum conservation equations yields the Rayleigh relation:

$$\boldsymbol{(p_b - p_u) = \rho_u u^2_s \left(1 - \frac{\rho_u}{\rho_b}\right)}$$ **Equation 2.12**

The Rankine-Hugoniot relation yields by substituting Rayleigh relation into energy conservation equation;

$$\boldsymbol{q = \frac{\gamma}{\gamma-1}\left(\frac{p_b}{\rho_b} - \frac{p_u}{\rho_u}\right) - \frac{1}{2}(p_b - p_u)\left(\frac{1}{\rho_b} + \frac{1}{\rho_u}\right)}$$ **Equation 2.13**

The schematic of the Rankine-Hugoniot curve is shown in figure 2.4, where point A represents the unburned gases state. All the Rayleigh lines describe the process starting from point A. The Rayleigh line intersection with the Rankine-Hugoniot curve represents the final burned state. However, there are two particular lines that are tangential to the Rankine-Hugoniot curve, at points D and E. With the horizontal and vertical lines of unburned gases states passing through the Rankine-Hugoniot curve at B and C, five regions along the curve are distinguished.

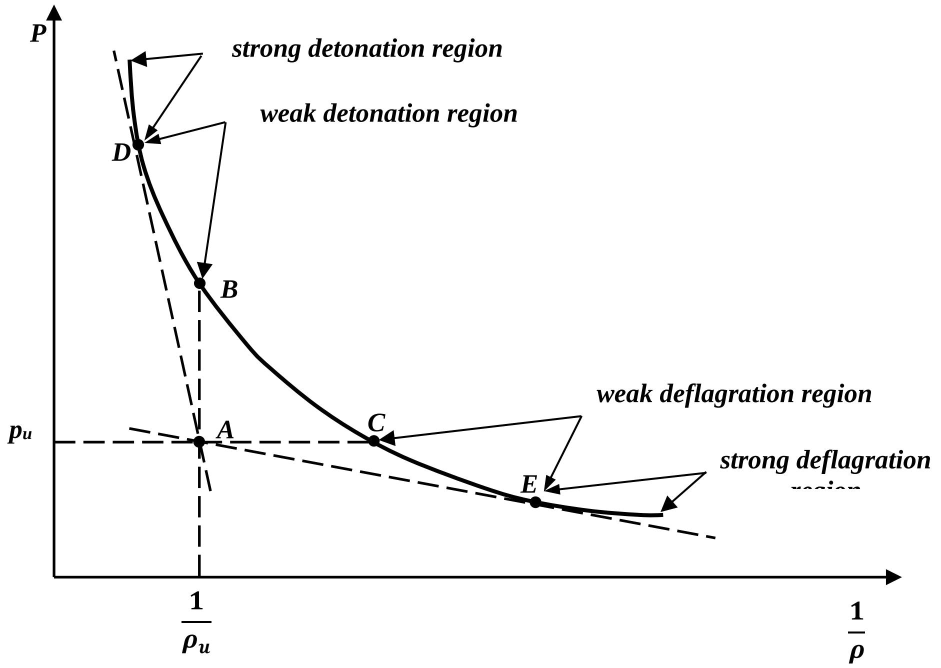

Figure 2.4 A schematic of Rankine-Hugoniot curve and Rayleigh lines shows the region distinguished along the curve

Two regions, where $p_b<p_u$ and $\frac{1}{\rho_b} > \frac{1}{\rho_u}$, underneath E represents a strong deflagration region, and from C to E, represents weak deflagration. The other two regions, where $p_b>p_u$ and $\frac{1}{\rho_b} < \frac{1}{\rho_u}$, represent weak detonation from B to D, and the strong detonation from D and up. The last region, where $p_b>p_u$ and $\frac{1}{\rho_b} > \frac{1}{\rho_u}$, represents an impossible solution because there is no positive slop as the Rayleigh line definition states:

$$\rho_u u_s = \sqrt{\frac{(p_u - p_b)}{\left(\frac{1}{\rho_b} - \frac{1}{\rho_u}\right)}} \qquad \textbf{Equation 2.14}$$

Point D represents the point where u_s is at its minimum and is equal to the summation of the sound speed in the product and the product gases speed:

$$u_s = c_b + u_b \qquad \textbf{Equation 2.15}$$

Also, the product gases entropy below this point is lower than the entropy of the product gases at the point itself and above. All of that, makes this point the only stable solution for the detonation, as Chapman and Jouguet stated in their theory.

2.5.2 ZND Detonation

Zeldovich [61], von Neumann [62] and Doring [63] independently developed detonation model well known as ZND theory. Starting from C-J theory, taking into account the detonation wave structure, they considered a trivial delay time to the energy to be released after the shock with finite reaction rates.

The shock wave, followed and strengthened by the reaction region, will increase the pressure and temperature of the reactants upstream the shock to ensure a high rate reaction so that the energy released is enough to keep the shock moving at high speed while assuming no reaction takes place in the shock wave region.

Figure 2.5 shows the behaviour of physical properties through a detonation wave according to the ZND theory. Four regimes are indicated, the first regime is the state of unburned gases. The next regime refers to the shock wave, the physical properties here change dramatically as explained above. The deflagration regime follows, and is subdivided into induction zone and heat addition zone. Although chemical reaction takes place in this regime, the physical properties in the induction zone are almost flat due to the very slow reaction rate. As the reaction rate soars in the heat addition zone, the physical properties will change sharply and C-J state will be reached by the end of this regime.

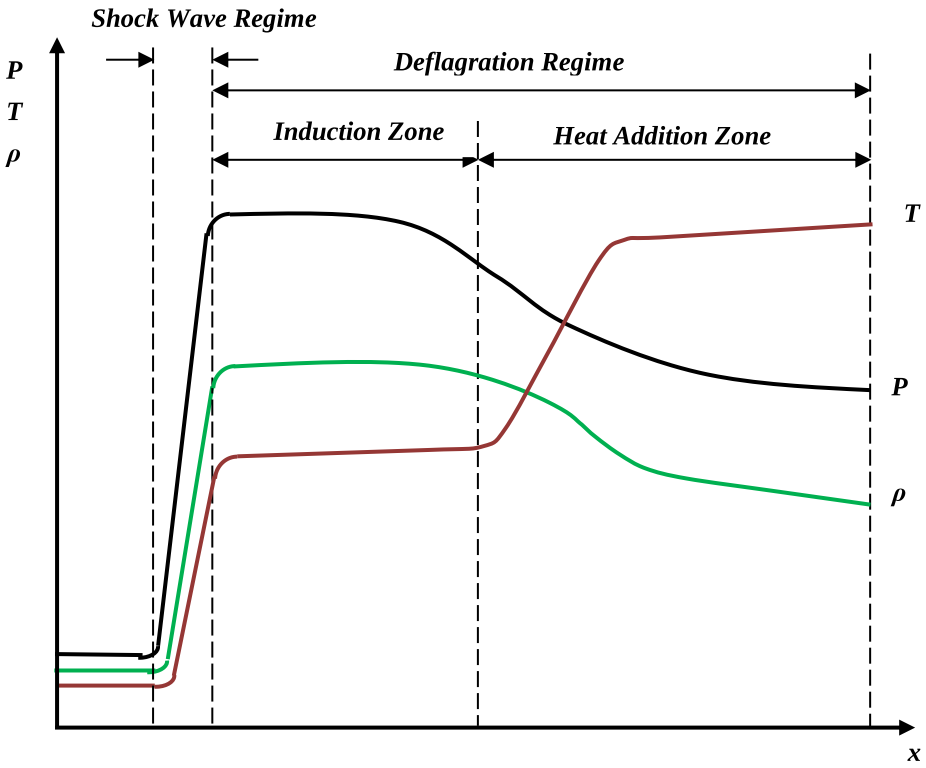

Figure 2.5 Physical properties behaviour through a ZND detonation wave.

2.6 DDT Phenomenon

Deflagration waves are inherently unstable waves, for that their turbulent reaction front leads to increase their propagation speed [64], until this speed reaches the boundary conditions where the propagation undergoes a sudden transition to detonation. The low energy required to trigger a deflagration makes it the more probable mode of combustion to happen. However, experiments have shown that, under certain conditions when the flame velocity continuously accelerates until it reaches about half the CJ detonation speed, a spontaneous onset of detonation takes place [65].

As it is illustrated in figure (2.4), the lower part of Rankine-Hugoniot curve represents the deflagration solutions, while the upper part represents the detonation solutions. Hence, transition from deflagration to detonation solutions is thought of as a jump from the lower to the upper part of the curve [47]. Nevertheless, precursor compression waves generated ahead of the deflagration flame due to products expansion will travel through reactants raising their temperature and changing the initial state. As the Rankine-Hugoniot curve depends on this initial state, it will change and give different deflagration solutions [66]. Higher temperature reactants cause faster compression waves apt to catch up the previous ones, and so on until all waves merge at a point forming a shock wave. Finally, when detonation is triggered, its wave is supersonic, therefore the initial state is considered as the original undisturbed conditions, which will go back to the original Rankine-Hugoniot curve.

The distance required for deflagration to transform into detonation (predetonation distance) is affected by many factors. The most dominant ones are discussed in the next section.

2.6.1 Boundary conditions

Boundary conditions exerts a strong influence on the propagation of detonation waves. It has been proved in many experiments that the presence of obstacles in pipes containing moving flames cause rapid flame acceleration. Turbulence is the result of that presence. Turbulence, in turn, increases the local burning rate by increasing both the surface area of the flame and the transport of local mass and energy. This leads to higher flow velocity in the unburned gas. All of these actions, under appropriate conditions, will lead to detonation[64]. For that, in smooth channels without obstacles only turbulent deflagration regimes can be achieved [67].

The predetonation distance can be decreased by initial flow turbulence increases, which is an essential factor to influence deflagration to detonation transition [68]. In a tube with nonslip walls, the flame–sound interaction also strongly influences the oscillations of a flame front. Flame–sound interaction happens mainly due to the acoustic mode between the closed tube end and the flame front. Oscillations are stronger in wider tubes, in sufficiently wide tubes violent folding of a flame front can be observed [69].

In a duct filled with an explosive gas mixture, the mixture properties and the duct geometry, which includes the wall surface roughness, governs flame propagation. The interaction of transverse pressure waves generated at the rough wall governs the propagation mechanism, not the boundary layer turbulence. The transverse waves, and its frequency appears to play a role in supporting the detonation wave [70].

Deflagration-to-detonation transition in reactive gases usually occurs in confined or partially confined spaces, the shape and layout of obstacles have a significant effect on flame acceleration, and subsequent detonation propagation. The flame accelerates as its surface bends with the flow around obstacles, which leads to formation of shocks ahead of the flame. These shocks are reflected by obstacles and propagate back to interact with the flame. When shocks become strong enough, their collisions with obstacles ignite the gas mixture, and detonations form [71].

The effect of obstacles geometry on the shock wave has been numerically studied by Sha et.al. (2012) [72] and (2014) [73]. Reflected wave and expansion wave were found to be generated by interaction between incident shock and obstacle. Both waves interact with the main shock and oppositely influence it. While the reflected shock increases pressure of incident shock, the expansion one decreases it. The shape and dimensions of the obstacle has also investigated by the researchers. The pressure of incident shock front was found to be highly influenced by the width of upper side and the height and angle of windward side, but neglectable effect by the leeward side. Higher pressure can be achieved with wider upper side and higher and more acute triangles obstacles [72], [73].

The method and location of initiation has its share of importance, a commercial spark plug, electrode or even an additional small tube filled with a sensitive mixture with conventional spark plug can be used [74].

Heat and momentum losses through the confining walls are one of the detonation propagation factors. The confinement tube diameter effects detonation velocity. There is a critical tube diameter for detonation to propagate, which is about a thirteenth of the detonation cell width for a given explosive mixture. The detonation cell is a multidimensional structure which includes both the detonation wave and transverse wave.

Another boundary condition that affects the propagation of detonation is the walls roughness. It is found that the presence of spiral wires could highly reduce the normal CJ detonation velocity [75].

2.7 Methods to analyse the DDT phenomenon

Understanding the deflagration to detonation transition phenomenon, either for safety purposes or due to its potential application to high thrust propulsion systems, has led researchers to conduct many studies since the last century. These studies can be classified into two main categories, experimental and numerical.

2.7.1 Experimental Method

Many experimental investigations have been conducted to understand various aspects of detonation. Detonation initiation is one of the most interesting processes in experiments, and it can be divided into direct and indirect initiation. As the detonation is a strong shock followed and supported by the chemical energy released by reactants, the igniter required to provide a strong shock for a sufficient duration in order to generate direct detonation initiation. Electrical discharge, high power lasers or condensed explosive charges are usually used to produce such a high energy [76].

Spherical detonation was the first observed direct initiation in 1923. A powerful mercury fulminate igniter was used to detonate carbon disulfide (CS_2) with oxygen in an unconfined geometry [77]. No detonation was produced when the same experiment was repeated using an ordinary spark. In 1949, Shepherd [78] used a confined geometry to demonstrate the direct initiation of detonation using the pressure wave from a blasting explosive to ignite the reactants. Exploding wire [79] and spark gaps [80] are two other techniques used to establish direct initiation of detonation in oxy-fuel mixtures. The amount of energy deposited in the later techniques, were difficult to be estimated.

However, the various flame acceleration mechanisms related to confining geometry play a pivotal role in detonation initiation. In a normal deflagration to detonation transition (DDT), the onset of detonation would require further flame acceleration once a deflagration is ignited. The distance travelled for the acquisition of this acceleration from the ignition point to the detonation formation is usually referred to as the DDT length. The DDT length is influenced by the pipe geometry, diameter, length and wall roughness. It is also influenced by the fuel-oxidiser type and equivalence ratio, and the ignition method and location. Finally, the initial mixture conditions have been shown to play an influential role on DDT length.

Porowski et al. [67] carry out an experimental study in a 6m long circular cross section tube with inner diameter of 140mm. Stoichiometric hydrogen-methane-air with different methane concentrations at ambient conditions was used to study the effect of obstacles locations and configurations on flame propagation, acceleration and transition to detonation. The transition to detonation was noticed to be more likely with higher methane concentration when the blockage area is 40% and the distance between obstacles is three times the pipe diameter [67].

The effect of spark timing in addition to geometry and equivalent ratio was investigated by Meyer et al. [81]. Shchelkin spiral, extended cavity with spiral and co-annular geometries were used with a 2 in inner diameter tube for H2/Air fuel. It was concluded that there is a fundamental difference in local explosion propagation between a Shchelkin spiral geometry and axisymmetric obstacles. The extended cavity before the Shchelkin spiral generate strong early detonations that are quicker to vanish. The nature of transition to detonation remains the same for different equivalence ratios, its only effect will be on the location of transition. The primary impact of spark timing was on the progression of the detonation wave further downstream the tube [81].

Detonation limits are other fundamental property of explosion with vast share of interest. Many attempts have been made to develop a general theory about detonability limits, but it has been impossible due to the strong dependence on tube geometry, fuel and ignition.

For methane-air mixture in high length to diameter ratio, detonations were successfully initiated by Zipf et al. (2013) [82] for mixture containing between 5.3% to 15.5% methane by volume. These finding are wider than the limits ascertained by Wolanski et al. in 1981 [83], where detonation was attained at 8% to 14.5% methane in methane-air mixture. Vanderstraeten et al. (1997) [84] stated that the lower explosion limit for methane concentration was of 4.6±0.3% and upper explosion limit was of 15.8±0.4%, and the maximum pressure rise occurs at a methane concentration of about 9.5% of the total mixture volume [84], as it illustrated in figure 2.6.

Initial pressure and temperature of combustible mixtures has a slight effect on the detonation velocity, but the acceleration process can be sensitive to the initial pipe wall temperature or mixture humidity [81], [82]. Although detonation velocity is essentially independent of initial pressure, increasing initial pressure results in decreasing reaction time and hence decrease the run-up distance to achieve DDT [85], [86]. Thus, it is evident that further research is still needed.

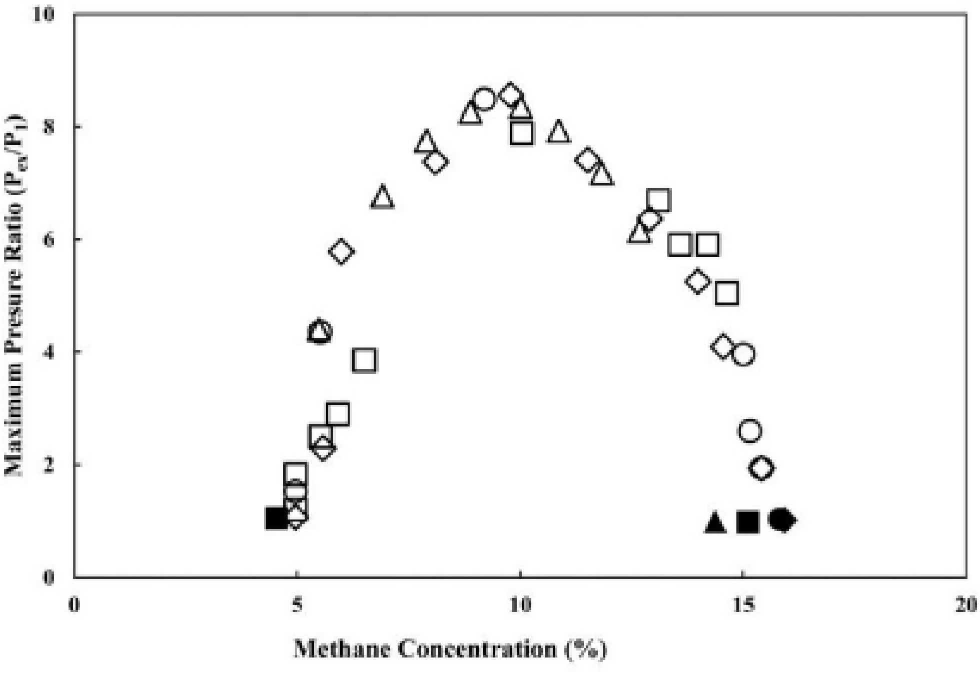

Figure 2.6 Lower and upper explosion limits and maximum pressure ratios for methane air mixture at atmospheric conditions [84].

2.7.2 Numerical Method CFD

Since 1970's when the computer developments made it possible to numerically simulate complicated phenomena, substantial attempts have been made to analyse and understand detonation. Due to its relatively simpler chemical kinetics and potentially catastrophic consequences in case of any accidentally release, hydrogen is often used as fuel in numerical studies [87], [88]. Intricate nonlinear reactions in addition to other physical processes like turbulence, shock waves and flame interaction made the simulation of deflagration to detonation transition one of the most challenging problems in combustion [89].

However, vast numerical and simulation works related to DDT show good agreement with experimental results. A good recapitulation of ten-year theoretical and numerical efforts to comprehend DDT has been made by Oran et al. [90]. They stated, "the turbulent flame itself does not undergo a transition to detonation", but it helps to create an environment to generate ignition centres in the reactant zones to contribute with the detonation. The interaction between shocks and flames with obstacles and boundary layers represent another assistant factor to create such an environment. An obstructed channel filled with hydrogen-oxygen mixture were simulated to find how the ignition centres, or hot spots, formed under turbulent flame effect, and how those hot spots can support a spontaneous reaction wave and if this wave can undergo a successful transition to detonation. Yet, detonation observed in this simulation was unable to surpass obstacles [90].

Ciccarelli et al. (2008) [91] published a detailed review about experimental and numerical studies related to flame acceleration and DDT in both smooth and obstructed ducts. Flame processes and detonation propagation are controlled by interplay of many spatial and temporal physical scales related to chemistry, turbulence and confinement. Nevertheless, it is extremely difficult to analyse all phenomena involved because of the wide range of existing scales [91].

Detonation waves as a fundamental combustion process was the major theme that Shepherd (2009) [92] focused on in his experimental, modelling and simulation review. Mixture types, boundary and initial conditions identified the behaviour of detonation front structures and their paradigm. Using systematic variation of the reactants composition, an experimental and numerical evidence was presented for the transition between combustion regimes. On the other hand, more difficulties regarding physical and chemical models are faced for simulation.

2.8 Fuels for DDT

Gaseous fuels are the common fuels that used to carry out detonation experiments due to ease in getting homogeneous mixtures in single-phase mixtures. However, remarkable efforts have been done by many researchers to sustain detonation in liquid fuels (two-phase fuel). There are multiple factors, such as droplet size, droplet breakup and the presence of fuel vapour that affect the detonation initiation and its sustain [93]. It is found by many researchers that droplets size must be sub 10µm in order to sustain detonation [94], [95]. Furthermore, when the liquid fuel droplets are about 2µm similarities in behaviour can be seen in the transition to detonation process with gaseous detonation.

Nevertheless, detonation using gaseous fuels is much easier and more achievable, and it depends strongly on the fuel-oxidiser combination. The sensitivity of a mixture to detonation can be measured by a parameter named detonation cell width (λ), the smaller the cell size the more sensitive to detonate [96]. Figure 2.7 shows a pattern for detonation cells for hydrogen/air mixture. Detonation parameters, pressure and velocity, depend on fuel to air ratio in addition to initial pressure and temperature. Table (2.1) shows the pressure, velocity and cell width for stoichiometric fuel with air and oxygen at ambient condition (298K and 1.01325bar) [97].

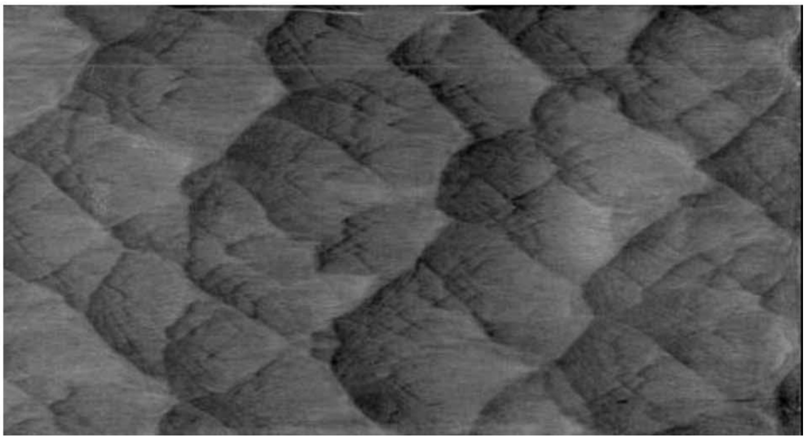

Figure 2.7 Cellular pattern on sooted foil created by hydrogen/air mixture at 20kPa [97]**.**

Table 2.1 Detonation parameters for stoichiometric mixtures at ambient conditions [97].

Fuel	Volume %		u_{CJ}(m/s)		p_{CJ}(bar)		λ (mm)	
	Air	Oxygen	Air	Oxygen	Air	Oxygen	Air	Oxygen
Hydrogen	29.6	66.7	1971	2841	15.6	19.0	6-10	1-2
Acetylene	7.75	28.6	1867	2425	19.1	34.0	10-15	0.1-0.2
Ethylene	6.54	25.0	1825	2376	18.4	33.7	24-26	2-3
Ethane	5.66	22.2	1825	2372	18.0	34.3	50-59	1-2
Propane	4.03	16.7	1801	2360	18.3	36.5	40-60	0.5-1
Methane	9.48	33.3	1804	2393	17.2	29.6	250-350	2-4

2.8.1 Hydrogen

As it seen in table (2.1), hydrogen has a smaller cell size than other hydrocarbons in air, and then it is more likely to detonate. For that, hydrogen poses the major concern in safety studies when the probability of deflagration to detonation transition is taken into account [87]. Another important factor influencing detonation is the detonability limits, mentioned above in section 2.7.1. While the cell size depends mainly on fuel and diluent concentration, and initial conditions, detonability limits depend on both initial and boundary conditions for certain fuels.

Eder et. al. (2000) [98] used hydrogen and air experimentally to investigate lean detonation limits of hydrogen based on the mixture composition and geometry of the detonation tube. A coaxial shape pipe was used in the experiments, the gap between the inner and outer pipes was filled with varied temperatures oil controlled by a heating cable. Obstacles with different blockage ratios, in addition to spacing and total length, have been also used to promote turbulence. Optical measurement techniques as well as conventional ones have been used to detect and record transition processes. They concluded that the initial conditions have more influence on the transition phenomenon than boundary conditions. The propagation velocity essentially is influenced by the heat flux to the confining walls. Also, they found that the peak pressure of supersonic deflagration can be twice higher than the detonation peak pressure, therefore they stated that “detonation is not the most dangerous combustion mode” [98].

Meyer et al. [81], used H2/Air in different configurations to enhance the transition from deflagration to detonation They concluded that between detonation limits, the equivalence ratio affects the location of transition rather than its nature [81]. The flame propagation of stoichiometric hydrogen-air mixture and its transition to detonation has been studied experimentally and numerically by Rudy (2011) [99]. Different configurations with different blockage ratio obstacles at atmospheric conditions were used. Detonation velocity stability has been found to be highly affected by obstacle configurations. Increasing the spacing between the obstacles decreases the differences between the velocities. This difference seems obvious for higher blockage ratio. The reduced reaction kinetic mechanism used in numerical simulations caused unconformity for quantitative comparison with experiments for detonation wave propagation. However, there is a good congruence between numerical results and experiment [99].

Table 2.2 Flammability limits of hydrogen in air and pure oxygen [100]**.**

Oxidiser	Flammability Limits, vol%		Detonability Limits, vol%	
	Lower	Upper	Lower	Upper
Air	4.0	75	18.3	59
Pure Oxygen	4.5	94	15	90

Using pure oxygen with hydrogen increases detonation probability, as it reduces the cell size and widens the detonation limits. Hydrogen-oxygen was the preferred combustible mixture in many studies [81], [86], [100], [101], [102], mainly because of its simplified chemical kinetics. Besides H_2/O_2 has lower ignition energy required for the trigger [103]. It has been shown numerically that there is a minimal concentration of hydrogen to achieve fast deflagration, which is inversely proportional to the mixture initial temperature. In order to ensure deflagration to detonation transition, hydrogen concentration must be higher than the minimal concentration [56].

2.8.2 Hydrocarbons

Although hydrogen has a low detonation cell size, hydrocarbons have higher detonation pressure, especially when they detonate with oxygen as an oxidiser (see table 2.1). Detonation of hydrocarbons is of particular importance for real life applications related to process industries.

Fuel composition has a greater effect on flame speed and transition to detonation in hydrocarbons fuels than in hydrogen. Chatrathi et. al. (2001) [105], performed experiments for different fuels at different equivalence ratios, using one pipeline system. They found that for hydrocarbon fuels the flame speed accelerates rapidly near the stoichiometric range. When the equivalence ratio goes further from stoichiometric condition, the rate of acceleration declines until the flame speed drops significantly and the flame quenches. On the other hand, hydrogen sustains detonation for an equivalence ratio range of 0.79 to 1.59 [105].

Stoichiometric methane-oxygen mixtures diluted in nitrogen were used by Ciccarelli et.al. (2013) [70] to investigate flame propagation and bead layer top surface influence in a smooth and rough surfaces rectangular channel for different initial pressure. For a smooth-walled channel, it is the piston action of the combustion products that limits the flame speed to the products speed of sound. In a very rough-walled channel, it is the sidewall boundaries that drive the flame acceleration and thus it is not limited to the sonic back boundary. Once the front velocity is sufficiently fast there is a transition to a direct shock ignition mechanism. It is shown that the interaction of transverse pressure waves generated at the rough wall governs the propagation mechanism, not the boundary layer turbulence. The transverse waves and its frequency appears to play a role in supporting the detonation wave.

Kundu et.al. (2016) [106] discussed the parameters that influence methane-air explosions phases, deflagration, detonation and transition stage respectively. The paper highlights the summary of results from several researchers that investigated the impact of the concentration, initial conditions, ignition, obstacles and geometry on flame acceleration and potential transition to detonation. It is found that the explosion pressure reaches its maximum value at methane concentrations of about 9.5%, figure 2.8. Even though the maximum pressure of explosion is affected by initial temperature, it falls down with initial temperature rise. It is found that the initial pressure does not influence the maximum explosion pressure, but it does increase the upper explosion limit [84], [105]. However, at elevated initial pressure the probability of detonation in hydrocarbon fuel is almost equal to hydrogen-air detonation [107].

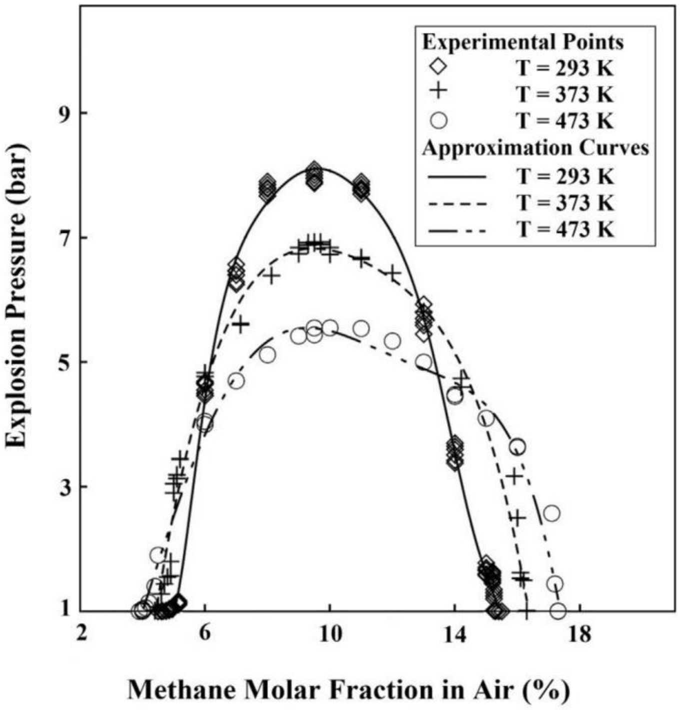

Figure 2.8 Explosion pressure of methane/air mixture for different initial pressure [106]**.**

Detonation sensitivity can be measured using detonation cell size. Hence, acetylene (C2H2) has been involved in many detonation research efforts for two reasons. First, it has a smaller cell size compared to other hydrocarbon fuels and hydrogen. Second, acetylene has flexibility regarding wide detonation limits[107][108].

2.8.3 Hydrogen/Hydrocarbons Blends

Promising combustion performance of hydrocarbon/hydrogen blends directed attention toward their use in combustion applications. The presence of hydrogen in hydrocarbon blends works on widen flammability limits and increase the flame stability range. Adding hydrogen will increase the probability of explosion, detonation in particular, in pipeline systems as it reduces the DDT length and the auto ignition delay time and increase the flame speed [109].

The influence of adding methane to stoichiometric hydrogen-air mixtures on the detonation cell size was investigated using smoked foil techniques by Porowski et al. (2011) [110]. Matlab application subscripts 2D Fourier transform were used to calculate the average detonation cell size. They found that adding 10% of methane to the hydrogen air mixture increased the cell size three and a half times of the cell size of hydrogen air mixture [110]. Zhang et al. (2016) [111], used the same technique to register the cellular detonation structure. They introduced ZND induction zone lengths to explain the difference of the cell size for three cases of combustible mixtures. Three different compositions of methane-hydrogen-air mixture (stoichiometric, higher content of methane and higher content of hydrogen) were used in circular tubes with three annular gap configurations at 293K and different initial pressures. Depending on the recorded cellular detonation structure, the detonation was found to become stronger as the hydrogen content increased in the mixture, and it reaches the onset of detonation limits earlier with an increase of concentration. They concluded that the cell size is smaller for higher methane content mixture for the same condition, and the cell size decreases when the initial pressure increase [111].

The effect of diluent types and their concentration, in addition to equivalence ratios and initial pressures, on the time required for detonation development (DDT time) has been investigated by Schultz et al. (1999) [112]. Hydrogen, ethylene or propane fuels were investigated individually with oxygen as an oxidiser and diluted by argon, carbon dioxide, helium or nitrogen. The DDT time for ethylene-oxygen was found to be the shortest among the three fuel types. As it was mentioned in section 2.7.1, this time decreases with initial pressure increase.

Although the dilution of fuel-oxygen mixtures reduces thermal energy, it changes the mixture heat capacity and as a result it peaks combustion temperature. For that, the molecular mass of the diluent has a great effect on DDT time. So, helium dilution causes the detonation velocity to increase and therefore decrease the DDT time, while carbon dioxide increases DDT time and significantly inhibits deflagration to detonation process [112].

2.8.4 Natural Gas

Safety concerns related to explosive gas mixtures that form in coal mines and in the pipeline system initiated many studies to address deflagration to detonation transition. Natural gas- air mixtures are not high sensitive mixtures to be detonated, but in certain circumstances such mixtures can experience detonation. Natural gas composition, confining geometry and initial conditions have utmost importance on transition processes.

Methane forms 82%-99% of natural gas by volume, in addition to ethane, propane and other gases [113]. Natural gas- air mixtures have been used by Zipf et al. [114] and Gamezo et al. [113] in a 73m length and 105cm inner diameter tube to determine the detonation characteristics. In both sets of experiments, a plastic bag filled with stoichiometric methane-oxygen mixture has been used to initiate the detonation. The normal flammability limits of methane (5% to 16%) was almost encompassed by detonation limits. The minimum average cell size, 20-30cm, was produced slightly above stoichiometric conditions, 10-11% of natural gas in the mixture. The cell size is about double at the lower limits and reaches up to four times at upper limits.

Turbulence produced by obstacles has also great effect on the flame acceleration. Kundu et al.[106], discussed various types of obstacles employed to understand the characteristics of explosion. Blockage ratio is the common and the most important parameter for all obstacle types. Still, parameters like length and pitch must be considered for construction of Shchelkin spirals as an example. This particular obstacle has an enormous effect on explosion characteristics of methane-air mixtures. Orifice plates, various shape obstacles and even wall roughness and their relation to transition time and distance, especially for methane, are well discussed by other researchers [106].

2.8.4.1 Usage of Shale for Detonation

Shale gas consists mainly of methane, for that it is not an easy process to detonate it. Using pure oxygen as an oxidiser will reduce the detonation cell size and enhance detonation characteristics. In addition, a proper geometry with suitable obstacles can have a tremendous impact on flame speed and lead to shorten the DDT distance. However, the presence of other gases in the shale gas composition affect detonation in different ways. Hydrocarbons, such as ethane and butane, and other alkanes in shale gas composition increase detonation chances [115]. In contrast, inert gases, carbon dioxide in particular, inhibits detonation transition or at least highly increase the DDT time [112].

Stamford and Azapagic (2014) [116] proposed three cases for shale gas composition, they named it as best case, central case and worst case depending on the parameters they considered in their study. Methane concentration ranging between 73% in the best case to 55% in the worst. Methane concentration decrease in the central and worst case is accompanied with an increase in more sensitive to detonation hydrocarbons and decrease in carbon dioxide concentration [116].

Table 2.3 Shale gas composition as suggested by Stamford et al. [116]**.**

Best Case	Central Case	Worst Case
• CH_4 0.61kg/m^3	• CH4 0.555kg/m3	• CH4 0.5kg/m3
• C_2H_6 0.04kg/m^3	• C2H60.075kg/m3	• C2H6 0.11kg/m3
• C_4H_{10} 0.04kg/m^3	• C3H8 0.05kg/m3	• C3H80.105kg/m3
• Other alkanes 0.02kg/m^3	• C4H10 0.02kg/m3	• Alkanes 0.04kg/m3
• CO_2 0.13kg/m^3	• Alkanes0.03kg/m3	• CO2 0.1kg/m3
• He 0.001kg/m^3	• CO2 0.115kg/m3	• H2S 0.09kg/m3
• Hg 2×10-7kg/m^3	• H2S 0.045kg/m3	• N2 0.03kg/m3
• Rn 400Bq/m^3	• N2 0.03kg/m3	• He 0.001kg/m3
	• He 0.001kg/m3	• Hg 2×10-7kg/m3
	• Hg 2×10-7kg/m3	• Rn 400Bq/m3
	• Rn 400Bq/m3	

2.9 Crack Propagation in Shale Rock

Unconventional gas and oil is the gas and oil needs unconventional methods to be extracted. As this unconventional gas is trapped in the petroleum source rock in minuscule spaces, production of commercial quantities of shale gas from one wellbore have been assessed via two specific techniques, horizontal drilling and fracturing. Although there are many studies have been dedicated to find reliable and efficient methods of modelling fracture system, it was indisputably proved that there are no two shale deposits are alike even along a wellbore [117]. Moreover, the hypotheses adopted by the researchers distorted their results from reality. Assumptions such as dealing with the shale as an isotropic material and ignoring the crack branching and natural fractures already existed in the formation [118].

Studying crack propagation in materials is part of fracture mechanics, which was first developed by Griffith in 1921 [119]. Griffith (1924) [120] stated that rupture surface is produced when stress generates enough energy to exceed a threshold [120]. Thereafter, Irwin in 1957 [121] introduced Stress Intensity Factor (SIF) as the stress intensity in the vicinity of crack tip caused by remote or residual stresses. SIF is associated with crack growth rate and it indicates the failure criteria due to fracture [121]. The Linear Elastic Fracture Mechanics (LEFM) theory stated the threshold of crack growth for brittle materials as [118], [122],

$$\mathbf{K_I \geq K_{IC}} \qquad \textbf{Equation 2.16}$$

where K_I is stress intensity factor and K_{IC} is the critical stress intensity factor, also known as fracture toughness. Fracture toughness is a measured material property, found by loading standard specimens until crack extends. SIF is usually expressed as,

$$\mathbf{K_I = C\sigma\sqrt{\pi a}} \qquad \textbf{Equation 2.17}$$

where σ is nominal stress in N/m^2, a is crack length and C is constant depending on the crack geometry [122].

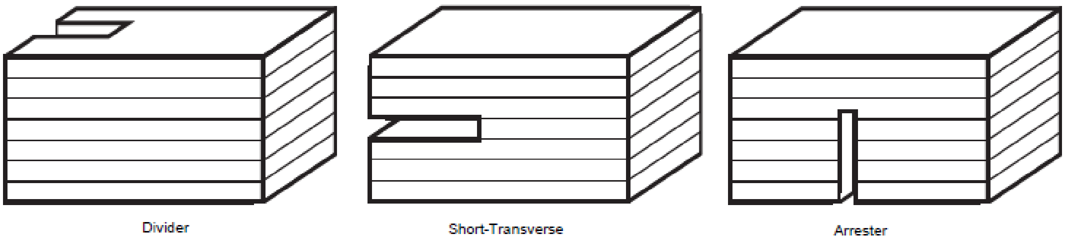

Figure 2.9 Crack plane orientation relative to bedding plane [123]**.**

Chandler et. al. [123] reported the fracture toughness measurements on Mancos shale for three different fracture orientations, as seen in figure 2.9. It is found that the fracture toughness is lower with crack plane parallel to the bedding, and cracks trend to deviate towards parallel bedding orientation [123]. Moradi et. al. [124] have studied the crack width, crack opening displacement (COD), in hydraulic fracturing. It is demonstrated that the COD is the “key parameter” for a successful hydraulic fracture, as it provides a route for proppant to access and also proportional to oil and gas production rate. Furthermore, they presented a model dealing with interaction between hydraulic fractures and natural fractures already existed in the formation. It is found that the propagation path is changed or even completely disappeared by natural fractures [124].

Zeng, YiJin et.al. [125] proposed a numerical model comprises the interaction of hydraulic fractures stage spacing and the wellbore stress redistribution. The redistribution of stresses induced by a certain stage fracturing parameters may activate complex natural fractures in the direction of horizontal wellbore. On the other hand, only minor change in stresses were found in the direction perpendicular to the horizontal wellbore [125]. Many factors, like crack deflection, crack surface friction, material anisotropic and crustal stresses, influence the interaction between fracture and crack propagation, branching and direction. Zeng X. et. al. [126] have given an explicit formula depends on crack surface friction and crustal stress to express the critical conditions that deflects hydraulic crack into weak interfaces. Applying their theory to real hydraulic fracture problem, the researchers concluded that further increase in hydraulic fracturing pressure introduces shearing crack mode rather than opening crack mode. Hence, in this mode of crack the crack propagation does not influenced by crack surface friction or crustal stress [126].

2.10 Health and Safety in DDT

Safety considerations were an important motivation for many researches to investigate deflagration to detonation transition. Although detonation is the most devastating accidental explosion event that could develop, incidents in industry are generally low compared to other potential hazards. The major conundrum of detonation lies in the inability to predict whether and where detonation will develop or not using any proven scientific method. Besides, the extreme pressure and potential damage which would be greater in localized regions are a major concern. Unfortunately, risk cannot be completely eliminated in combustion processes, thus there are criteria as to what is an acceptable risk level. The best accepted way to reduce risk is to reduce the consequences.

Enormous dynamic loads run with high pressure and velocity, along with the absence of general rules and imagining the consequences of damage made detonation experiments one of the most dangerous experimental approach in combustion, herein must be replete with warning and safety equipment. Pressure and temperature detection instruments, pressure relief valves, flashback arrestors and other equipment with purge and venting processes are essential appurtenances in any rig or system prepared to hold detonation experiments.

Consequently, different risk assessment models must be applied to predict and analyse the potential cause and consequences of each hazard to humans and facilities. Meanwhile, it is highly significant to provide appropriate protections and recommendations for optimizations of any project. Indeed, all of these actions could improve and ensure health and safety effectively in the workplace.

2.10.1British and European Legislation

In order to ensure safety of employees and others in the work place, large number of fire and explosion regulations and legislations have been introduced. Excluding, or at least reducing, the risks and hazards of dangerous substances and processes is the main issue to be addressed by such legislations. In 1974, the Health and Safety at Work Act was set up by the Health and Safety Executive (HSE) in the United Kingdom to ensure the occupational health, safety and welfare at work.

Working in explosive atmospheres, or with explosive materials, is a matter covered by wide range of legislations in the United Kingdom and Europe [127]. The Control of Substances Hazardous to Health 2002(COSHH) and Dangerous Substance and Explosive Atmosphere Regulations 2003 (DSEAR), are one of the MUST DO risk assessments in Cardiff University laboratories. Control measures equipment and personal productive equipment are compulsory to be used with explosion and detonation experiments. DSEAR implements the ATEX user directive, which targets work places containing potentially flammable and explosive atmosphere to be provided with safety equipment.

The main objective of all such legislation is to identify hazards and to mitigate the associated risks by describing the procedure that must be carried out in case of hazardous conditions [128]. In addition, it focuses on encouragement of positive human behaviour and correct reaction in case of an accident to achieve the requirements of health and safety. One of the well known quantitative risk assessments is HAZOP, hazard and operability study, which is a structured analysis used to identify design defects and its consequences. Despite the fact that this type of risk assessment entails considerable time, it helps to assess and record all deviations from design intent that will create risk and hazard, thus allowing prompt correction.

2.10.2 HAZOP

A hazard and operability study (HAZOP) at the detailed design stage can be considered as an important element in any system to prevent major accidents in the plant or during operation. A HAZOP study is a systematic technique to “identify potential hazards and operability problems caused by deviation from the design intent of both new and existing process plants” [129]. The word hazard is defined as any source of potential harm or adverse health effects on something or someone under certain conditions, while operability refers to the ability to maintain a whole industrial establishment or a system in it, in a safe and reliable operational condition. Deviation refers to any aberration from the agreed-upon design, and the design intent describes the concepts and criteria for the design [129].

Potential hazards and operational problems are identified using the HAZOP in terms of both plant design and human error. Essentially, every part of a process is methodically asked to find out how deviations from normal operation happen and whether further protective measures, change in operating procedures and design are required [130].

To carry out a HAZOP study, a complete design with design intent and a detailed P&ID schemes are needed. However, this study should preferably be carried out as early in the design phase as possible in order to have influence on the design. For all of that, the HAZOP should represent the final step of the detailed design which will check it. The main objective of the HAZOP is to identify the cause and the consequences of reckoned faults of equipment and conjugated interfaces in the complete system.

As a first step for the HAZOP study, the process flow diagrams, piping and instrumentation diagrams (P&IDs) and layout diagrams should be available, in addition to the following information:

- Material safety data sheets.
- Provisional operating instructions.

- Equipment data sheets.
- Start-up and emergency shut-down procedure.

The key element of the HAZOP are [130];

- HAZOP team
- full description of process
- relevant guide words
- conditions conducive to brainstorming
- recording of meeting
- follow up plan.

The HAZOP team

A HAZOP team should consist of approximately five to seven members [131]. A chairperson should be an independent member and have no responsibilities for the process and the operation performance. One of the main responsibilities for the chairperson, who should have a very good experience in HAZOP techniques, is to choose a skilled team. This team must contain a technical secretary, Engineering disciplines, management, and plant operating staff, all should possess a good understanding of the plant and its operations to ensure all aspects are covered.

The secretary will be responsible for preparing the HAZOP worksheets, recording the discussion in the HAZOP meeting and preparing draft reports. A good HAZOP participant should be active and avoid endless discussion of details, everybody's contribution is important, and they have to be responsible.

Full description of process

Process and Instrument Diagrams (P&IDs), which is also known as Engineering Flow Diagrams, represent the essential information needed in the HAZOP study. A member of the HAZOP team, at least, should be an expert knowing these diagrams and all symbols and instrumentations represented on them. Not all information will be available on the

P&IDs, therefore, it is necessary to have full details of all instrument specifications and definitions, as well as pipeline size and design parameters and working properties, like pressure, temperature, flow,…etc.

Other information should be also available and might be required during the HAZOP study, i.e. layout and site plan drawings, safety data sheets, relevant code and standard and operating, start-up and emergency shut-down procedures. However, only the P&IDs are going to be reviewed and all the other drawings and documents are used for reference purposes.

Relevant guidewords

The relevant guidewords (also known as key words) can be divided into two types, primary guidewords (also known as parameters) and secondary guidewords. The primary guidewords are a particular aspect of a design intent related to a process condition or parameter, mainly related to safety or operability. For example, some of the safety guidewords are temperature, pressure, flow, level,…etc., while operability guidewords are isolate, maintain, drain,….etc.

Secondary guidewords refer to possible deviations of the design intent that might happen during the process. These guidewords tend to be a standard set. The success of the HAZOP in the detection of design and operability problems is highly influenced by the choice of suitable guidewords [130]. Guidewords help the team members to imagine the deviation of the design intent, by applying them, in turn, to all the parameters, or primary guidewords, for every process line within the P&ID, in order to identify unexpected faults from the design intent.

Basic HAZOP secondary guidewords are:

- No: which refers to none of the design intent is achieved, also mentioned as not or none.
- More: refers to an increase in the parameter quantity, also mentioned as more of or higher.
- Less: refers to a decrease in the parameter quantity, also mentioned as less of or lower.

- As well as: refers to occurrence of an additional activity accompanying the design intent, also known as more than.
- Part of: when only a part of the design intent is achieved.
- Reverse: refers to the incidence of opposite of the design intent.
- Other than: when completely another activity is happening, also known as other.
- Sooner than: when the activity takes place before the design intent, also known as early.
- Later than: the activity appears too late for design intent, also known as late.
- Where else: the design intent happens in a different place.

Conditions conducive to brainstorming

As a risk assessment tool, a HAZOP is often described as a brainstorming technique [132]. Brainstorming is considered a powerful technique especially with a group of people, as it creates new ideas, solve problems, motivates and develops teams. However, brainstorming is not a simple and random activity, it needs to be well-organized. Brainstorming involves all team members and it gets them working together. All ideas are managed and structured by the chairperson. Also, the chairperson has to encourage every member to be involved and effective.

Structured brainstorming sessions stimulate the fanciful thoughts for a HAZOP, which will ensure that the deviation of design intent is comprehensively studied [133].

Recording of meeting

There are many approaches that have been developed by companies to record meetings and document HAZOPs. These approaches can be fall within two major categories [130]:

- Recording by exception.
- Full recording.

The first way refers to record only the key findings. This approach looks to record the negative consequences accompanying the potential deviations. Although, this way of recording reduces the time taken in both meeting and the subsequent HAZOP report, the produced analysis would be hard to be described.

In order to produce a full and comprehensive report, which will include all deviations and causes, the second approach might be used. This way of recording demonstrates unambiguously that a rigorous study has been carried out. Each guideword combination is applied to every process line within the P&ID and followed by “no Cause could be identified, No action required existing - safeguards considered adequate, or alternatively that no Consequence arose from the Cause recorded” [129].

Nowadays, the second approach is considered to be more appropriate to record HAZOP meetings, as it eliminates the time issues mentioned earlier with the use of a computer. Besides, this kind of reporting makes it easier to perform assessment of the safety for future process modifications.

2.10.2.1 HAZOP Limitations

It is a fact that a HAZOP incorporates general experience available for the team involved in the study, and gives excellent identification of critical deviations and its causes associated with hazardous effects to people and working environment. However, the primary limitation of this kind of study is that, it is time consuming, as it requires long time to be performed. Also, the tendency to look at many insignificant consequence deviations. The team decides whether the deviations are meaningful depending on their own collective experience. They have a propensity to disregard interventions of the operator. Finally, a HAZOP study does not take in account the occupational or chronic hazards [134].

CHAPTER THREE

Conceptual Design

3.1 Introduction

This chapter describes the system proposed to be used for increase of pressure at variable frequencies in order to crack shale rock for gas extraction. Thereafter, the detonation tube rig setup, with equipment and measurement instruments are laid out and briefly described. The normal procedure to supply the system with fuel blends and pure oxygen for the experimental work is provided, so as the abnormal procedure for the cases of ignition failure or any other system fault.

Finally, the risk assessments (HAZOP, DSEAR and COSHH) for the system and environment are assessed and presented in this chapter.

3.2 Design of Non-Aqueous Appliance

The system is a device that enables the use of pulse detonation for the increase of pressure (and temperature) at variable frequencies in order to crack shale rock for gas recovery. The concept has been developed from the notion of a topic called “Explosion/Propellant Systems EPS” for non-aqueous shale gas exploitation, using state of the art systems to improve efficiency and reduce environmental/social concerns.

The use of new alternative fuel sources at large scale will be a reality in the near future as oil and conventional fossil gas depletion in several parts of the world are becoming more significant. The increase of energy prices and the lack of supply have triggered various political and economic issues around the world, denoting the complex nature of this problem. Thus, governments and energy suppliers have look at the possibility of exploiting a fuel source that is highly available all around the world, shale gas.

However, the exploitation of this resource is highly controversial, as it requires a process called Fracking, which uses high amounts of water and ~2% chemicals for the extraction of gas. The likelihood of earthquakes and the damaging effects to the environment have started social movements against the process, especially in regions such as Europe where the community feels high responsibility towards climate change and environmental improvement.

The concept of explosions in the shale wells has been studied for over 130 years [135]. Most of the attempts have been based on the use of explosives (i.e. TNT, grenades, rocket propellants, etc.) under water, with very poor control on the process. Moreover, single explosions tend to produce just minor cracks in the geological structures, as the propagation of the waves is limited to a very short time interval and high amplitudes [136]. However, the technique is considered as being environmentally friendly for shale gas and shale oil extraction giving better return on investment (ROI). The EPS has none of the impacts of hydraulic fracking such as fluid compatibility, wettability, formation heavy and light metal leachates, smectite expansion, that lock up the fractures with hydraulic fracking.

Thus, the use of a system capable of improving the efficiency of the process through the control of its pressure wave characteristics, frequency, amplitude and location could be of great benefit to the industry globally. Localised increase of the pressure wave amplitude or frequency could allow the propagation of longer cracks with higher extraction rates. The high temperature of the combustion gases would allow the higher diffusivity of the shale molecules towards the flue gases. In order to increase process efficiency, shale gas from the well could possibly be used as the main fuel in combination with pure oxygen fed from the surface. Variable pressure wave frequencies would enable matching to the natural resonance of different formations to be made, thus elongating the cracks and increasing shale gas extraction.

In order to reduce the size of the system, specially shaped tubes would be used to improve detonation, whilst a multiple ignition system would provide higher energy to the mixture to reduce the length of the transition process. An advanced cooling system would be required to provide mechanical and thermal integrity. At the tip of the device, axial vanes will be used to direct some shale gas inside of the system. The former will be compressed before being delivered to the detonation tubes. A blockage component at the end of the system would almost seal that particular region of the well, allowing for the build-up of pressure and temperature for the cracking of the shale rock. Development is still required for all these concepts, specially the cooling system, the short transition deflagration to detonation process and the improvement of shale gas recovery at high pressures. The system is illustrated in figure 3.1.

Figure 3.1 Non-aqueous acoustic aviator for shale gas recovery system.

3.2.1 Fundamental Concept of the DDT

Deflagration to detonation transition involves initiating a deflagration, the flame then accelerates due to turbulence provided by obstacles. Detonation is defined as a shock wave propagating at supersonic velocities. According to this, the deflagration must accelerate to a critical velocity so that the precursor shock strength is such that autoignition occurs in the shocked mixture.

The detonation front propagates into unburned gas at a velocity higher than the speed of sound, and is sustained by the energy released by the combustion process. As the traveling detonation wave is supersonic, the gas ahead of the detonation remains undisturbed. The chemical process releases energy and triggers a volumetric expansion of the burned gases which drives the shock wave. Thus, detonation is due to the confluence of hydrodynamic and thermo-chemical processes. A detonation wave in which there is a strong interaction between these processes is said to be self-sustaining.

3.2.2 Rig Setup

Several attempts have been undertaken to get the optimal design for the current system. The optimum adopted the best materials and a design that provides adequate safety and security factors. The first design trial was based on using three parts of seamless stainless steel pipes connected by flanges, figure 3.2. Multi parts were chosen in order to have the ability of changing the length of the shock tube to achieve the transition from deflagration to detonation. All diagnostics and ignition instruments were designed to be added by drill holes on the tube body.

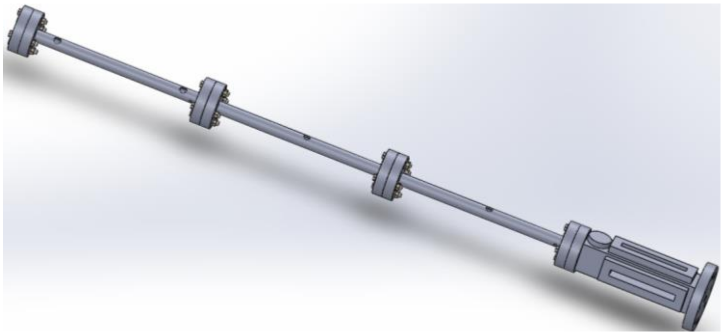

Figure 3.2 First design of detonation tube.

The high cost for constructing and material in addition to the HAZOP recommendations compelled us to look for alternative designs. HAZOP study suggested that making holes in the tube may create stress concentration points, which will create a high potential failure points. For all of that, a 316-stainless steel seamless tubing of 25.4mm outer diameter and 2.1mm wall thickness copes with working pressures up to 214bar, thus having sounded as the best option in terms of material and technical considerations, figure 3.3. Length and diagnostics instruments can be controlled using LET-LOK fittings.

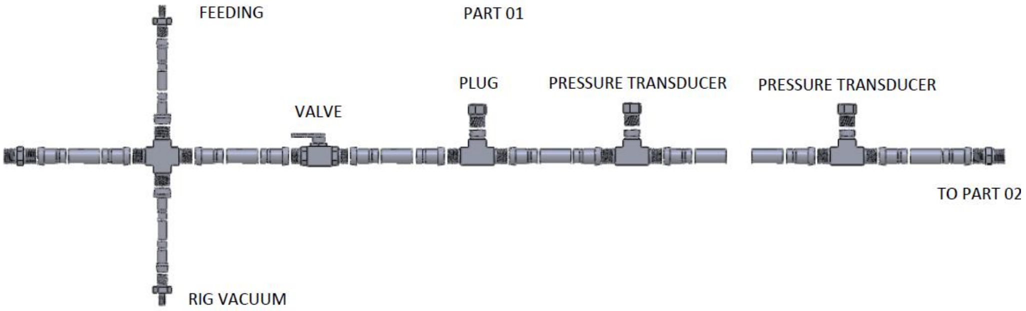

Figure 3.3 Final design of detonation tube.

Unfortunately, the time consuming HAZOP study occurred at the same time as a laboratory renovation and its refurbishment. This forced us to change the place of where the rig has been set up, and changed the layout of nodes 1 and 2 to fit the space and satisfy the risk assessments.

3.2.3 Rig Layout

The rig layout was built of a seamless circular stainless-steel pipe with 21.2mm inner diameter and 1500mm length to achieve the deflagration to detonation transition. The numerical data obtained by GASEQ and CHEMKIN were used to predict the maximum values for the pressure, temperature and other parameters, which were used to choose the pipe specifications and mixture composition in the first experiments. The data obtained by OpenFOAM has guided us for the best selection of obstacles.

A HAZOP study was performed for the experimental rig dividing it into four nodes. The first looks into delivering the fuel gases. Other part of this node is responsible for delivering pure oxygen into the main rig tube. The fuel mixture and pure oxygen are kept apart until they reach the main rig cylinder for safety purposes.

Node 2 is the mixing chamber and the pipeline responsible for delivering the fuel gases mixture into the shock tube. The mixing chamber is a cylinder where the mixture is left for about thirty minutes to undergo satisfactory mixing so that homogeneity is ensured. Node 3 is the main part of the experiment rig system. It consists of one inch (25.4mm) OD pipe with an exhaust/vacuum system used to get rid of the air in the rig prior to fill it with the combustible mixture and oxygen, or to exhaust a failed “to ignite” mixture. The last node is the burned gases exhaust and the diagnostic and ignition systems.

3.2.4 System Parts

All the parts used in the experimental rig are detailed below:

- Pipes

The pipes used in the experiments were circular seamless smooth stainless-steel pipes. The pipes are manufactured complying with ASTM A213, A269 316L specifications [137]. Two different diameters were used, a 3.65mm for delivering fuel gases and pure oxygen to a 25.4mm pipe where the experiments are held.

The wall thickness of the 6.35mm tubes is 0.91mm, with a maximum allowable working pressure of 359bar. For the 25.4mm pipe, the wall thickness is 2.1mm and the maximum allowable working pressure is 214bar.

- Pipe fittings

Most of fittings used are stainless steel 316 HAM-LET tube fittings with LET-LOK mechanism. The allowable pressure rating for the male and female tapered pipe thread ends are 552bar and 455bar for the 6.35mm pipe and 365bar and 303bar for the 25.4mm pipe [138]. Some NPT (National Pipe Tapered) or BSP (British Standard Pipe) are used to fit particular parts in the system.

- Flashback arrestor

For safety purposes, all lines containing combustible gas are equipped with flashback arrestors. The flashback arrestors offers the following safety elements:

- A flame trap.
- A contamination filter.
- A flame arrestor.
- A non-return valve.
- A temperature activated cut-off valve.

Flame arrestors work to quench the flame front and prevent the flame from travelling back to the gas source. Also it works as a low pressure none-return valve designed to prevent the backflow of gas. Figure 3.4 is a longitudinal section of flashback arrestor used in designed rig.

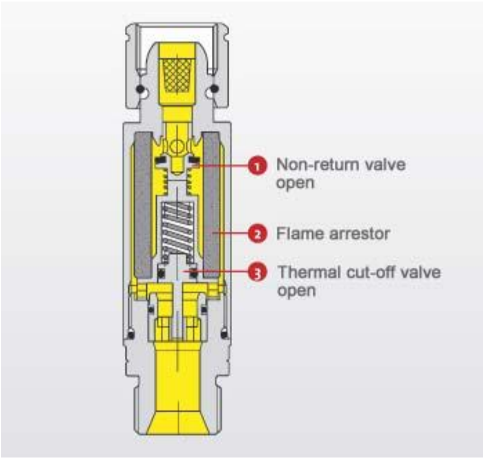

Figure 3.4 Flashback arrestor [139]**.**

- Check valve

Check valves used in this experimental system are HAM-LET H-400 series, shown in figure 3.5. It provides an accurate operating point, mean allowing working pressure (MAWP) of 207bar. This type of valve is normally closed. Initial flow passes when the differential pressure between inlet and outlet reaches 0.02bar. The valve is made of stainless steel 316, the end connection is 6.38mm LET-LOK tube fitting.

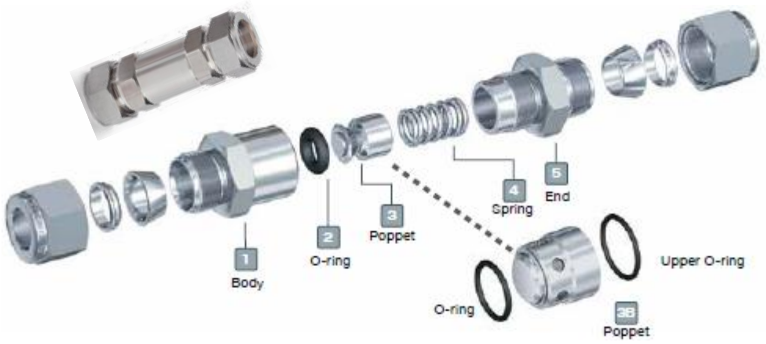

Figure 3.5 HAM-LET H-400 series check valve [140]**.**

- Relief valve

A high-pressure service relief valve HAM-LET H-900HP series is used here. This valve is intended to be used in high pressure applications, up to 413bar, and is constructed from stainless steel 316 with 6.35mm LET-LOK tube fitting end connection. The valve is normally closed, it will open when the system reaches the set pressure level, and re-closed when the pressure falls below that level. The nominal pressure range of the valve used in the present system is 3.4-24bar, set at 4bar.

- Needle valve

HAM-LET H-300U needle valves are used here, figure 3.6. The MAWP is 345bar with stainless steel construction. The valve has a 6.35mm LET-LOK end connection with a regulating stem to achieve a degree of flow control.

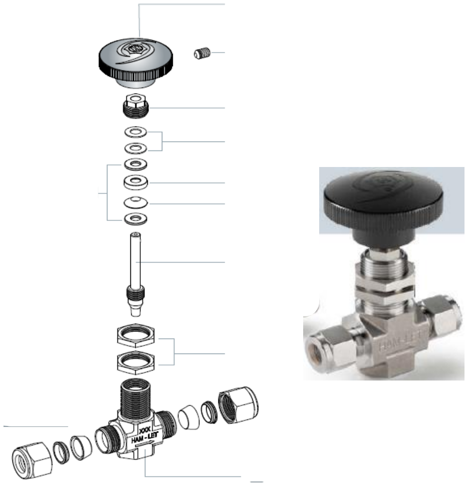

Figure 3.6 HAM-LET H-300U needle valves [140]**.**

- Rotameter

Two different meter specifications of Brooks Sho-Rate flow meters have been used in the current system. The fuel lines are equipped with 1355/D 150mm glass tube scale length and 316 stainless steel horizontal female 3.175mm NPT adapters. The flow range is 0.025 - 0.25l/min and the design pressure is 14 bar. The oxygen and carbon dioxide lines are equipped with 1355/G flow meters. Flow range goes from 0.25 – 2.5l/min and the designed pressure rating is 13.8bar.

- Pressure gauge

Two pressure gauges of direct bottom mount are used. One gauge where vacuum is required, the other gauge in the gas feeding lines. All gauges used are dry case stainless steel Burdon tube, with bottom entry and safety pattern glass window.

- Shut-off valve

Two-piece ball valve stainless steel 316 HAM-LET H-700 series have been used in nodes 1 and 2 of the designed rig. The valves are rated to a maximum pressure of 135bar.

In order to isolate the combustible gas mixture and oxygen feeding from the 25.4mm shock tube, a HAM-LET H-500 three-piece ball valve is used. This valve, figure 3.7, offers large ports for high flow, tight shutoff and low operating torque. It is a stainless steel 316 construction and bears MAWP up to 206bar.

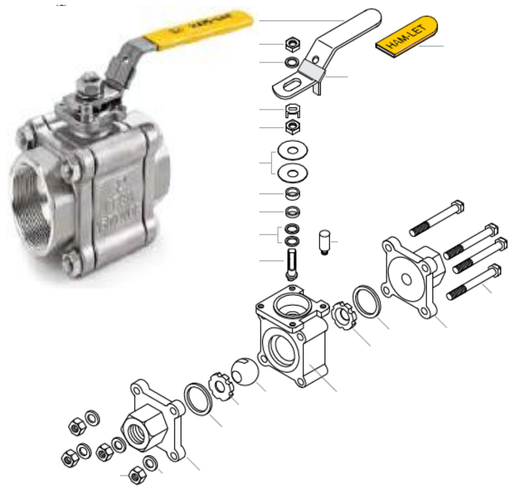

Figure 3.7 HAM-LET H-500 series shut-off valve [141]**.**

- Mixing chamber

All gaseous fuels and carbon dioxide are brought to a stainless steel 500cc sampling cylinder, figure 3.8. This cylinder works as an accumulation point that helps in mixing the fuel mixture and keeps the fuel lines as far as possible from the place where the fuel mixture will mix with the oxidiser. The cylinder used is seamless cold-finished stainless steel with NPT thread ends and an operating pressure rated to 124bar.

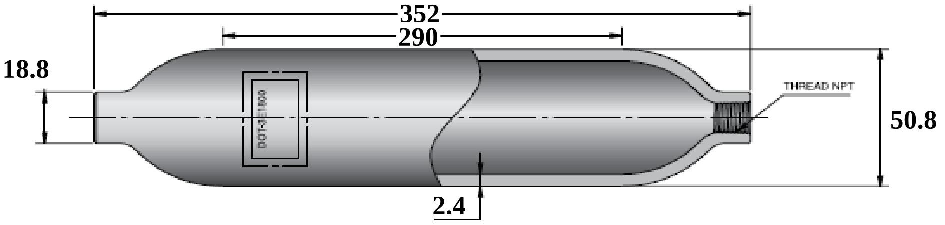

Figure 3.8 Sample cylinder used as a mixing chamber [140]**. (All dimensions in mm)**

- Ignition system

The premixed gas mixture is ignited using an ordinary automotive spark plug mounted at the beginning of the first section of the main rig body. A satronic ® ZT930 high frequency ignition unit is used along with the spark plug.

- Pressure diagnostics and data acquisition

The pressure along the detonation tube is measured using 211B4 PIEZOTRON Kistler pressure transducers, shown in figure 3.9. Pressure transducer is assembled with a cooling adapter and mounted to the detonation pipe through a machined pipe plug screwed on a female branch tee. The system used to record the signals from the pressure transducers is 5165A-Four-Channel Kistler LabAmplifier.

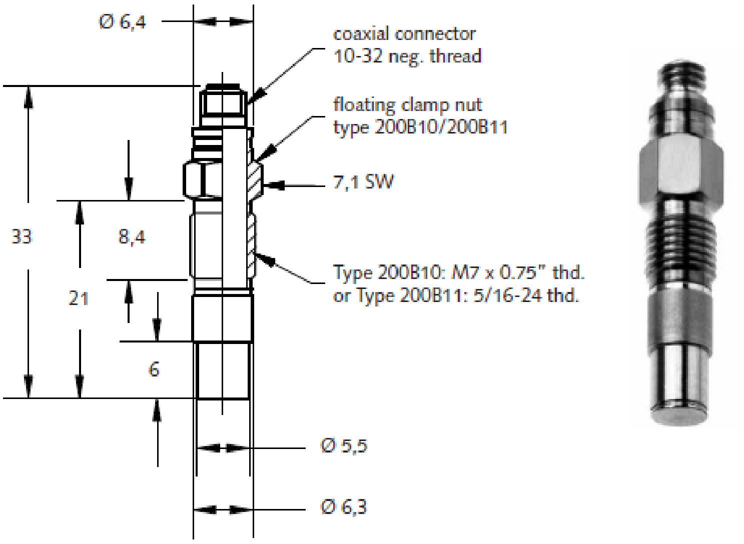

Figure 3.9 211B4 PIEZOTRON Kistler pressure transducer [142]**.**

3.3 HAZOP

In order to overcome any deviation from the design intent that could result in a major accident, a full HAZOP study has been conducted for the recent work. The HAZOP team was formed by Mr. Martyn Griffiths (School Safety Officer) as a chairperson, Dr. Agustin Valera-Medina (supervisor), Mr. Gareth Hunt (School Technical Services Manager), Mr. Malcolm Seaborne (Technician) and the researcher, in order to identify the cause and the consequences of reckoned faults of equipment and conjugated interfaces in the complete system. Starting with version one of a P&ID, figure 3.10, there were seven versions of the later along the HAZOP team meetings. More instruments and equipment were added every meeting to ensure safety, until the last version (version seven) had been agreed on, figure 3.11.

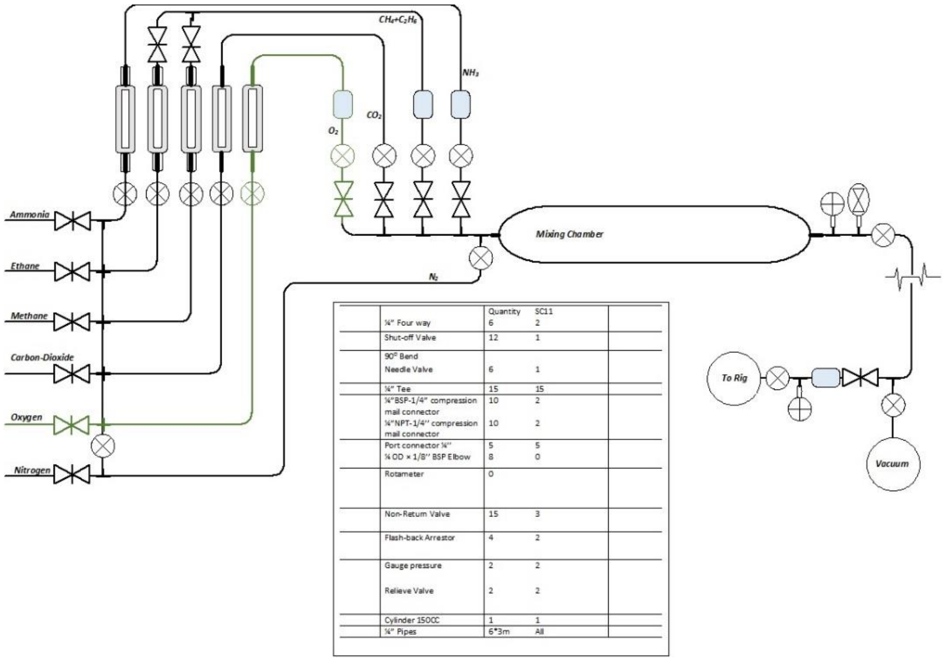

		Quantity	SC11	
	¼" Four way	6	2	
	Shut-off Valve	12	1	
	90° Bend Needle Valve	 6	 1	
	¼" Tee	15	15	
	¼"BSP-1/4" compression mail connector ¼"NPT-1/4'' compression mail connector	10 10	2 2	
	Port connector ¼'' ¼ OD × 1/8'' BSP Elbow	5 8	5 0	
	Rotameter	0		
	Non-Return Valve	15	3	
	Flash-back Arrestor	4	2	
	Gauge pressure Relieve Valve	2 2	2 2	
	Cylinder 1500C	1	1	
	¼" Pipes	6*3m	All	

Figure 3.10 P&ID for the first designed pipelines.

The engineering flow diagram has been divided into the four HAZOP nodes to simplify the HAZOP study and to conduct the study systematically from the cylinder regulators to the exhaust tank. A full description for every node provided as follows.

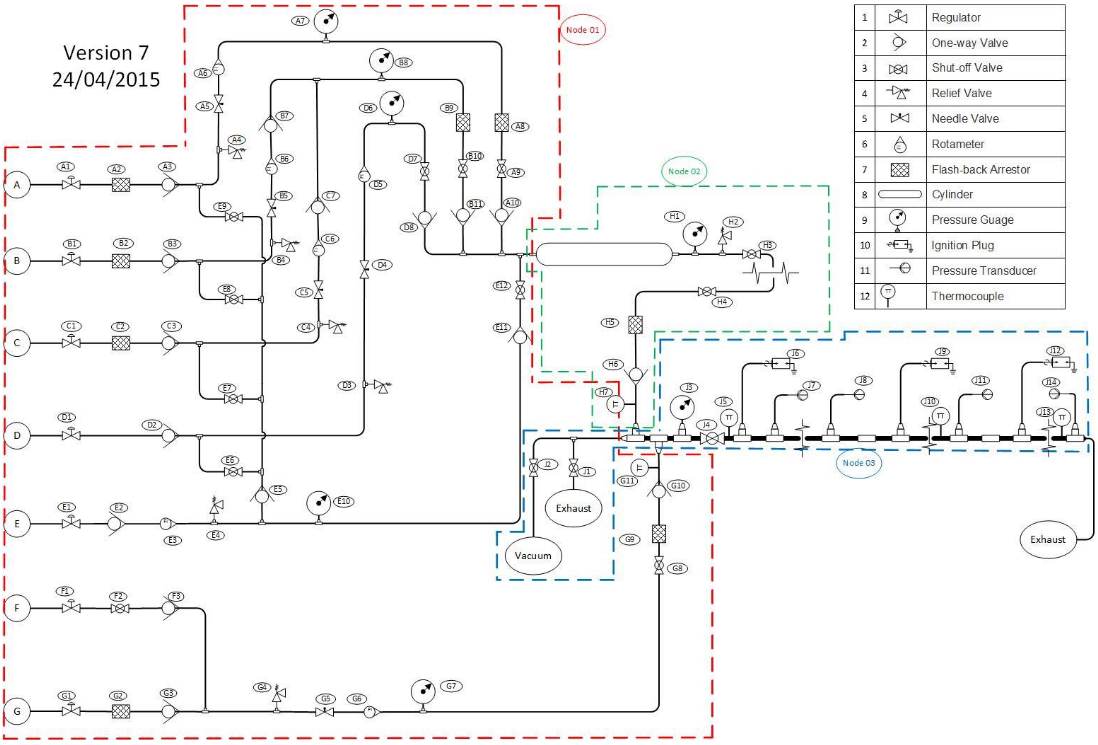

1	⋈	Regulator
2	▷	One-way Valve
3	⋈	Shut-off Valve
4	⋈	Relief Valve
5	⋈	Needle Valve
6	△	Rotameter
7	▨	Flash-back Arrestor
8	⬭	Cylinder
9	◔	Pressure Guage
10	▭	Ignition Plug
11	⊖	Pressure Transducer
12	TT	Thermocouple

Figure 3.11 P&ID for the assembled pipelines.

Relevant primary and secondary guidewords had been chosen by the team to cover all the expected deviation as much as possible. Parameters like pressure, temperature, ignition … etc., were examined periodically with the basic secondary guidewords like more, less, no … etc., to discover possible causes of deviation from the design intent and the consequences. The best protection and safeguard was to act with recommendations for improvement

3.3.1 Node 1

Node 1, the red dashed box in figure 3.11, is the pipeline which responsible for delivering the fuel mixture to the mixing chamber and the pure oxygen directly to the rig. At the beginning, all the pipelines, including the oxygen line, were feeding the mixing chamber. During the HAZOP study it was found that there would be a high risk of oxygen entering any fuel line. In addition, there would be risks of having an ignition in any place other than the designed exact location, inside the shock tube, node 3. For all that, it decided to separate the fuel lines from the oxidiser line until they reach the shock tube.

The node was subdivided into seven branches, a branch for every gas line. Ammonia, methane, ethane, carbon dioxide and nitrogen for purging all lines and for (purging the mixing chamber) all pour in the mixing chamber from one side. From the other side, an oxygen line with another nitrogen line pour immediately to the shock tube.

3.3.2 Node 2

The mixing chamber being used is a 500cc stainless steel cylinder. The shale blends will be mixed in this prior to injection to the detonation tube. This will provide a suitable location to enable all gases to mix completely for the required concentrations.

3.3.3 Node 3

The detonation tube, is a 21.2mm diameter stainless steel pipe and is where the ignition phase of the experiment. This is divided into four sections. The first section consists of an exhaust/vacuum aperture; the fuel mixture is delivered from an aperture with the oxygen coming in from another opening. The end of this part is finished with a 206bar shut off valve, which is used to prevent flashback reaching the gas supplies in the earlier nodes.

The final three sections are each of 500mm in length. Each part is equipped with an internal combustion spark plug at its beginning. These sparks plugs will provide the ignition for the experiment. Pressure transducers are distributed along the three sections.

This node also has the exhaust which is responsible for expelling the used propellants through a rupture disk to guarantee smooth and fast flow of exhaust gases to prevent back pressure building up in the main rig pipe.

3.3.4 Node 4

Node 04 consists of two parts. The first one is the rupture disc and the exhaust to the extractor system. The second part is the ignition system and measurement instruments. The ignition of the blend is facilitated through an ordinary automotive spark plug mounted at the beginning of the first section of the main rig body. A satronic ® ZT930 high frequency ignition unit is used along with the spark plug. A 211B4 PIEZOTRON pressure transducers are used to measure the pressure pulse, shown in figure 3.9. The transducers are distributed along the detonation tube as one immediately after the spark plug in the first section, and the second one is by the end of the first section. The two other transducers are at the middle of the second and last sections.

3.4 HAZOP Spread Sheet

Once the HAZOP parameters and guidewords are prepared and the P&ID sketch of the node under discussion is laid out, systematic questions are applied along each line of the P&ID. The results are recorded in a spreadsheet. System, part under discussion and the design intent for the part are mentioned at the top of the page followed by twelve columns. The guidewords applied for every parameter to determine the deviation and verify the cause and consequences. Measures are proposed to mitigate or at least manage risk. Likelihood, severity and level of risk for every step of the study is measured and recorded in the next columns. Table 3.1 shows the assessment of risk to health after additional control measures.

Table 3.1 The assessment of risk to health after additional control measures.

parameter	Scoring range	Scoring criteria
Likelihood of Harm	1-5	1-Very Unlikely 2-Unlikely 3-Likely 4-Very Likely 5-Extremely Likely
Severity of Injury or Illness	1-5	1-First Aid is adequate 2-Minor Injury 3-Three Day Injury 4-Major Injury 5-Fatal or Disabling Injury
Risk	1-25	1-5 Low (No further action required) 6-11 Medium (Appropriate additional control measures should be implemented) 12-25 High (Additional control measures must be implemented. Work must not commence until such measures are in place)

The next column is team recommendations to overcome the deviation followed by the person among the HAZOP team who is responsible for doing the recommendations and the timescale for doing them. The set of HAZOP spreadsheets are shown in appendix A.

3.5 Operating Procedure

One of the main subjects that HAZOP study has focused on was the operating procedure preparation. In order to minify risks, three types of procedures have been prepared, as follows.

3.5.1 First Run Procedure

Due to high rescue of detonation itself in addition to using pure oxygen as an oxidiser, periodic inspection for safety are highly recommended. Checking all pipelines, valves and safety equipment must be done before each run followed by a period of leaving the system. First of all, all pipe lines and fittings must be visually checked for any apparent defects or abnormal appearance. All pipes in the system must be pressurised, using nitrogen, slightly above the design intent pressure to be checked for any leak.

Instruments must be checked to ensure fully performance. Finally, all electrical connections must be checked, and the ignition system must be tested.

3.5.2 Normal Procedure

The experimental work is operated in single-shot mode. The pipelines are supposed to be filled with nitrogen from prior experiment trial. All valves are closed, shutoff valves are all in horizontal layout. The following procedure must be followed prior to each experiment.

Nitrogen is expelled from node 1 lines through node 2 to the exhaust opening at the beginning of node 3, refer to figure 3.11, by pushing the fuel gases and carbon dioxide through pipelines. In order to ensure using pure oxygen as the only oxidiser in the experiments, node 2 and node 3 are vacuumed through vacuum opening at the beginning of node 3. The desired amount of fuel gases is accumulated in node 2 (mixing chamber) before it moved to the main rig. For health and safety purposes, oxygen is added to the rig after purging node 1 and node 2 by nitrogen. Finally, oxygen line is purged with nitrogen and allow the nitrogen to flow into the exhaust tank, node 4. This will extinguish any fire might leave the detonation tube.

Experiment now is ready to be held in detonation tube, node 3. It is very important to check the exhaust burst disk, node 4, is not hampered or stuck by any means to avoid backpressure build up. Check all connections, electrical and measurement instruments, and press ignition button. When the test is finished purge the detonation tube with nitrogen to confirm it is free of any fuel gases or oxygen.

3.5.3 Abnormal Procedure

In case there was any problem happens anywhere during the procedure mentioned above. Any gases added to mixing chamber or detonation tube must be seeped out. When the fault occurs while adding fuel gases, purge all lines with nitrogen through the exhaust at the beginning of node 3. Otherwise, when the fault occurs while or before delivering oxygen to the system which means the fuel gases are already in the shock tube, purging is achieved throuh exhaust tank, node 4.

3.6 Risk Assessments

Conducting an experiment involves flammable gases with an oxidizer and an ignition source. Therefore, risk assessments and a meticulous procedure must be completed prior to the experiment taking place. This is to ensure that all risks involving the experiment are limited as much as possible, the safety of everyone present is assured and that the procedure will produce the best possible results whilst maintaining the upmost safety.

Regarding to this experiment, the risk assessments that must be addressed are the Control of Substances Hazardous to Health Regulations “COSHH”, Dangerous Substances and Explosive Atmospheres Regulations of 2002 “DSEAR” and ATEX risk assessments. COSHH regulations regard the need for the control of the possible exposure to hazardous substances to prevent health issues. DSEAR relates to the possibility of an explosive atmosphere forming and the necessary ventilation required. ATEX requires equipment and protective systems intended for explosive atmospheres to be designed and manufactured to minimize the occurrence and limit the severity of accidental explosion.

3.6.1 DSEAR Risk Assessment

Based on the DSEAR Regulations, the risk assessment in the work place should take into account all following parameters: the dangerous substances, the suitability of the space, appropriate equipment and protective systems, safety measures and emergency arrangements. The British standard for DSEAR states that protective measures must be applied in areas where concentration of flammable gases can be dangerous.

The DSEAR risk assessment aims to maintain the working area, where the experiment is held, below the lower explosive limit (LEL) of a particular gas in case of any accidental fuel leakage. This results in no explosive atmosphere being formed. This is achieved via calculating the magnitude of the mass flow rate of a flammable substance released from a pipe, ventilation rate and the volume over which this ventilation is required. The calculation results in the minimum space required to control the ignition source.

In the present experiments, five different gases are used, methane, ethane, carbon dioxide, nitrogen and oxygen. The two inert gases, carbon dioxide and nitrogen, are not required to be analysed. The oxygen is the oxidiser itself. Thus, the DSEAR analysis has been done for methane and ethane and is shown in appendix B1.

3.6.2 COSHH Risk Assessment

A COSHH risk assessment aims to protect people against risk to their health arising from exposure to hazardous substance. It looks into the potential of harmful substances during the experiment, the measures to prevent these issues and measures to deal with any problem if it does happen. Risk consideration created by hazardous substances must be written in the COSHH assessment, with procedures that need to be followed to prevent or adequately control any exposure. Particular care must be taken with the introduction of new substances and new processes/experiments.

The COSHH risk assessment for the present experimental system are shown in appendix B2.

CHAPTER FOUR

0-D & 1-D Numerical Analysis

4.1 Introduction

The use of computational means to simulate complex combustion processes before experiments provided stronger background for a more robust design. The effect of change in initial conditions or reactants composition on final equilibrium properties and products species concentration are well predicted using chemical thermodynamics and kinetics.

Numerical solutions using NASA chemical equilibrium software GASEQ with three composition scenarios proposed by literature have been conducted. The same composition scenarios have been analysed using chemical kinetic software CHEMKIN-PRO. The specific setups for computations performed using GASEQ and CHEMKIN-PRO in recent works are described. Thermodynamic properties of products are calculated for different fuel fractions of the total reactants volume. The three shale gas compositions scenarios/pure oxygen mixtures are compared with hydrogen/air mixture for design purposes.

4.2 GASEQ

GASEQ is a Microsoft Windows programme written in Visual Basic 3 used to calculate chemical equilibrium for combustion and other processes. The combustion calculations are made on the basis of thermodynamic equilibrium and minimisation of the free energy equation [143]. GASEQ can be used to predict the effects of initial conditions and composition on equilibrium reaction with the final product parameters and species concentrations. As seen in figure 4.1, reactants, initial pressure, temperature and set of products must be introduced to GASEQ. The initial (reactants) and final (products) thermodynamic properties for the defined process are then calculated.

4.2.1 GASEQ Description

Chapman-Jouguet detonation is one of the problem-solution types GASEQ deals with, thus species of three shale gas composition scenarios suggested by Stamford and Azapagic [116] (mercury and Radon are omitted) are used as reactants with pure oxygen as oxidiser, with various hydrocarbon/oxygen sets used as reactants. Initial temperature and pressure are set at 300K and 1.01325bar, respectively. GASEQ provides a wide range of equivalence ratio, an automatic increment of equivalence ratio values from 0.2 to 4, depending on oxygen concentration in the mixture, was set to change the stoichiometric values.

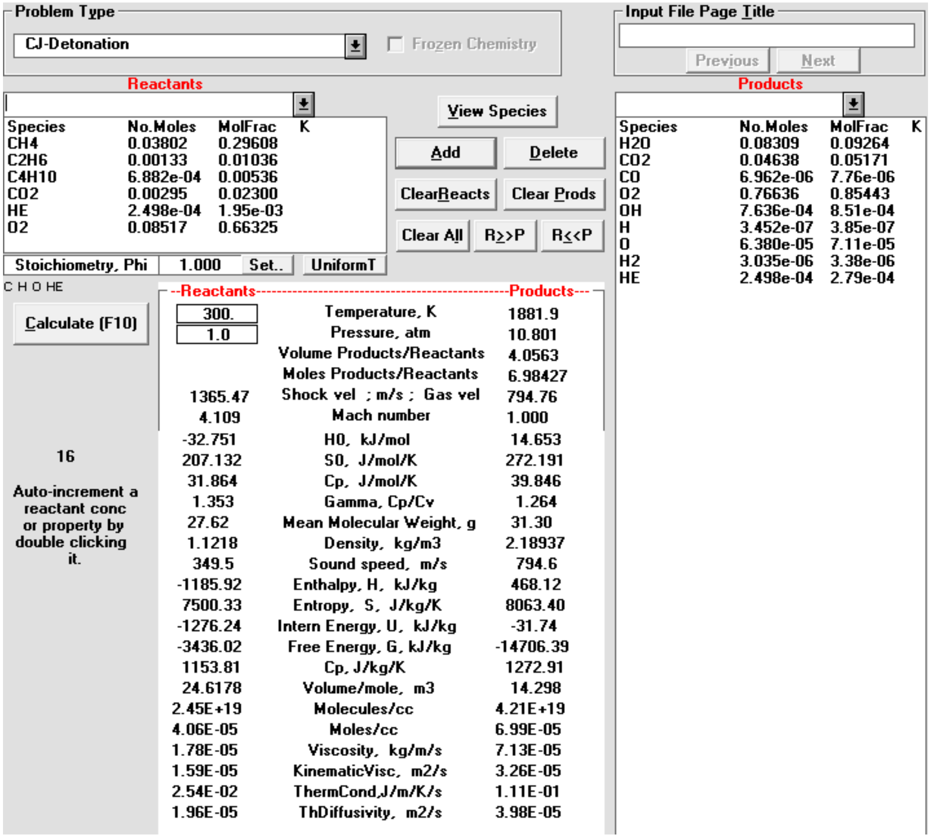

Problem Type: CJ-Detonation

Reactants

Species	No.Moles	MolFrac	K
CH4	0.03802	0.29608	
C2H6	0.00133	0.01036	
C4H10	6.882e-04	0.00536	
CO2	0.00295	0.02300	
HE	2.498e-04	1.95e-03	
O2	0.08517	0.66325	

Stoichiometry, Phi 1.000

C H O HE

Products

Species	No.Moles	MolFrac	K
H2O	0.08309	0.09264	
CO2	0.04638	0.05171	
CO	6.962e-06	7.76e-06	
O2	0.76636	0.85443	
OH	7.636e-04	8.51e-04	
H	3.452e-07	3.85e-07	
O	6.380e-05	7.11e-05	
H2	3.035e-06	3.38e-06	
HE	2.498e-04	2.79e-04	

16

Auto-increment a reactant conc or property by double clicking it.

--Reactants		Products---
300.	Temperature, K	1881.9
1.0	Pressure, atm	10.801
	Volume Products/Reactants	4.0563
	Moles Products/Reactants	6.98427
1365.47	Shock vel ; m/s ; Gas vel	794.76
4.109	Mach number	1.000
-32.751	H0, kJ/mol	14.653
207.132	S0, J/mol/K	272.191
31.864	Cp, J/mol/K	39.846
1.353	Gamma, Cp/Cv	1.264
27.62	Mean Molecular Weight, g	31.30
1.1218	Density, kg/m3	2.18937
349.5	Sound speed, m/s	794.6
-1185.92	Enthalpy, H, kJ/kg	468.12
7500.33	Entropy, S, J/kg/K	8063.40
-1276.24	Intern Energy, U, kJ/kg	-31.74
-3436.02	Free Energy, G, kJ/kg	-14706.39
1153.81	Cp, J/kg/K	1272.91
24.6178	Volume/mole, m3	14.298
2.45E+19	Molecules/cc	4.21E+19
4.06E-05	Moles/cc	6.99E-05
1.78E-05	Viscosity, kg/m/s	7.13E-05
1.59E-05	KinematicVisc, m2/s	3.26E-05
2.54E-02	ThermCond,J/m/K/s	1.11E-01
1.96E-05	ThDiffusivity, m2/s	3.98E-05

Figure 4.1 Screen shot of GASEQ calculations for the Best-case gas composition.

The mass/mole fraction (for reactants and products) and thermodynamic parameters are calculated using the two-dimensional secant method to solve the basic energy and momentum equations

$$\mathbf{p_1 - p_2 + \rho_1 u_1^2 - \rho_2 u_2^2 = 0} \qquad \textbf{Equation 4.1}$$

$$\mathbf{h_1 - h_2 + \frac{1}{2}(u_1^2 - u_2^2) = 0} \qquad \textbf{Equation 4.2}$$

where p is pressure, ρ is density, u is velocity and h is enthalpy. The subscribes 1 and 2 refer to the states before and after the detonation wave, respectively.

The velocity of gases downstream of the detonation wave is assumed to be the speed of sound in the burnt gases, the upstream velocity is calculated from the continuity equation

$$\boldsymbol{\rho_1 u_1 = \rho_2 u_2} \qquad \textbf{Equation 4.3}$$

To start the iterative secant method, the initial value of pressure ratio for C-J detonation is estimated to be $(p_2/p_1)_0 = 15$, which is found to be satisfactory for a number of chemical systems by Gordon and McBride [144]. According to them, the estimation of temperature ratio has higher importance than pressure ratio, hence the temperature of the flame (T_2) is calculated corresponding to the enthalpy [144]

$$\mathbf{h_2 = h_1 + \frac{3}{4}\frac{RT_1}{M_{w1}}\left(\frac{p_2}{p_1}\right)_0} \qquad \textbf{Equation 4.4}$$

where M_{w1} is molecular weight.

In order to compare the validity of the CFD calculations with the numerical results from GASEQ and CHEMKIN-Pro, hydrogen/air mixtures are used to calculate thermodynamic parameters. Also, the mole/mass fraction for the three shale gas compositions with oxygen and for the hydrogen/air mixture calculated by GASEQ are used as input for CHEMKIN-Pro. The results obtained by GASEQ software for different equivalence ratios are compared to those obtained by CHEMKIN-Pro software and discussed later.

4.2.2 GASEQ Setup and Method

As illustrated in figure 4.1, the GASEQ software interface on windows requires three main inlets. At the upper left corner, the problem type must be specified. Nine different processes are provided, the latter process is CJ-Detonation. The reactants must be provided next step. Finally, to enter the reactants quantity, the desired amount needs to be added in mole or in mass unit. The units can be changed from the Unit tab at the toolbar. The most familiar reactions i.e. methane, hydrogen, propane and isooctane with air mixture are provided as templates.

The standard sets of products can be entered manually to provide chemical balance. Hydrocarbons and hydrogen air products with some combustion features are provided. Reactants initial pressure and temperature can be changed from Reactants/Products output properties. The total equivalence ratio is calculated by the software and shown in the box between the Reactants box and output box.

An automatic increment for the case study can be set up by changing the equivalence ratio, after selecting the reactant to be varied, between two definite values by adding or multiplying the initial value with a certain number. The output properties are chosen by clicking them and can be printed on excel spreadsheet. It is possible to get the mole/mass fraction of reactants and products in the excel sheet, which is an important factor in CHEMKIN-Pro software.

4.3 CHEMKIN-Pro

Unlike chemical thermodynamics (GASEQ), chemical kinetics modelling has the ability to provide full information related to the rates of the chemical processes. The mechanisms and rates of the chemical reactions and the factors that affect it are the main subject that chemical kinetics study. CHEMKIN-Pro is one of the most popular software to simulate chemical reaction and analyse chemical kinetics. It was originally designed by Sandia National Laboratory, then it was maintained and enhanced by Reaction Design Inc., which has recently become part of ANSYS [145].

4.3.1 Reaction Mechanism

Wide range of thermodynamic properties and mechanisms can be calculated accurately and fast using CHEMKIN-Pro software. CHEMKIN-Pro uses an extensive library that contains various reaction mechanisms and thermodynamic information that depends on the Reaction Design’s Model Fuel Library, the most complete and thoroughly library assembled by the Model Fuel Consortium [146].

The Gas Research Institute mechanism, GRI-Mech 3.0, was designed to model natural gas and methane combustion. Although this mechanism is considered as one of the most popular single carbon reaction mechanism, it also includes other fuel combustion mechanism such as the detailed combustion reaction mechanism for hydrogen [147]. The detailed GRI-Mech 3.0 mechanism consists of 325 reaction steps and 53 species with associated rate coefficient expressions and thermochemical parameters.

4.3.2 CHEMKIN-Pro Description

For the recent work, an incident shock wave model was employed in CHEMKIN-Pro with GRI-Mech 3.0 for predicting pressure and temperature after the shock. The initial mixture conditions with the composition of mole fraction and the incident shock velocity are required. The mole fractions calculated by GASEQ for the three cases of shale gas compositions and hydrogen/air mixture were used here. The initial pressure and temperature were 300K and 1.01325bar, respectively.

In order to estimate the shock velocity, the equilibrium reactor model with Chapman-Jouguet detonation option has been used with all mixtures above. Since both GASEQ and CHEMKIN-Pro software use Gordon and McBride NASA computer programme [148] in their calculation of chemical equilibrium compositions, the product parameters have been found to be similar from both codes.

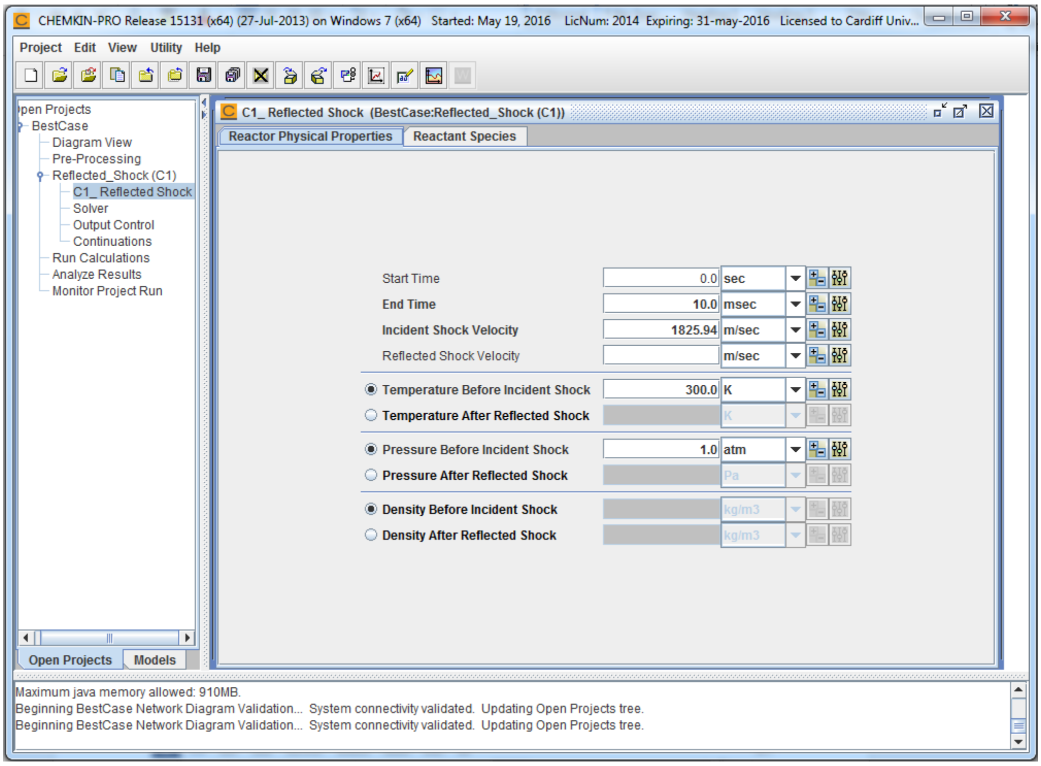

Start Time 0.0 sec
End Time 10.0 msec
Incident Shock Velocity 1825.94 m/sec
Reflected Shock Velocity m/sec
● Temperature Before Incident Shock 300.0 K
○ Temperature After Reflected Shock K
● Pressure Before Incident Shock 1.0 atm
○ Pressure After Reflected Shock Pa
● Density Before Incident Shock kg/m3
○ Density After Reflected Shock kg/m3

```
Maximum java memory allowed: 910MB.
Beginning BestCase Network Diagram Validation...  System connectivity validated.  Updating Open Projects tree.
Beginning BestCase Network Diagram Validation...  System connectivity validated.  Updating Open Projects tree.
```

Figure 4.2 Screen shot of CHEMKIN-Pro.

CHEMKIN utilises the Rankine-Hugoniot relations in a one-dimensional flow across the incident shock assuming that the enthalpy is a function of temperature alone, finding an expression for pressure and temperature ratio across the shock as,

$$\frac{p_2}{p_1} = \frac{1}{2}\left[\left(1 + \frac{\rho_1 u_1^2}{p_1}\right) + \sqrt{\left(1 + \frac{\rho_1 u_1^2}{p_1}\right)^2 - \frac{4\rho_1 u_1^2}{p_1}\frac{T_2}{T_1}}\right]$$ **Equation 4.5**

To determine the temperature ratio that satisfies the above equation, a subroutine within CHEMKIN called ZEROIN [149] is used. The initial value of temperature ratio to start the iteration is calculated using equation 4.6, where the mixture is assumed to be as an ideal gas with constant heat ratio γ (specific heats are independent on temperature),

$$\frac{T_2}{T_1} = \frac{\left(\gamma M_1^2 - \frac{\gamma-1}{2}\right)\left(\frac{\gamma-1}{2} M_1^2 + 1\right)}{\left(\frac{\gamma+1}{2}\right)^2 M_1^2}$$ **Equation 4.6**

where M_1 is the Mach number of the shock, and is calculated using a shock velocity provided.

4.3.3 CHEMKIN-Pro Setup and Method

Setting up CHEMKIN-Pro needs more details than GASEQ. Some factors used in CHEMKIN are extracted from GASEQ. The main interface window of the software contains different reactors laid out on the workspace. The shock reactors do not need an inlet and outlet flow stream and connections. The next step is to pre-process the chemistry set, this step is required before any further input.

The reaction mechanism and rate coefficient file in CHEMKIN format (grimech30.inp) was utilised for the Gas Face Reaction File. The associated thermochemical file (thermo30.dat) was used for Thermodynamics Data File. After running the Pre-Processor, the Gas-Phase Kinetics Output can be checked from to ensure correct launch of the mechanism.

A transient Solver is chosen as problem type from Reactor Physical Properties. Start and End time must be identified with the expected shock velocity and before shock temperature and pressure. The reactant species in mole or mass fraction is introduced in the subsequent step. The mass fraction of reactants used in CHEMKIN software was obtained from GASEQ software. The mixture equivalence ratio (Φ) is used to describe the stoichiometry. As the properties of products have been calculated over a wide range of equivalence ratios (0.2 – 4.0), the Parameter Study Facility in CHEMKIN was the best choice to use. However, using more than one hydrocarbons fuel in different concentrations as reactants generated errors in execution, which led to introduce the fractions of reactant species for every equivalence ratio manually.

The shock velocity can be calculated using the pressure of the shock predicted by Gordon and McBride NASA computer programme [148] with either GASEQ or CHEMKIN software. The pressure ratio relationship across the shock states:

$$\mathbf{u_s = c_s\sqrt{\frac{\gamma+1}{2\gamma}\left(\frac{p_2}{p_1}-1\right)+1}} \qquad \textbf{Equation 4.7}$$

The velocity obtained in CHEMKIN was used to calculate the velocity induced by the shock using equation 4.8

$$\boldsymbol{u} = \mathbf{\frac{2c_s}{\gamma+1}\left(M_s-\frac{1}{M_s}\right)} \qquad \textbf{Equation 4.8}$$

where, u_s is the shock velocity, c_s is the speed of sound in shock conditions, γ is specific heat ratio, p_2 and p_1 are the pressure before and after the shock respectively, u is the induced velocity, and finally M_s is the shock Mach number. All results spreadsheets are then accumulated in one spreadsheet to be discussed and compared with GASEQ results.

4.4 Numerical Results and Discussions

The reactants composition used in GASEQ and CHEMKIN-Pro codes are extracted from the three shale gas senarios proposed by Stamford and Azapagic [116], shown in table 2.3. Oxygen is added to the reactants so that the total equivalence ratio is ranged between 0.2 to 4.0. For both codes, the initial pressure and temperature are assumed to be 101.325bar and 300K respectively. In addition to that, CHEMKIN-Pro requires an estiamted shock velocity, which is calculated using equation 4.7 depending on GASEQ results.

4.4.1 Pressure Gradient

The pressure of products calculated using GASEQ and CHEMKIN-Pro is depicted with respect to the volume ratio of the fuel to the total mixture and shown in figure 4.3. It is found that the pressure behaviour for the three cases is similar and the values correspond well with slightly higher values for those calculated by CHEMKIN. The values of pressure are higher by about 5% at the highest pressure and decrease to less than 3% on the rich and lean sides. The most important cause for this disparity is the higher detailed combustion reaction mechanism used with CHEMKIN. Moreover, the time factor that has been taken into consideration in CHEMKIN-Pro.

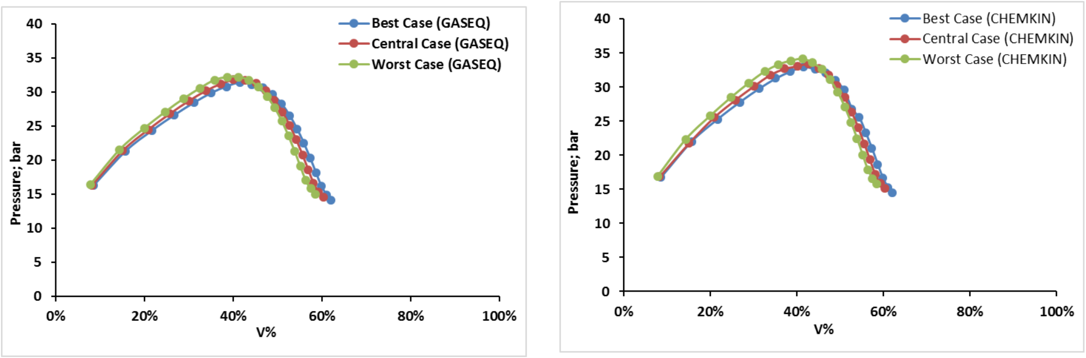

(a) (b)

Figure 4.3 Products pressure versus fuel volume % for hydrocarbon/oxygen mixtures, a. GASEQ, b. CHEMKIN-PRO.

Using pure oxygen as oxidiser made the pressure to peak at a point where the fuel volume reaches about 40% of the total oxy-fuel mixture volume. Also, increasing of hydrogen concentration in product species increases the pressure. The pressure of the products drops more steeply on the rich side than the lean side. The increase of higher hydrogen content hydrocarbons at the expense of methane in the third scenario for shale gas, the worst case, led to attain higher pressure than in the other two cases. However, the presence of nitrogen in the second scenario and the increase in its concentration in the third one led to decreasing the volume percentage of fuel for those scenarios.

Figure 4.4 shows the product pressure for different volume ratios of hydrogen in hydrogen/air mixture. Once more, the CHEMKIN-Pro calculations were higher than GASEQ calculations, but it is now around 1% in the maximum of the reading, which was at a volume percentage of 32%, and less on both sides. Unlike a hydrocarbon/oxygen mixture, the hydrogen/air mixture declined less severity on the higher hydrogen ratio side than the lower one. The more rapid combustion of hydrogen compared to hydrocarbons leads to swift release of heat with less overpressure.

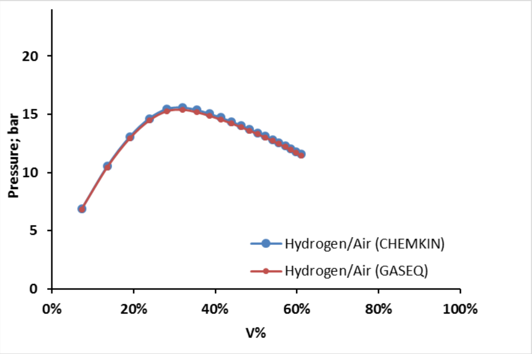

Figure 4.4 Products pressure versus hydrogen volume % for hydrogen/air mixtures.

4.4.2 *Velocity Gradient*

Velocity profiles of products calculated by GASEQ and CHEMKIN-Pro software are shown in figure 4.5. Although the trends of velocity behave in the same manner as pressure in figure 4.3, the maximum values of velocity are more shifted to the rich side of the mixture. The main factor responsible for this shift is products dissociation. This will increase total low molecular mass and density species in the products, as shown in figure 4.6, which leads to increase the velocity until a point where the total molecular mass of these species decreases with the rise of denser species.

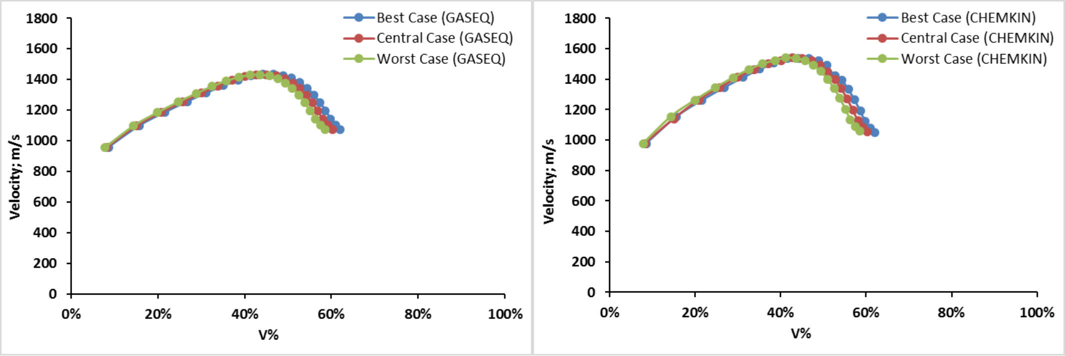

(a) (b)

Figure 4.5 Products velocity versus fuel volume % for hydrocarbon/oxygen mixtures, a. GASEQ, b. CHEMKIN-Pro.

Unlike hydrocarbon, hydrogen/air mixture products velocity persists increasing with hydrogen content increase, figure 4.7. This is mainly related to the continuous decrease in molecular mass of the products with the increase in hydrogen species, figure 4.8. However, the increase of velocity after stoichiometric conditions starts to be less sharp until it remain mainly flat for high hydrogen content detonations.

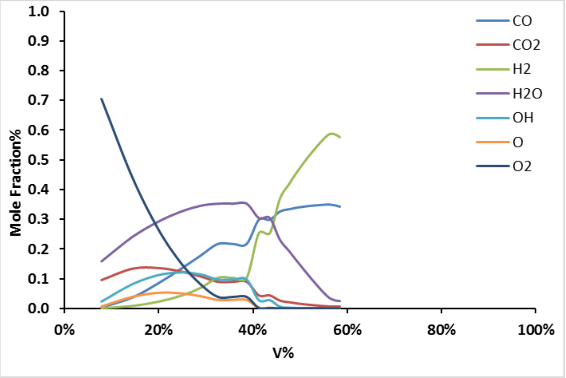

Figure 4.6 The most dominant products species versus fuel volume % for hydrocarbon/oxygen mixtures.

Both GASEQ and CHEMKIN-Pro software calculations correspond well for hydrogen ranged from 19% to 46% of the total mixture. For the ratios out of this range, the product velocity obtained from GASEQ was slightly higher. This was mainly related to the more detailed reaction mechanisms required for these chemical reactions in CHEMKIN-PRO. This, in turn, affects the products heat capacity and the parameters used in equation 4.8 above to calculate induced velocity.

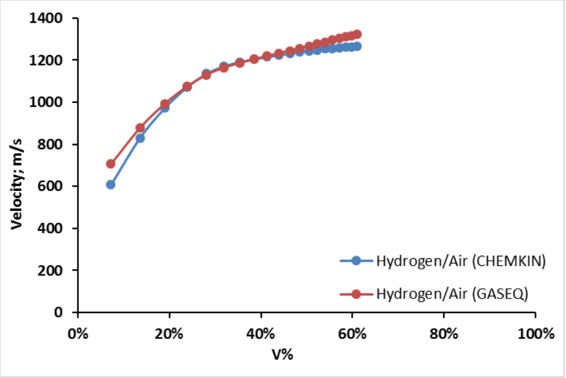

Figure 4.7 Products velocity versus hydrogen volume % for hydrogen/air mixtures.

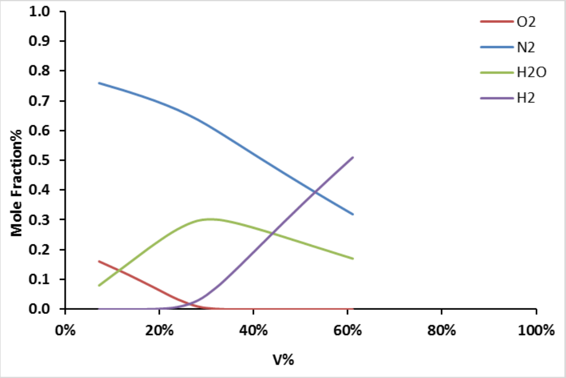

Figure 4.8 The most dominant products species versus hydrogen volume % for hydrogen/air mixtures.

4.4.3 Temperature Gradient

The product gases temperature for different fuel volume fraction for GASEQ and CHEMKIN-Pro software were significantly dissimilar in values. Many factors are responsible for this disparity. Tremendous impact was observed for the more accurate and precise multicomponent formulation and analysis that is utilised with CHEMKIN-Pro rather than the average method which calculates the final equilibrium conditions that is used with GASEQ.

Another factor is initiation of radicals associated to the more detailed GRI-Mech 3.0 mechanism utilised in CHEMKIN-Pro, which consists of 325 reactions and 53 species, mentioned previously. These radicals and some of the combustion products will dissociate back into reactants, or even higher reactive species, at high temperature flames. This dissociation is an endothermic reaction and will be accompanied by energy absorption which will noticeably decrease the temperature in the products.

Figure 4.9 shows the products temperature of detonation as a function of hydrocarbon percentage in the hydrocarbon/oxygen mixture for the three scenarios of shale gas for GASEQ (a) and CHEMKIN-Pro (b). It was found that the temperature of products calculated using GASEQ was about 65% higher than those calculated using CHEMKIN-Pro. However, this difference declines as the fuel volume ratio goes over 50%. The maximum temperature for both software was achieved slightly above stoichiometry. Therefore, the behaviour of the trends for both software was highly matched on the lean side of the curve, while disparity increase with the increases of fuel volume percentage on the rich side.

The temperature of hydrogen/air mixture products for GASEQ and CHEMKIN-Pro showed to be more equiponderance. GASEQ results were 2.9 times the results calculated by CHEMKIN-Pro at the maximum temperature, which was at fuel volume fraction of 32%, and decrease until GASEQ results reaches 2.5 of CHEMKIN-Pro results on both sides of the curve.

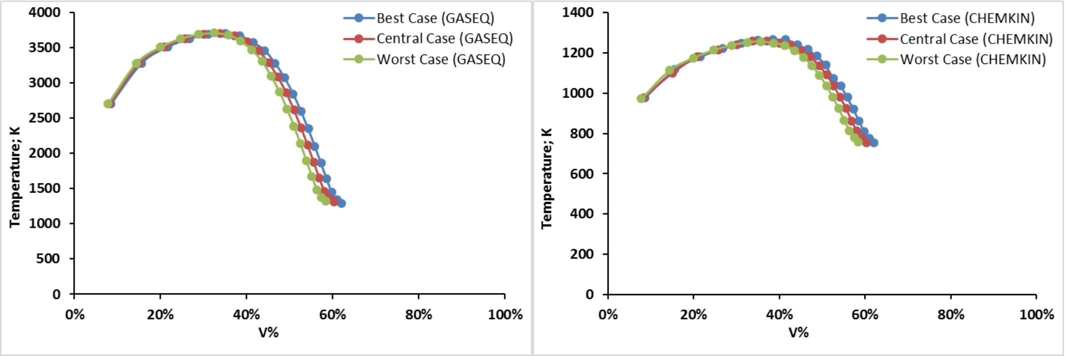

(a) (b)

Figure 4.9 Products temperature versus fuel volume % for hydrocarbon/oxygen mixtures, a. GASEQ, b. CHEMKIN-PRO.

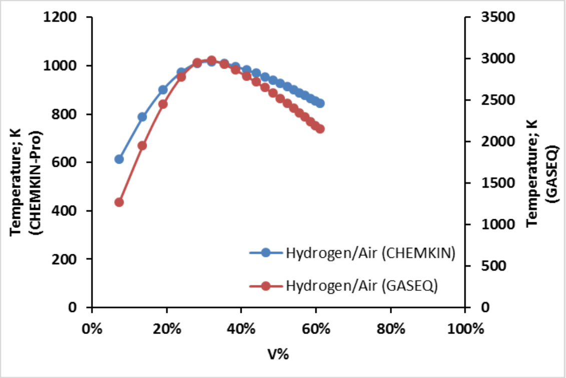

Figure 4.10 Products temperature versus hydrogen volume % for hydrogen/air mixtures.

4.4.4 Detonation Velocity

The Chapman-Jouguet detonation velocity is achieved when the products velocity reaches the speed of sound in the burned gases conditions for a given temperature and pressure. The detonation velocity for common stoichiometric hydrocarbon/air mixtures is above 1800m/s, and it goes above 2300m/s for the hydrocarbon/oxygen mixtures [93][150]. Typical detonation velocity and pressure rise across the detonation wave for common hydrocarbons with air and oxygen are tabulated in table 2.1.

Calculations of the detonation velocity for hydrocarbon/oxygen mixtures in the present work were done using GASEQ software. The results are depicted in figure 4.11 below. The three scenarios of shale gases showed very high-match in detonation velocity for the whole fuel concentration ratios. The maximum detonation velocity was 2558m/s for the best scenario case, this value was shifted to the rich side and achieved at fuel concentration of 47%. This was mainly because of the products dissociation, especially when pure oxygen is used as oxidiser.

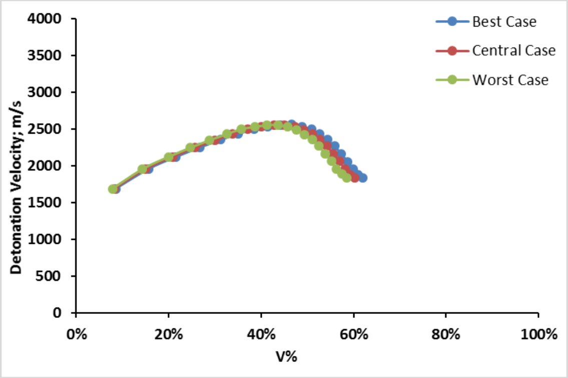

Figure 4.11 Detonation velocity versus fuel volume % for hydrocarbon/oxygen mixtures.

The hydrogen/air and hydrogen/oxygen mixtures detonation velocity are shown in figure 4.12. Results show that hydrogen mixtures have much broader detonation velocity than hydrocarbons. Although hydrogen/oxygen mixture seems to increase more dramatically with fuel volume fraction, the detonation velocity is less compact at high concentrations. Figure 4.13 illustrates the products composition of hydrogen/oxygen mixtures. The decrease in oxygen concentration in the reactants led to decrease of the energy content in the products species, accompanied by the dissociation of products and the decrease of molecular mass caused by the increase of hydrogen in the products, led to a detonation speed increase.

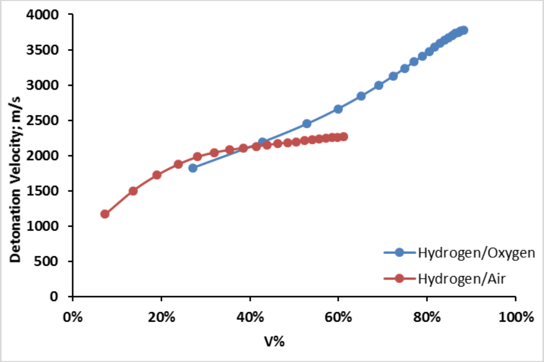

Figure 4.12 Detonation velocity versus hydrogen volume % for hydrogen/air mixtures.

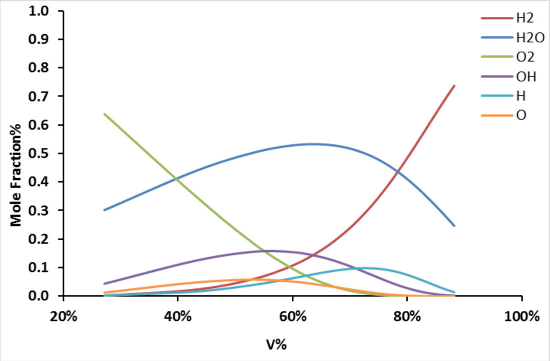

Figure 4.13 Products species versus hydrogen volume % for hydrogen/oxygen mixtures.

4.5 Conclusions

GASEQ and CHEMKIN-Pro have been used to calculate the thermodynamics properties for products of detonation. The product pressure and gas velocity results agree well for GASEQ and CHEMKIN-Pro for a broad range of total equivalence ratios.

The pressure peaks at 41% of fuel volume to the total mixture volume, which is equivalent to 1.6 of total equivalence ratio. Two factors are responsible for deviating the equivalence ratio from stoichiometry. The first one is due to the use of pure oxygen as an oxidiser, the second is the increase of hydrogen content in product species. Less chemically reactive products produced by fuel rich mixtures combustion burns cooler than stoichiometric mixtures, which is considered a major advantage in the current particular application.

Even though pressure produced by detonating hydrocarbons are higher than pressure produced by detonating hydrogen, using pure oxygen with hydrocarbons increases the product pressure by about 50% at the maximum products pressure. The products velocity increases by about 30% at its maximum. The detonation velocity of combusting shale gas blends with air reaches its maximum at total equivalence ratio of 1.2. However, referring to table 2.1, this velocity does not reach the detonation velocity threshold. On the other hand, detonation velocity of shale gas/oxygen blends exceeded threshold with wide range of total equivalence ratio, from 1.2 to 2.6. Figure 4.14 shows the detonation velocity versus total equivalence ratio.

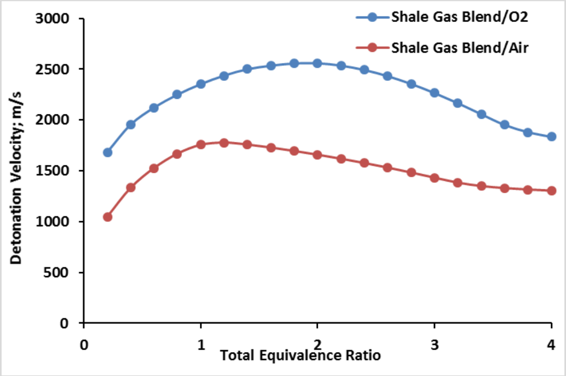

Figure 4.14 Detonation velocity versus total equivalence ratio for shale gas blend.

Numerical results clearly demonstrated the possibility of detonating all the three shale gas scenarios as long as pure oxygen is used as oxidiser. Also, it was shown that the worst case, regarding the amount of methane, of shale gas composition was the best case of produced pressure, which is the main objective to be used in fracturing the shale formation.

4.6 Summary

Numerical results using GASEQ and CHEMKIN-Pro codes have been presented in this chapter. Three shale gas scenarios proposed by Stamford and Azapagic [116] are used with pure oxygen to achieve the highest pressure in the detonation process, to be used in shale formation fracturing. Also, hydrogen/air blend has been used for the purposes of comparison.

Both codes showed good agreement between each other and with results obtained from literature. The detonation velocity threshold for hydrocarbon/oxygen blend has been reached over fuel volume ratios ranging between 30% to 50%. The maximum pressure and velocity were achieved with a fuel volume fraction that exceeds 40% of the total hydrocarbon/oxygen mixture.

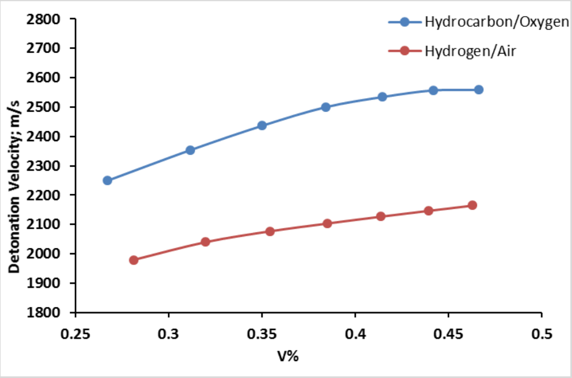

Figure 4.15 Detonation velocity versus fuel volume % for hydrocarbon/oxygen and hydrogen/air mixtures.

Figure 4.14 shows a comparison between detonation velocity for hydrocarbon/oxygen and hydrogen/air blends for volume percentage of fuel to total mixture ranging between 27% to 47%. Although the detonation velocity of shale gas/oxygen mixture composition was higher by about 16% than the hydrogen/air mixture detonation velocity, it was found that they are both behave in the same manner over this range.

CHAPTER FIVE

2-D

Numerical

Design

5.1 Introduction

This chapter presents the results of two-dimensional CFD simulations of the deflagration to detonation transition at stoichiometric conditions for hydrogen/air mixture in the proposed detonation tube. The code used in this simulation was developed originally by Ettner [87] using OpenFOAM. The high-level and advanced programming language of the code is based on a finite volume approach. Many internal geometries, obstacles, shapes, etc., have been examined. Obstacle presence increases flame speed, which in turn generates intense turbulence. This leads to a reduction of the transition distance.

The most effective obstacles are reviewed here. This has been identified depending on the lowest transition distance and higher pressure produced by the detonation tube. The temperature has been taken into account as it was required to keep the pipe wall temperature as low as possible to avoid oxygen autoignition.

5.2 OpenFOAM

The Open Field Operation And Manipulation (OpenFOAM) software is an open source Computational Fluid Dynamics (CFD) toolbox. It is based on the finite volume method. The finite volume is a numerical method where the investigated physical domain is meshed and divided into a control volume at the centre of every node in such manner that the governing partial differential equations are discretised to algebraic equations. The algebraic equations then are solved for every cell, integrated over them and approximated for the entire domain.

A C++ library is used in OpenFOAM to create executable files in the form of application files utilised to develop and solve a system of partial differential equations with suitable initial and boundary conditions. The OpenFOAM environment, such as other CFD codes, is structured in three parts, as indicated in figure 5.1.

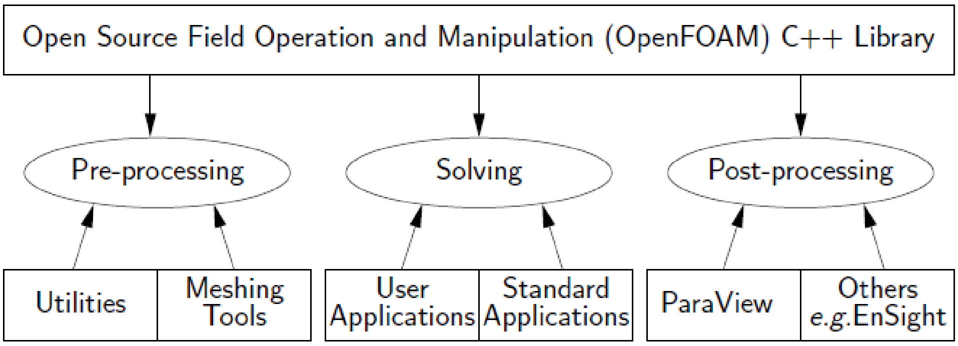

Figure 5.1 OpenFOAM structure [151].

In the Pre-processing, the geometry of the domain is defined with the aid of a grid generation application. The solver is where the system equations are solved for the given grid. The final step is Post-processing, where the results are analysed and visualised.

5.2.1 *Modelling*

Deflagration to detonation transition modelling requires a wide range of combustion aspects to be studied. Laminar flames, turbulent flames, the acceleration and transition phenomenon, in addition to the detonation waves that must be taken into account when dealing with DDT simulation. Deflagration requires very low energy to be initiated [64], for that it is more likely to occur than detonation. However, deflagration is intrinsically unstable which will give the flame front a wrinkled shape increasing the flame surface area and its velocity as a result. In a confined geometry, the wall effects and interactions of the acoustic waves with the flame front generate turbulent flames. Further propagation can develop into detonation.

In the OpenFOAM code used in the present work [87], the conservation of mass, momentum and energy equations together with the equation of state for ideal gas have been used for a compressible flow. A system of differential equations, included the mass fraction for all species, resulted from the above step to calculate the flow parameters during the chemical reaction. According to Godunov's scheme, each contacting cell was considered to be a Riemann problem. Godunov's scheme [152] is a conservative method used to calculate the convective flow on the cell surface without using a time expensive iterative scheme.

The Riemann problem is an initial value problem. It is numerically very expensive to have the exact solution for it. Therefore, various methods have been established to calculate an approximate solution. One of the most popular methods is the Harten-Lax-van Leer-Contact (HLLC). HLLC works on direct calculation of numerical fluxes, for that it is considered as a time efficient Riemann problem solver. For more details see [87].

5.2.2 Solution Methods

The turbulent flow equations employed in the current simulation have been solved using the Unsteady Reynolds Averaging Navier-Stokes (URANS) method. The URANS method is developed from RANS method. The main difference between RANS and URANS methods is the additional unsteady term that is presented in the momentum equation in URANS [153]. It depends on predicting the effects of turbulence on the mean flow field, yet it has had successful models of unsteady separated model [154].

Turbulent fluctuations are separated clearly from stationary main flow in RANS calculations, while in URANS both turbulent fluctuations and mean magnitude are considered as transient and subjected to temporal changes. The Reynolds averaged equations are solved in three-dimensions with time dependence [155]. Large Eddy Simulation (LES) quite differs from URANS regarding the mesh and time step requirements [72]. While LES targets the eddies of the turbulence itself, URANS models the turbulence and resolves only unsteady mean flow structures. For that, LES requires higher spatial and temporal resolution, and is more costly [156].

In CFD, there are two main approaches developed to calculate the flow parameters, the pressure-based approach and the density-based approach. Originally, the pressure-based approach was developed to deal with incompressible and low-speed compressible flows, while the density-based approach, on the other hand, was developed for high-speed compressible flows. Nevertheless, both approaches are nowadays enhanced to be used on a wider range of flow conditions. The momentum equation is used in both approaches to obtain the velocity. The continuity equation is used to obtain density and the equation of state to obtain pressure in the density-based approach. Continuity and momentum equations are manipulated to obtain the pressure field in the pressure-based approach. The density-based original formulation for high-speed compressible flows offers the advantage of better shock capturing resolution with greater accuracy in terms of results, which in turn gives preference over the pressure-based approach for such cases [157].

The code used was originally designed to calculate the flow parameters and flow properties for the combustible mixture of stoichiometric hydrogen/air. This was suitable for this research as in the 2-D simulation document. The initial conditions are stagnant at atmospheric pressure and temperature. The compressible flow at low speeds can be considered an incompressible flow, with incompressibility meaning that density is independent of pressure. For that, the density-based solver cannot be used at the beginning of the solution where the flow is considered to be totally stagnant. Therefore, an additional solver is provided to start the solution. This solver was developed using the pressure-based approach to overcome the low Mach numbers at the beginning of the solution. When the velocity reaches a certain value, the density-based approach solution would start using the outputs of the pressure-based approach as initial values.

5.3 OpenFOAM Setup

As seen in figure 5.1, OpenFOAM is a C++ library. This library is structured in three parts, Pre-processing, Solving and Post-processing. The Pre-processing is where the geometry is defined to generate a computational mesh, the convenient boundary conditions are specified and necessary properties defined. The next step is where the governing differential equations are discretised and then iterated through the domain to get the final solution. Finally, using a post-processing step, the results can be visualised and analysed.

5.3.1 Pre-Processing Stage

5.3.1.1 Geometry and Mesh Generation

OpenFOAM is designed to work with a 3-dimensional Cartesian coordinate system, for that all geometries are generated in 3-dimensions. The 2-dimensional computations are made by creating a 3-dimensional mesh and set the third dimension, where no solution is required, as a one cell thickness.

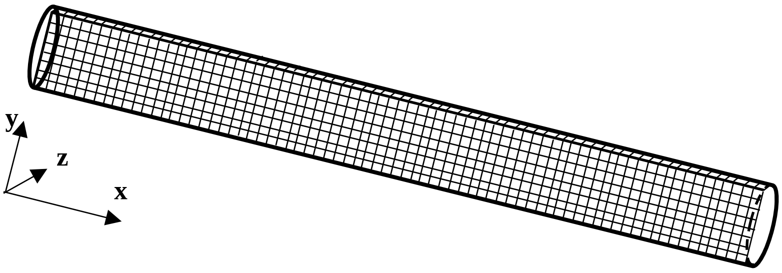

Figure 5.2 Mesh grid.

Many utilities are used to generate a mesh in OpenFOAM, like blockMesh and snappyHexMesh, which are the most popular utilities. However, the mesh can be generated using other software (ANSYS, Fluent, Gambit, etc.) and converted into a format that OpenFOAM uses. A 2-dimensional geometry with 21.2mm height and 1500mm length was used to simulate the experimental tube by using the blockMesh utility, figure 5.2. This utility has all the basic elements needed to create any kind of mesh.

At the outlet, the mesh is specified with a uniform parallelogram, segmented into hexahedral cells. The number of cells in x and y-direction depends on the mesh refining, while it is unity in the z direction. The blockMesh dictionary file contains eight vertices, a 3-dimensional point in space, forming a block with six patches called boundaries. Four of those patches, normal to x and y directions are dealt as walls, while the other two, normal to z direction, are considered as an empty front and back. That means there is no flow moving in the z direction.

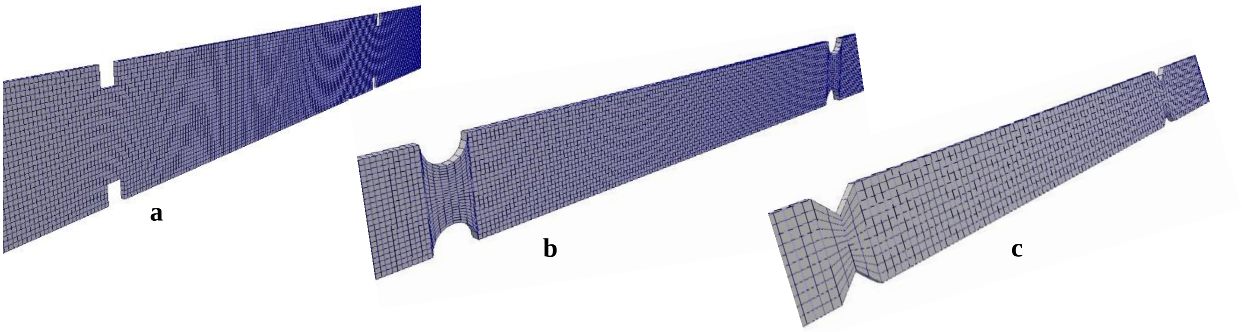

Figure 5.3 obstacles shapes.

The next step was to add obstacles to the internal geometry along the x direction. Three types of obstacles (rectangular, semi-circular and triangular cross-sections) were used to increase the flame turbulence, which will decrease the transition to detonation distance. The rectangular obstacles, figure 5.3a, were specified by using the topoSet utility. This utility is used to split the mesh into different regions. The obstacle box has been identified by two points, the lowest and highest points diagonally, and the mesh has been eliminated in a way the programme deals with it as a wall.

Using the topoSet utility to create the semicircular obstacles showed a bumpy surface, which would certainly affect the calculations. A new blockMesh dictionary was written where the domain block was divided into nineteen blocks (ten for the smooth tubes and nine for obstacles in-between). Semicircles are drawn on the upper and lower end of the short blocks to represent the semicircular obstacles along the tube, see figure 5.3b. With triangular obstacles, figure 5.3c, the domain block has been split into three times the obstacle number plus one.

The size of the mesh highly influences the time of computations, finer meshing sizes consumed more time in the solution stage. On the other hand, an accurate numerical solution of the equations robustly depends on the mesh size. However, the blockMesh utility allows the user to control the cell number in the domain in each axis. At the beginning, the domain was discretised into (1500,21,1) cells for (x, y, z) directions, this created 31,500 cells. More accurate and detailed results have been described when the cells duplicated in x and y-direction, to be (3000,42,1) which creates 126,000 cells. Further duplicate, (4500,42,1), led to an intolerable run time, and the results at the beginning of the solution process showed close results to the previous discretisation. Checking the mesh was the next and last step in mesh generation, this step checks the validity of the mesh, geometric and topological quality of the surface and the orthogonal quality and skewness. The average mesh non-orthogonality was zero and the maximum skewness was 4.7728×10^{-6}.

5.3.1.2 Boundary and Initial Conditions

A set of files (points, faces, boundary and other files) is generated describing the geometry and mesh cells. Each boundary is associated with a boundary condition. In our particular case, there are two kinds of boundaries, as described in the previous section above. In the x-z and y-z plans, there are four walls set as zeroGradient, i.e.

the gradient of the respective quantity is zero on this boundary. The two walls in the x-y plane are set as an empty front and back, i.e. no flow through the z direction.

A zero time folder is created to include all the initial conditions. The charge, which is stoichiometric hydrogen/air mixture, is set in the entire domain at atmospheric conditions and at rest. The reaction is started by setting the temperature at the first column of cells at the beginning of the domain higher than the autoignition of the fuel.

5.3.1.3 Properties Dictionaries

The properties dictionary contains thermophysical, chemistry, turbulence, and any other properties related to the simulation. The thermophysical properties define how the thermal, transport and mixture properties are calculated. The chemistry properties dictionary defines the chemical reaction rates, chemical timescale and released energy. In the present work, the reaction mechanism of GRI-Mech 3.0 [147] was used to calculate the coefficients for the above properties.

The turbulence model has been included in the code used here. Any solver that includes turbulence modelling reads the turbulenceProperties dictionary, included in the constant folder. Within that file is the simulationType keyword that controls the type of turbulence modelling to be used. The simulation of the turbulent model was performed using the Reynolds-Average Stress (RAS) model with amended coefficients. The amended RAS turbulence model coefficients are defined in an appended sub-dictionary. Another dictionary was used to define additional properties like turbulent Schmidt number and viscosity.

5.3.2 Solving Stage

As the mixture is at stagnation and atmospheric condition at the beginning of the simulation, it was necessary to develop two approaches to solve the case. Pressure-based approach for the stagnant beginning and density-based approach when the velocity reaches a certain value. The main difference between the two approaches is how the three conservation equations are coupled. Whereas the density-based solution calculates the density field using the mass conservation equation and the pressure field is calculated using the equation of state, the pressure and velocity fields in a pressure-based solution are calculated by manipulating the mass and momentum conservation equations. Although a pressure-based solution is a cost-efficient solution with large time steps, the density-based solution offers a much better resolution to capture the shock in addition to the possibility of faster convergence rates as it is primarily designed for compressible flow.

The simulations for the three internal geometry cases studied in this work were started with a pressure-based solution from time zero until a point when the flame speed reaches the critical deflagration speed. Switching to the density-based solution is possible after this point as the combustion velocity is strong enough. The initial boundary conditions are set at the time when the flow reached the supersonic conditions. This time differs with different obstacle cross-sections.

5.3.3 Post-processing Stage

Although the time steps that have been chosen in the pressure-based solution were longer than those used in the density-based one, the write intervals were the same for both solutions. This would give uniform output files for every time step for the purpose of visualisation and analysis. The open source data visualisation and analysis tool, Paraview, was used to review the results for every time step saving screenshots to show images for influential time steps. Also, a line has been drawn at the centre of the mesh along the x-axis and the data lying on this line have been researched and depicted using excel.

5.4 Simulation Results and Discussions

The 2-dimensional simulation was used to compare between many internal geometries to find the most effective ones that produce higher pressure and require less transition distance. Three main geometries are discussed in here, rectangular, semicircular and triangular. The blockage ratio, which is the ratio of smooth tube area to the least area in the tube, for all of the obstacles is 47%. The domain is divided into ten equal parts along the x-axis, each part is 150mm in length measured from centre of an obstacle to the centre of the next obstacle. Each obstacle was 10mm long.

5.4.1 Combustion Propagation and Flame Speed

The internal geometry of the detonation tube influenced the combustion propagation significantly. The time required to consume the reactants was less for the tube with rectangular and triangular obstacles than for the tube fitted with semicircular obstacles. This has been ascribed to the sharp edges in the cross-section of the first two geometries, which increases drag and its influence on the degree of induced recirculation. Thus, the combustion in the tube equipped with rectangular obstacles consumed the combustible mixture in 7.15ms, while the tube fitted with triangular obstacles consumed the combustible mixture in 7.40ms, and the tube fitted with semicircular obstacles consumed it in 8.40ms.

One feature of the OpenFOAM code used in the present study is determining the combustion progress along the domain. Figure 5.4 shows the combustion location versus time for the flame when it passes every obstacle. However, when the flame is too fast at the last obstacles, the flame passes the obstacle somewhere between two sequential intervals. Although the behaviour of the flame was quite similar for the three configurations until it reaches the first obstacle, the geometry effect was obvious on the arrival time of the flame. The flame arrives the first obstacle at 4.80ms, 4.95ms and 5.15ms for the rectangular, triangular and semicircular obstacles, respectively. The flame entailed 67.1% of the residence time for the tube equipped with rectangular obstacles, while it entailed 66.9% for the triangular and only 61.3% for the semicircular obstacles configuration, figure 5.5. This indicates that waves reflected by the polygonal obstacles interact with the flame and accelerate it leading to faster flame speed. On the other hand, the oscillations in the flame created by the interaction between the flame and the semicircular obstacles were very high, which resulted in low consumption of combustible mixture, or in other words, slower flame speed.

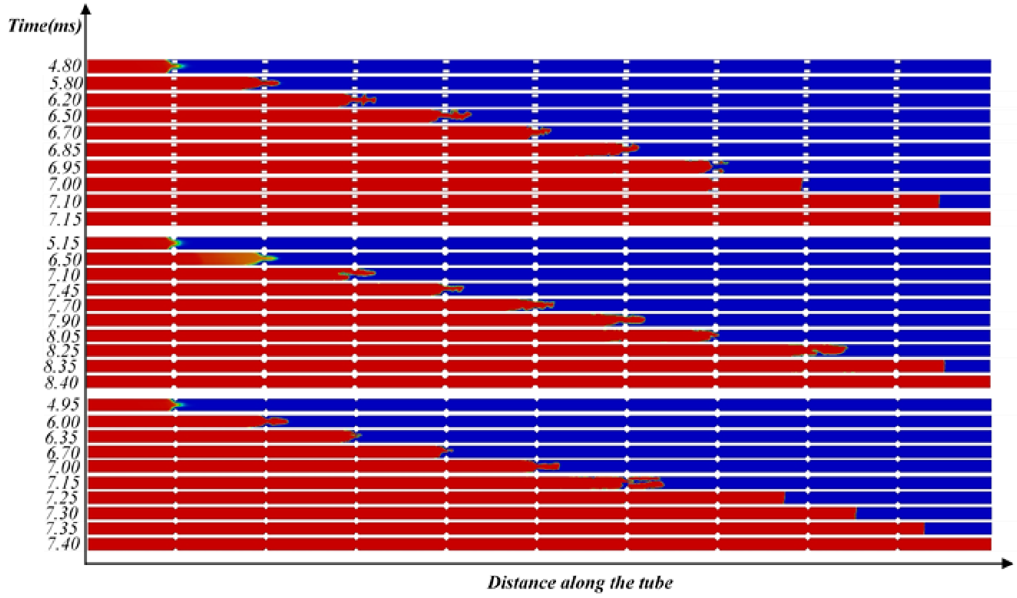

Figure 5.4 Combustion propagation along the tube for the three configurations.

Depending on the combustion progress, the flame tip is located along the x-axis for a line drawn at the centre of the domain. Figure 5.6 shows the flame tip speed for the three configurations, where the squares shown on the x-axis represent the position of the obstacles. Before delving into details, it is worth to emphasise that as the flame speed increases while moving downstream the tube, the flame step increases with time and results in a lack of detail for the flame tip. Nevertheless, the oscillation was more obvious all along the tube due to the moderate acceleration of the flame speed with the semicircular obstacles.

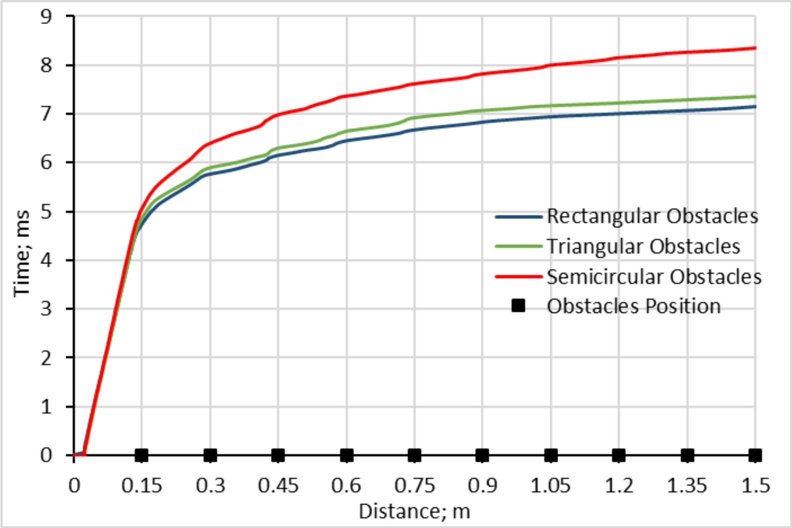

Figure 5.5 The arrival time of flame along the tube.

However, the flame tip speed was found to behave in the same manner for the three configurations from the beginning of the tube, through the first obstacle until it reached the second obstacle. As it is illustrated, the flame tip velocity oscillates during the acceleration process due to the interaction of the fresh mixture with the obstacles in the tube. The magnitude of the oscillations grows as the flame interacts with more obstacles.

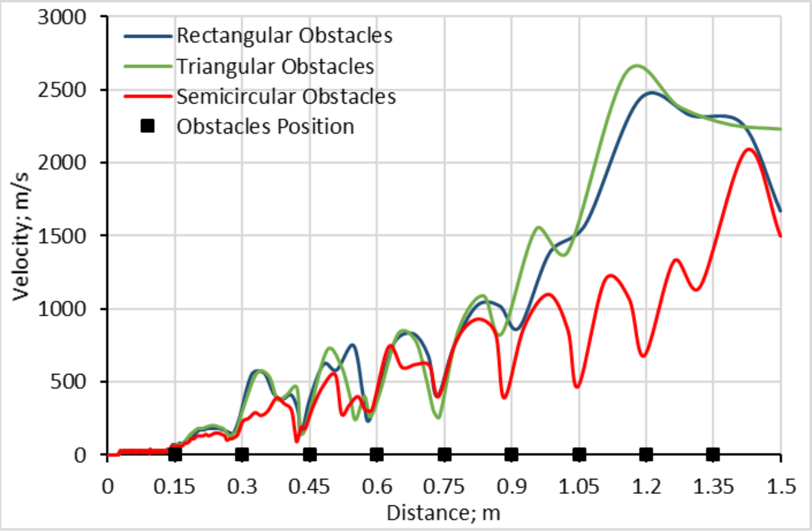

Figure 5.6 Flame tip velocity along the tube.

Generally, the flame decelerates before every obstacle and accelerates while passing through them. The mounting mass flux entering the flame near the obstacle stretches the flame and accelerates it. The flame is deformed in the short distance gap inside the obstacle, leaving an amount of unburned mixture at the windward side of the obstacle. The Rayleigh-Taylor instability and the Kelvin-Helmholtz instability are induced by the turbulence occurred due to the longitudinal deformation of the flame passed the obstacle to the full tube diameter. As the flame front pass the obstacle, it is deviated and folded up towards the leeward side of the obstacle. Meanwhile, the flame at the windward side of the obstacles turns to be almost vertical whilst burning the fresh combustible mixture left there, as illustrated in figure 5.7. The same behaviour for flame propagation interacting with an obstacle was found by Singh et. al. [158] and Fan et. al. [159].

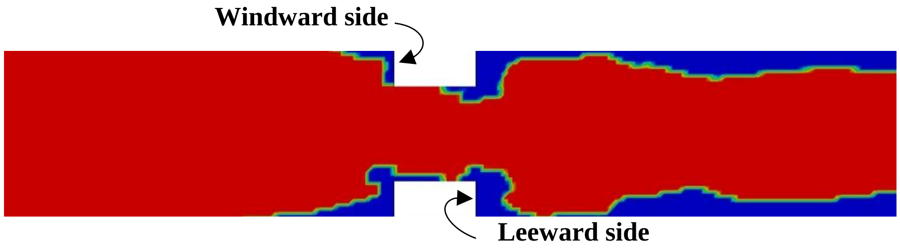

Figure 5.7 Second obstacle at t=5.9ms.

Although the smooth cross-section area changes achieved with triangular and semicircular obstacles promote the flame with a longer accelerating distance resulting in higher flame velocity, it was found to act in a different manner for each geometry. The triangular obstacle was found to achieve higher velocity through the obstacle passage than the semicircular obstacle. This was mainly because of the separation point and its effect on the induced vortex behind the obstacle, in addition to the degree of induced recirculation produced by increasing drag due to sharp edges, as illustrated in figure 5.8.

Both polygonal obstacles behaved in almost identical manner until the flame exceeds the third obstacle. The influence of the sudden expansion of the rectangular obstacle on the flame speed reduction was most obvious after the third obstacle. Yet, both configurations undergo a convergent increase until the flame exceeds the sixth obstacle. The flame with the triangular obstacles then will experience higher peaks and exceeds the detonation threshold at a distance shorter than that for the flame with the rectangular obstacles. The flame decelerates for both configurations, leaving the tube at detonation speed for the triangular obstacles and below that for rectangular obstacles.

The flame speed experienced higher disturbance along the tube. The flame speed decelerates sharply before every obstacle and accelerates through and between the obstacles. This led to gradual growing in the flame speed and longer time to consume the combustible mixture and lower jump when the flame exceeds the detonation speed after the last obstacle.

t=6.10ms

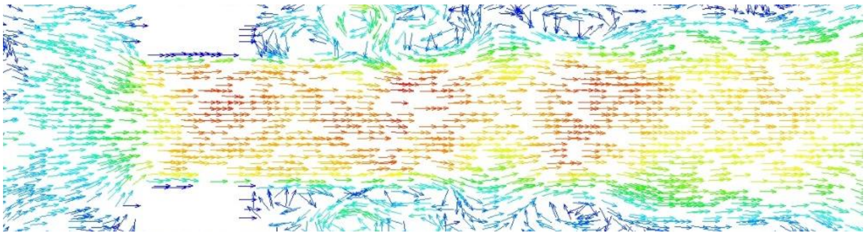

t=6.30ms

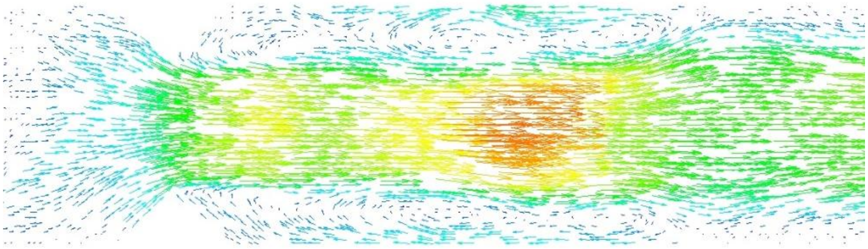

t=7.05ms

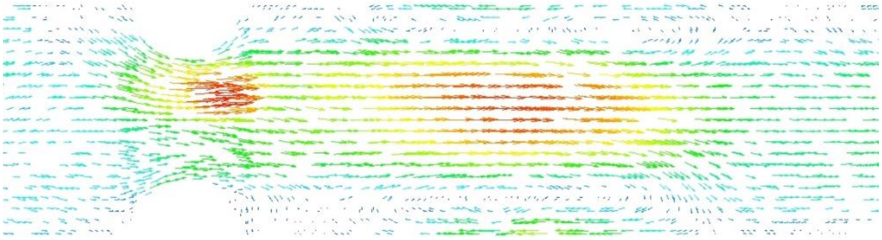

Figure 5.8 Velocity vectors for the three configurations at the third obstacle.

Figure 5.9 shows the flame speed along the tube versus time. The first noticeable oscillation in the flame speed starts when the flame interacts with the first obstacle. As it was mentioned above, the flame in the tube equipped with the rectangular obstacles reaches the first obstacles in 4.80ms, which is the earliest among the three configurations. As it seen in figure 5.9, the flame speed, for both rectangular and triangular obstacles, behaves in quite similar manner. However, the flame accelerates earlier with rectangular obstacles, which made it advanced at each point where the flame speed experiences a peak. The tube equipped with semicircular obstacles took longer time and distance to develop fast flame speed. The shorter recirculation zone, as shown in figure 5.8, in addition to the absence of sharp edges, which decreased the Rayleigh-Taylor the Kelvin-Helmholtz instabilities, prevents the rapid flame speed development.

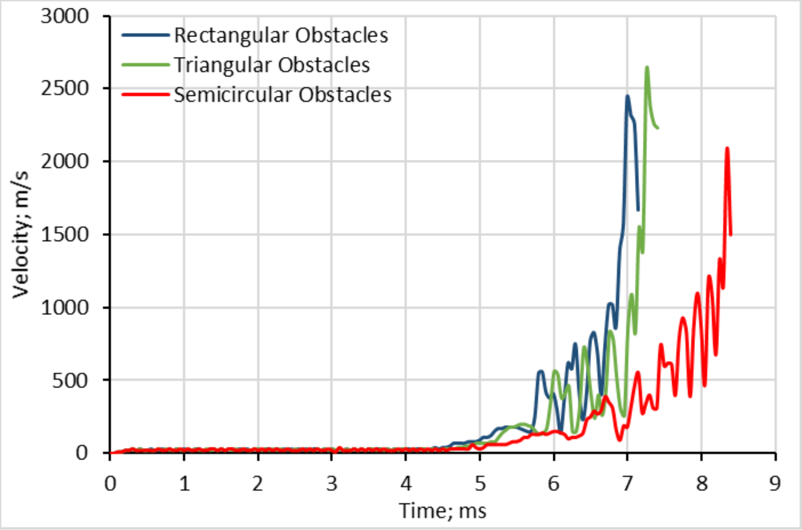

Figure 5.9 Flame tip velocity variation with time along the tube.

5.4.2 Detonation Velocity Threshold

The development of products velocity downstream the flame is considered one of the most dominant factors responsible for spontaneous pressure increase in detonation. The main source of the flame acceleration at the beginning of the combustion, just after ignition, is the flame surface area. Reactants enter the flame with a speed equal to the burning velocity of the mixture. Expansion combined with a reduction in density caused by heating during combustion process accelerates the products, until a certain point when the products hit the speed of sound. That leads the pressure waves to propagate downstream of the combustion zone. The compression heats the reactants in front of the flame and increases the burning velocity and the velocity of the product consequently, which eventually leads to a detonation.

The simulation results, shown in figure 5.6, showed that flame speed exceeded the detonation speed threshold in the tube with rectangular obstacles at t=6.95ms before the flame enters the seventh obstacle. For the triangular obstacles, detonation speed threshold is exceeded at time t=7.15ms where the flame lies between the sixth and the seventh obstacle. Finally, the detonation speed threshold is achieved when the flame passed the eighth obstacle at t=8.25ms for the semicircular obstacles. The flame location when the detonation was achieved for the three configurations with their velocity contours are shown in figure 5.10.

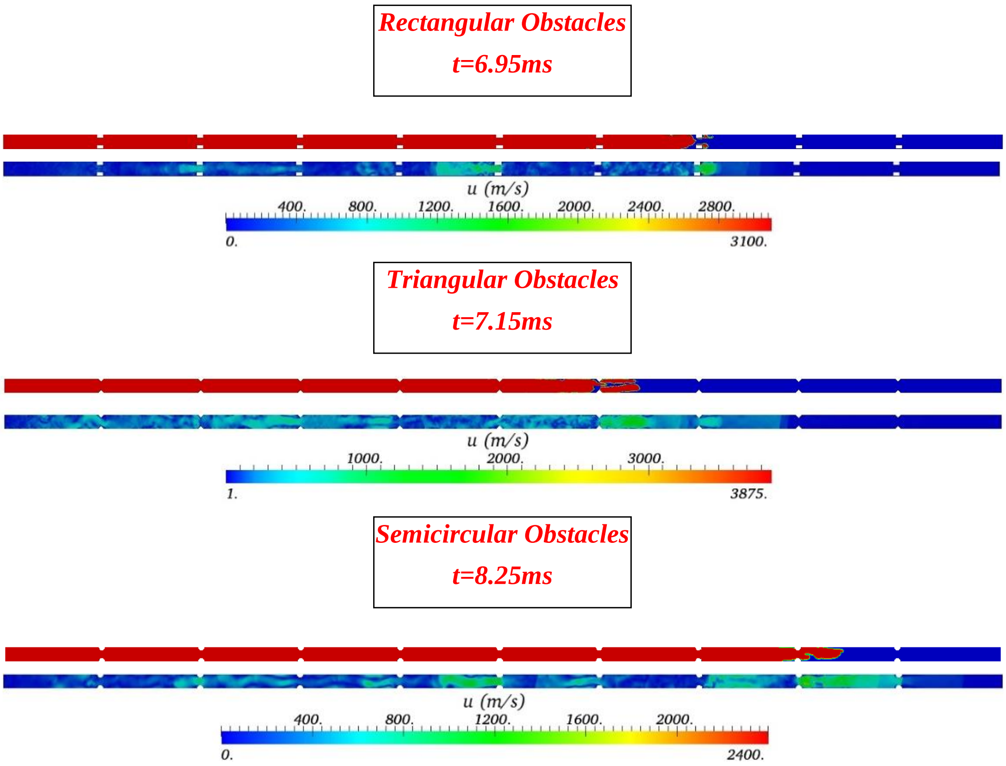

Figure 5.10 Detonation location and time for three internal geometry configurations.

A phenomenon of importance for all geometries is the shock reflection, which has a crucial effect on the pressure and velocity gradient along an obstructed tube. When the shock wave hits the upper surface of an obstacle it reflects, and when it passes the obstacle two more waves are generated: an expansion wave and a diffraction wave, as it illustrated in figure 5.11. While the reflection wave strengthens the incident shock, the expansion wave weakens it. Mach stem (the wave formed by the incident and reflected shock waves fusion) will be generated between the high pressure point of the incident-reflected waves interference and the low pressure point of the incident-expansion waves interference.

The upper side width of the obstacle plays a pivotal role in generating the expansion wave. Wider upper side obstacles produce higher Mach stem and higher incident shock pressures as a result. The windward slope (for triangular cross-section obstacles) also has considerable influence on the incident shock strength. For the positive slope of the triangular obstacle, the reflected wave is generated as soon as the incident shock touches the obstacle edge. Thus, there is a phenomenon of more expansion-contraction as a consequence of this early reflected shock, and therefore the higher incident shock pressure [73].

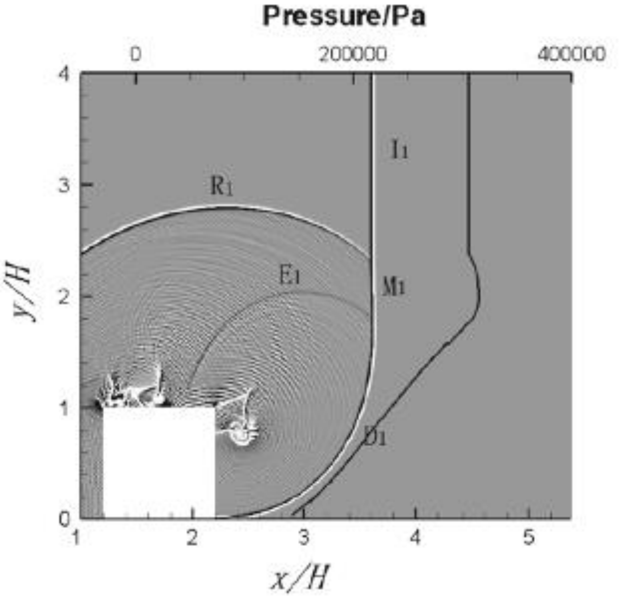

Figure 5.11 Waves generated when an incident shock wave (I) passes an obstacle [73]**.**

5.4.3 Pressure Gradient

Unlike deflagration, detonation waves are compression waves. The pressure ratio across detonation wave reaches up to 15.6 [93]. This ratio is liable to increase significantly under certain circumstances, like retonation. Retonation is a reflected pressure wave. Detonation formation is usually accompanied by strong pressure waves propagate through products. When these pressure waves reflected off the closed end or obstacles, they propagate back towards the main detonation wave. The increased speed of sound in the products helped the retonation wave to overtake the detonation wave. For a very short period, a detonation/retonation combination is formed, leading to a stronger detonation wave.

The flame tip pressure along the tube for the three configurations is shown in figure 5.12. The pressure was almost the same for the three configurations until the flame passed through the second obstacles. By that time, the pressure wave emanated at the beginning of combustion will reflect by the obstacles and the end of the tube and reflect to merge with the flame front. The effect of contraction created by the obstacle is more noticeable at the first six obstacles than the last three. This was because of the better recorded output data according to the writing time interval with respect to the flame speed. The pressure increases as the flame approaches the obstacle and decreases when it goes through it to re-increase in the distance between two sequential obstacles.

The growth gradient in pressure is increasing while the flame is moving downstream. Unlike the two other configurations, where the maximum pressure is achieved at the end of the tube, the tube fitted with rectangular obstacles hits the maximum pressure just before the eighth obstacles, where the detonation has been achieved. The pressure then falls sharply followed by a steep rise when leaving the tube.

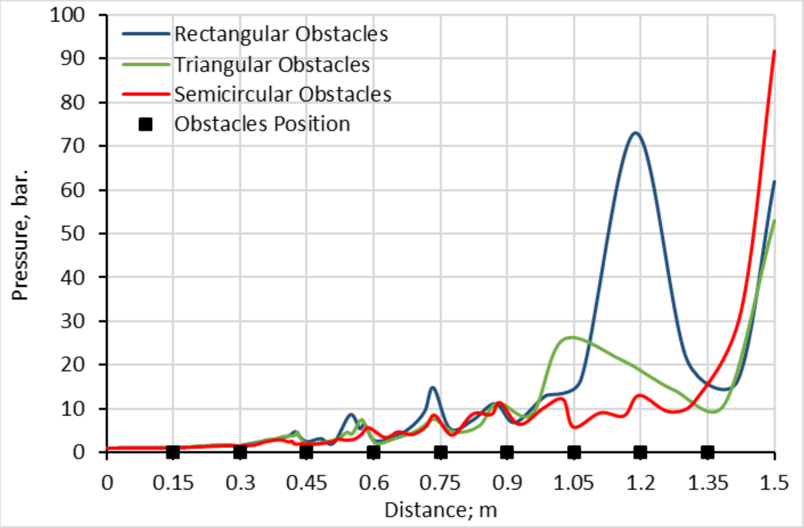

Figure 5.12 Flame tip pressure along the tube.

The first noticeable increase of pressure, for the tube fitted with triangular obstacles, was as the flame moves from the fifth to the sixth obstacle. The pressure then decreases gradually until the flame passes the last obstacles. A sharp increase in pressure is shown while the flame is leaving the tube, where the pressure reaches the maximum value by the exit of the tube.

The tube fitted with semicircular obstacles achieved higher pressure than the two other configurations. The pressure growth increases slightly along the tube with modest leaps before each obstacle followed by a decrease in pressure. While the flame moves toward the last obstacle, the pressure increases until the detonation is achieved where the pressure upsurge to the maximum heading out of the tube.

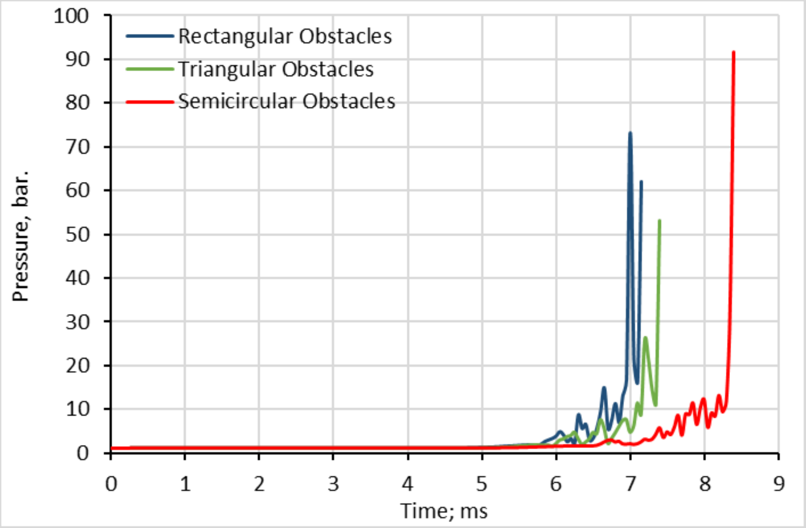

Figure 5.13 Flame tip pressure along the tube versus residence time.

Figure 5.13 shows the flame tip pressure with respect to time. The tube fitted with rectangular obstacles shows the earliest development of pressure as it was the first configuration where the flame reached the first obstacle. In addition, the pressure growth with time was higher with this configuration. The maximum pressure is achieved before the combustion is completed at t=7.00ms, with another pressure jump by the end of combustion, t=7.15ms, at the tube exit plan.

The tube fitted with triangular obstacles was the second in pressure development. The growth was the least among the three configurations until t=7.20ms, when the first jump is stated. The pressure then decreases before it hits the maximum by the end of combustion process at t=7.40ms. The flame tip pressure in the tube equipped with semicircular obstacles was less volatile than the other two configurations until t=8.35ms and the step after, when it encounters an enormous surge to reach the maximum at t=8.40ms. The three maximum pressure contours for each configuration are depicted in figure 5.14.

Figure 5.15 illustrates maximum pressure traces, over the whole combustion time, along the tube with respect to distance for the three configurations. Rectangular obstacles showed more systematic behaviour for pressure. Pressure undergoes steep augmentation at the beginning of the obstacle, then declines sharply by the end of it. It is shown that the maximum pressure along the tube was 73.2bar., and was reached just before the eighth obstacle. Figure 5.16 represents the maximum pressure change versus time for each point along the tube. Pressure range between 1.01325bar and

2.1bar until it reaches the second obstacle at time 5.8ms, then pressure experiences high fluctuations moving from the second obstacle to the end of the tube at time 7.15ms.

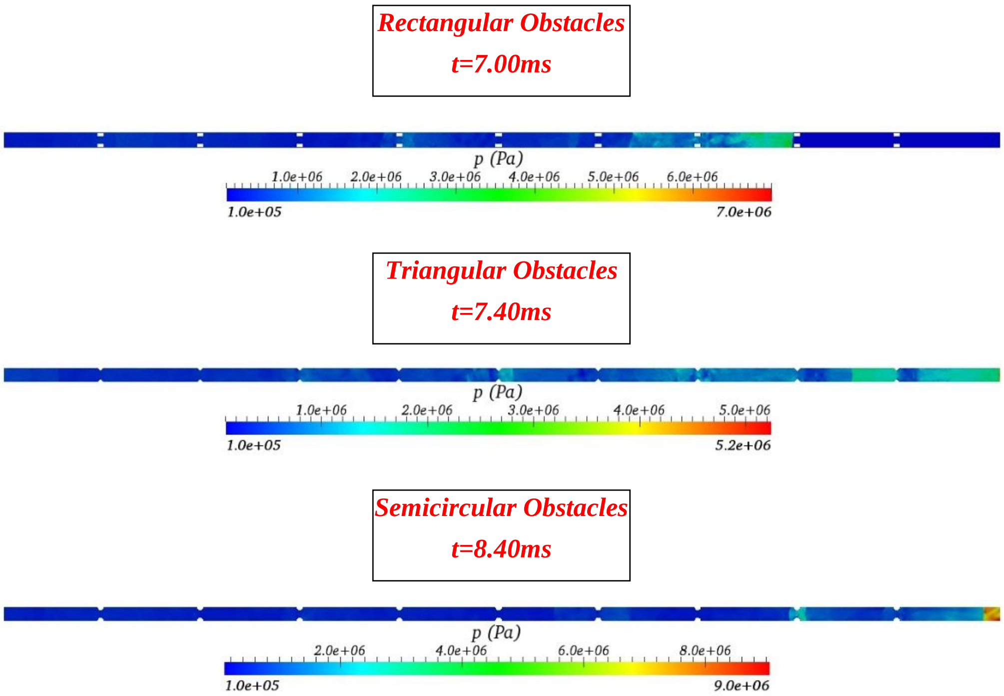

Figure 5.14 Maximum pressure location and time for three internal geometry configurations.

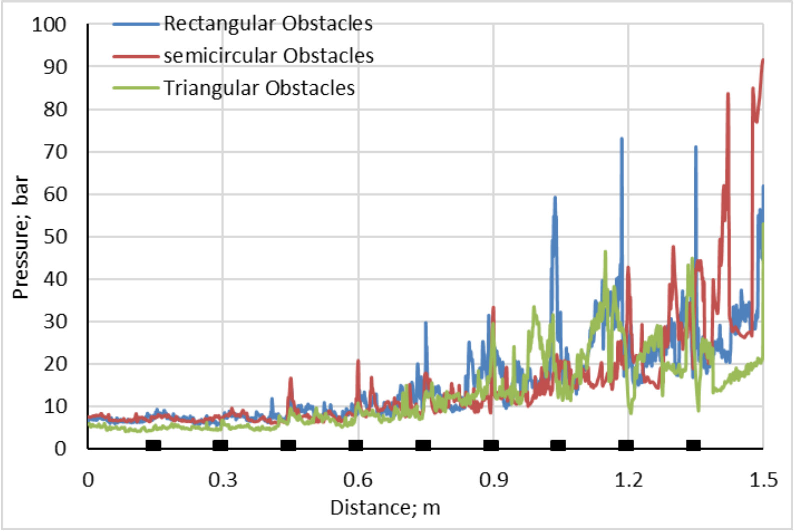

Figure 5.15 Maximum pressure trace during residence time along the tube.

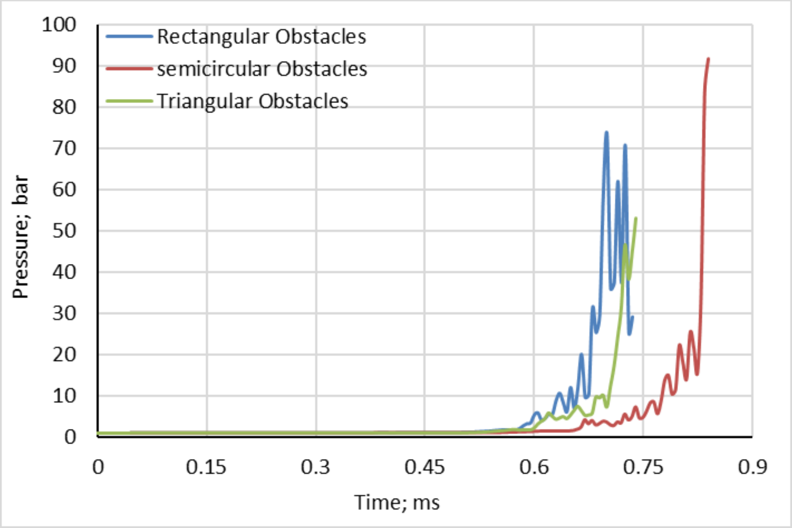

Figure 5.16 Maximum pressure trace along the tube with respect to time.

Pressure peaked at the centre of the triangular obstacles for the first four obstacles, figure 5.15. Pressure jumped irregularly regarding the location with the next obstacle, then it returns to peak at the centre of the sixth obstacle where detonation took place. The fluctuation increased from that point, and the pressure peak points were in different locations. The maximum pressure of 53.1bar was achieved by the end of the tube, which was the least pressure achieved among the three configurations. Pressure value ranged between 1.0bar to 2.0bar up to time 6ms, as it illustrated in figure 5.16. Pressure experienced alterations that rose eventually at 7.25ms up to 46.6bar, followed by a slight decrease previous to a re-increased profile before leaving the tube at the maximum pressure value.

The semicircular obstacles passed through the same conditions of the rectangular obstacles until the third obstacle, figure 5.15. Starting from the third until the eighth obstacle, pressures peaked at the centre of the obstacle. At the middle distance between the last obstacle and the end of the tube, the pressure encountered a dramatic accretion up to 82.1bar followed by an enormous reduction. Another dramatic increase in pressure occurred by the last 20mm of the tube followed by a tenuous decrease. Finally, the flame leaves the tube with a maximum value for pressure at 91.7bar. Figure 5.16 states that pressure moves slowly from 1.0bar to 2.0bar until 6.6ms, pressure then fluctuates with slight build up until 8.25ms when it undergoes a huge surge towards the end of the tube.

For the three configurations, the effect of the reflection and expansion waves interference are obvious. Reflected shocks are formed at the moment when the incident shock hits the obstacle, which is the same for the three configurations. For the rectangular cross-sectional obstacles, an expansion and diffraction waves are formed at the point when the shock wave reaches the last point on the obstacle upper side. This will give longer time for the reflected shock to affect the main incident shock before the expansion wave generated. This was the reason behind the steep augmentations.

The diffraction of the incident shock caused by the triangular obstacles is started around the tip of the obstacle [72]. Hence, the expansion waves merge with the reflected waves, which will decrease the expansion waves and the effect of the reflected waves on the main incident shock wave. Therefore, the jump in pressure with triangular obstacles is less sharp than the one with rectangular obstacles.

Unlike a sudden constriction in the rectangular obstacle, both triangular and semicircular obstacles generate sequential reflected shocks due to the gradual change in the flow area [160]. The reflected shocks generated at the second half of the obstacle, the part after the apex, will travel downstream. In the triangular obstacles case, sharp edges contribute in generating higher vortices which in turn reduce the severity of reflected shocks effect on the incident shock as it travelled downstream. This is not the case with semicircular obstacles, as the reflected shocks travelled towards the pipe exit are gradually consolidated to eventually thrust the pressure by the end of the tube.

Figures 5.17 and 5.18 show the ratios between products to reactants pressure, or the pressure ratio across the flame tip. As it was stated before, the pressure across the flame starts to fluctuate after the flame passes the second obstacle. The pressure ratio for the tube equipped with rectangular obstacles showed growth in both amplitude and frequency while moving downstream. When the flame approaches the seventh obstacle, the pressure ratio soars severely. The maximum products to reactants pressure ratio reached was 62.49 at x=1.1875m and t=7.00ms, which is where the maximum pressure has been achieved. The pressure ratio declines when it passes by the eighth obstacle and encounter a low increase through the ninth obstacle.

The tube equipped with triangular cross-section obstacles underwent less fluctuations. After the third obstacle, the pressure ratio steadily increases while the flame moves towards the next obstacle, and decreases when it goes through it. The ratio inadequately increases between the next pair of obstacles, and experiences more rapid rise entering the fifth obstacle and decreases through it. The pressure ratio steadily and tranquilly augments toward the eighth obstacle, where it encounters lesser decrease. Another increase is recorded at the midway between the last two obstacles. The flame finally leaves the tube with a pressure ratio of 45.32.

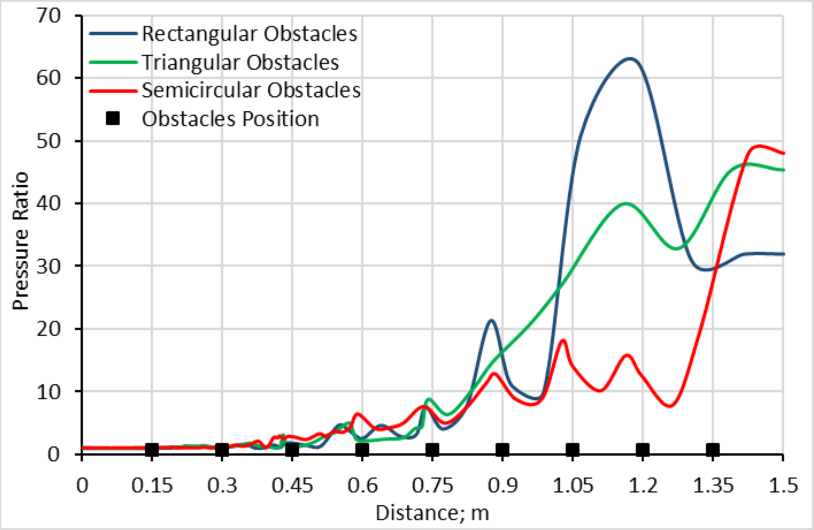

Figure 5.17 Pressure ratio across flame tip versus location along the tube.

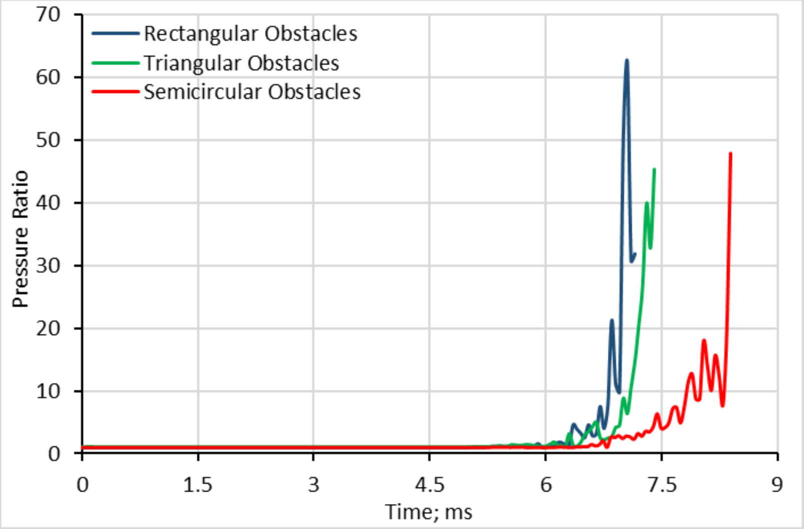

Figure 5.18 Pressure ratio across flame tip versus time along the tube.

While the flame moves downstream the tube equipped with semicircular obstacles, the pressure ratio showed more steady growth between obstacles. However, when the flame passes the before last obstacles, it decreased more than the other cases with the previous obstacles. This was followed by a dramatic accretion of pressure ratio reaching the maximum value 47.96 at the tube exit.

5.5 Conclusions

A comparison of the flame propagation using three obstacle geometries is required to understand how obstacle geometry affects flame acceleration. The combustion propagation is shown in figure 5.4 and the time versus distance graph shown in figure 5.5 stated that more than 60% of the residence time is consumed before the flame reaches the first obstacle, which is only 10% of the total distance. While it is required 26.1ms for the flame to reach the end of the tube without obstacles, only 32% of that time is required for the tube equipped with semicircular obstacles, this even is lesser with polygon shaped obstacles.

In order to compare the rate of flame acceleration in a stoichiometric hydrogen-air mixture for the all three obstacle configurations, the leading flame tip position is plotted in Figure 5.19. The slope of the curve at any given point represents the instantaneous flame velocity. All three curves show the same slow initial acceleration, followed by a more rapid acceleration and then terminating at a rather steady flame propagation velocity.

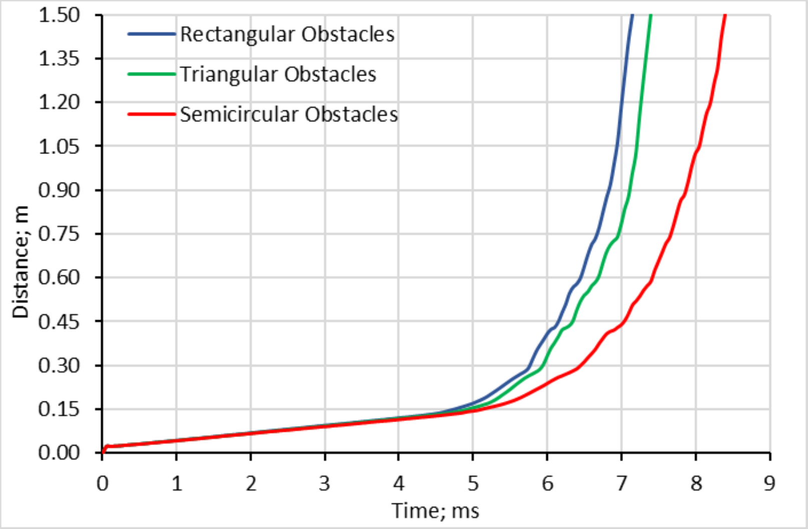

Figure 5.19 Pressure ratio across flame tip versus time along the tube.

The presence of edges in obstacles shows a clear effect on the flame propagation, even before the flame reaches it. The flame reaches the rectangular obstacles 3% earlier than the triangular obstacles and up to 7% the semicircular one. Influence then extends along the tube so that the combustion in the tube with rectangular obstacles accomplishes 3% earlier than the tube with triangular obstacles, but 15% earlier than the tube with semicircular obstacles. Also, it is found that the detonation velocity threshold is exceeded once with semicircular obstacles at t=8.25ms and last for a short period, while it is exceeded earlier and for longer period for both polygon obstacles.

However, semicircular obstacles possess two merits, the highest pressure, as the pressure is the desired outcome and the location where it is achieved. The curvature surface of the semicircular obstacle has produced the flow with the least turbulence, which helped in building up the pressure along the tube. Besides, the consolidated reflected shocks by the end of the tube, figure 5.20, promoting the pressure by the end of the tube to reach up to 91.2bar.

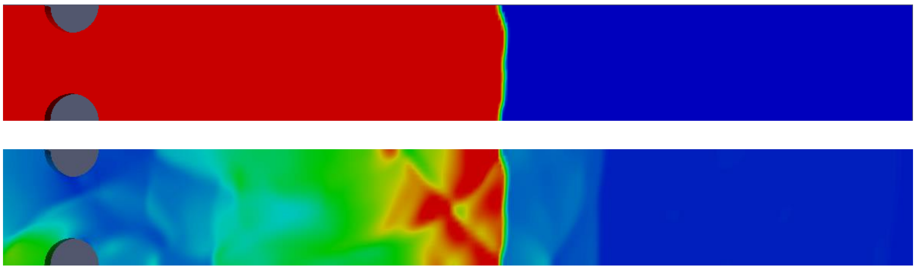

Figure 5.20 Flame front and reflected shocks travel ahead one time step before the end of the tube equipped with semicircular obstacles.

Although the earlier detonation was carried out by the tube with rectangular obstacles, the shortest deflagration to detonation distance was achieved by the tube with triangular obstacles. However, the pressure accomplished was the least among the three configurations, which was reached by the end of the tube. For the rectangular obstacles, detonation was not only achieved earlier, yet the maximum pressure was achieved at 79% of the total length of the tube. Thus, shorter tube might be more desirable with this configuration, unlike the two other configurations where longer tubes may maintain the continuation of pressure increase.

5.6 Summary

A numerical simulation has been performed in OpenFOAM to find out how the obstacle geometry could affect the flame propagation for an open end tube. A stoichiometric hydrogen/air mixture was used in a 21.2mm diameter and 1500mm length tube equipped with three different cross-section geometry obstacles.

The results of analysis demonstrated that the shock-flame interaction highly influences the flame propagation along the tube. Also, the sharp edges were found to affect recirculation produced by increasing drag. Therefore, the detonation speed threshold was exceeded earlier for rectangular obstacles. Yet, the flame velocity as higher and developed with shorter deflagration to detonation distance with triangular obstacles. This was mainly due to the separation point and its effect on the induced vortex behind the obstacle. However, as the pressure was the desired outcome, the tube with semicircular obstacles surpasses the two other configurations.

CHAPTER SIX

Geological Survey

6.1 Introduction

Shale is one of the most common types of sedimentary rocks. They have been formed by the deposition of different sediments and as a result vary in colour from red to green or black and in properties. High levels of organic matter and low levels of oxygen are the main requirements for this type of rock to be created. By lithification the organic matter is deposited gradually and as the time passes more material accumulates which then results in an increase in pressure and temperature. During this process, the organic material is transformed into kerogens which are long hydrocarbon chains [161].

This chapter is based on obtaining some of the shale rock characteristics out of samples obtained from the Dulais Valley, South Wales, and compare them with some others obtained from the Bowland-Hodder area, which has been demonstrated to have formations capable of producing good amounts of fossil fuel for human consumption.

6.2 Area of Interest

A 2010 report by the British Geological Society identified several potential shale gas deposits in northern England. First estimates were around 5.3tcf of gas reserves or 2 years of reserves based on current UK consumption rates. British gas company Cuadrilla Resources then estimated that there could be 200tcf of gas hiding in the Bowland shale [162].

These and posterior studies have determined a very good potential of extraction in this region known as the Bowland-Hodder area, figure 6.1. Carboniferous organic-rich basinal marine shales are present in this region. The shales are either buried at depth or occur at outcrop. These organic-rich shales are recognised to be excellent source rocks, in which oil and gas matured before some of it migrated into conventional oil and gas fields [163].

Figure 6.1 Bowland-Hodder area, UK [162]**.**

Wales is also carrying out several exploration projects through various companies to recognise areas where to exploit the resource in order to contribute with this energetic revolution. North Wales, having a share in the Bowland-Hodder unit can highly benefit from this region. However, there are some other regions of interest close to South Wales where the extraction could be linked to a high populated area that includes the capital, Cardiff, and the surrounding valleys. According to the Department of Energy and Climate Change [164], there is a good prospect for shale extraction in this region.

6.3 Experimental Setup

Specimens were collected at the British Geological Survey Centre. In total 11 samples were obtained from 6 different boreholes located in South Wales (Dulais Valley) and the Bowland-Hodder area (Smeathalls, Wingfield, Edale, Kingsmill and Milfordhall), figure 6.2.

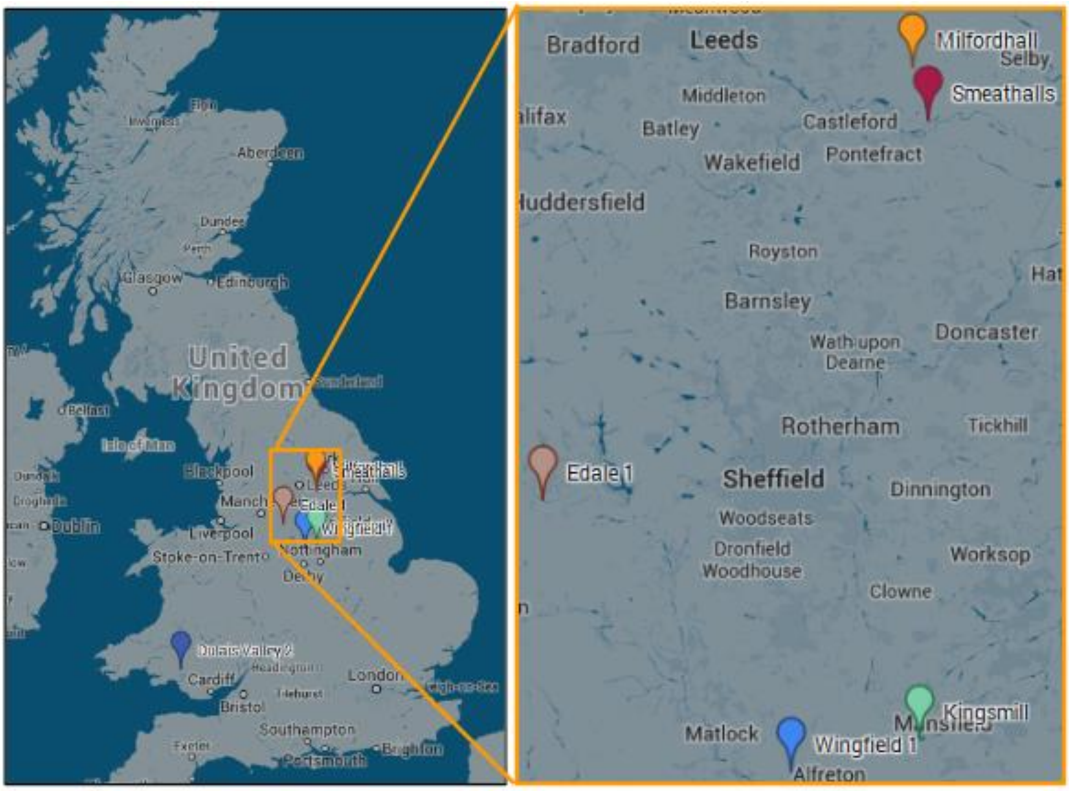

Figure 6.2 Location of samples.

The size of the subsample depended entirely on the size of the actual sample which varied in each site. It should be noted that most if not all of the samples had a dark grey to black colour. Generally speaking, there is a correlation between the colour of the shales and the potential content of gas and or oil. The darker the colour the more organic material there is [165], which suggest the shale was formed in an oxygen depleted environment and hence more likely it is to contain hydrocarbons. Three techniques have been used in the present work to characterise and compare the samples.

6.3.1 Volatile Content

Volatile matter is the material that changes state from a solid to gaseous state when heated to specific conditions for a period of time without the presence of oxygen. Most of the solid which volatilises in shale is comprised of free hydrocarbons present in the sample, i.e. kerogen which is cracked with the heat and yields hydrocarbons and CO_2 among other compounds [166].

In order to recognise the volatile matter, experiments were carried out based on the standard BS ISO 562:2010 Hard coal and coke determination of volatile matter [167].

The objective was to find the volatile matter in the shale rocks. The process was as follows:

1. Crushing of each sample in mill until it reached a fine powder consistency.
2. Placement of each sample on an evaporating dish and then put all the samples inside an oven for an hour at a temperature of 105°C in order to remove moisture.
3. Measurement of one gram of the sample and then put it inside of a crucible. Repeat this step two times, so there are three crucibles, each with one gram of the sample.
4. Placement of crucibles in oven for seven minutes at a 900°C temperature.
5. Removal and weight measurement of the sample, recording the mass loss.
6. Repetition of step 3 to 5 for each of the samples.

6.3.2 RockEval Pyrolysis [168]

One of the most common methods used to analyse the potential of shale rocks is referred to as RockEval pyrolysis. This was performed in conjunction with a previous MSc student [168]. The procedure is as follows:

1. The rock samples are pulverised.
2. Pulverised samples are heated for three minutes at a temperature of 250°C.
3. Then samples are heated gradually from 250°C to 600°C at 25°C per minute.

The process was carried out in the absence of oxygen, and during the time water, carbon dioxide and hydrocarbons are released from the rock [169]. The important parameters obtained from the process are:

- S1: Amount of hydrocarbons measured in milligrams per gram of rock released at initial heating of 250°C, table 6.1.
- S2: Amount of hydrocarbons produced upon pyrolytic degradation of the remaining organic matter in the rock, table 6.1.

- S3: Amount of carbon dioxide generated during the pyrolysis.
- T_{max}: Temperature at which most hydrocarbons are released. It is an indication of the rock thermal maturity [170], [171].
- TOC%: Total Organic Carbon, table 6.1.
- PI: Production Index and also indicates thermal maturity. PI values below 0.4 are thermally immature, between 0.4-1 are thermally mature and above 1.0 indicate over mature organic matter [172], table 6.3.
- Ro%: Vitrine reflectance: Parameter to identify the maximum temperature history of sediments. It is used as an indicator of maturity in hydrocarbon rocks.
- HI: Hydrogen Index is obtained using S2 and TOC, and can be used as a maturation indicator [170], [171], table 6.2.
- OI: Oxygen Index is a parameter that correlates with the ratio of oxygen to carbon [170].

Table 6.1 Geomechanical parameters describing Source Rock Generative Potential [170].

Potential	TOC (weight %)	S1 (mg HC/g rock)	S2 (mg HC/g rock)
Poor	0.0-0.5	0.0-0.5	0.0-2.5
Fair	0.5-1.0	0.5-1.0	2.5-5.0
Good	1.0-2.0	1.0-2.0	5.0-10.0
Very Good	2.0+	2.0+	10.0+

Table 6.2 Geomechanical parameters describing Type of Hydrocarbon Generated [170]

Type	Hydrogen Index (HI)
Gas	0-150
Gas and Oil	150-300
Oil	300+

Table 6.3 Geomechanical parameters describing Level of Thermal Maturation [170]

Maturation	Production Index (PI)	T_{max} (°C)
Top Oil Window	Ca. 0.1	Ca. 435-445
Bottom Oil Window	Ca. 0.4	Ca. 470

6.3.3 High Resolution Transmission Electron Microscope (HRTEM)

Laboratory characterizations have revealed that gas shales have low porosity (<10% of pore space in a unit volume of rock) and ultralow permeability (tens of nanodarcy), with the majority of gas stored in the kerogen nanopores [173]. Scanning electron microscopy and transmission electron microscopy images can offer important information regarding the nanometer-scaled pore geometry in gas shale. They can also offer information about element tracing for the assessment for environmental impacts during hydraulic fracturing. Impacts such as potential for acid rock drainage generation, distribution of trace elements in shale gas and management of well cuttings are just some example assessments that can be carried out with these studies.

To provide detailed morphological and compositional information about the studied samples at micro and nano-scale, a high-resolution transmission electron microscope (HR-TEM) system JEOL 2100 (LaB6) was employed. The state-of-the-art instrument is equipped with a high-resolution Gatan digital camera (2k x 2k) providing resolution of 0.2Å which makes possible detailed observation of the crystal lattice, obtaining diffraction pattern and accurate measurement of the lattice d-spacing with the help of Digital Micrograph software. In scanning transmission electron microscopy (STEM) mode, a dark field (HAADF/Z-contrast) detector was used to provide excellent compositional contrast. Energy Dispersive X-ray Spectrometry (EDS) system Oxford Instruments equipped with a large-area 80mm^2 SDD (Silicon Drift Detector) X-MaxN 80 T was employed to study the elemental analysis in Point&ID, LineScans, layered and elemental mapping modes. To analyse the EDS data, the latest version of AZtecTEM software was utilized. For HR-TEM analysis, after preparing a (water) suspension from the samples, a drop of about 8μL was put on the TEM grid and dried.

Launched since March 2013 at Cardiff University, the state-of-the-art instrument features high-resolution Gatan digital camera with resolution 0.02nm, dark field (HAADF detector) imaging in STEM mode, 3-D tomography with high-stability goniometer stage specifically tuned for high tilt tomographic applications, EDS elemental analysis with elemental mapping and line scan capability and CRYO imaging at -175°C.

The diameter of the samples studied was close to 2mm and due to the magnification capacity each one was studied at five different locations within each sample. For each sample and each location, the percentage of each element was obtained. Subsequently, an average value for each sample was calculated.

6.4 Results and Discussion

The difference in mass of the samples was divided by the total mass to find the volatile contents. Average results are given in table 6.4 for all the samples. Although this is a rough estimate of the possible presence of hydrocarbons, the results determine that all regions are candidates for the exploitation of fossil sources. As it can be seen the values of shale rocks range from 7.05 to 20.65% which is an indication that they may contain sufficient hydrocarbons for them to be source rocks. However, it is clear that the region in South Wales contains the lowest percentage in the batch, an indication of a poor/fair content of hydrocarbons. Nevertheless, the volatiles which are given off should be measured to ensure there is oil and or gas with more specialist equipment.

Table 6.4 Average volatile organic content of each shale rock sample.

ID	Name of borehole location	Elevation above sea level at surface (m)	Depth relative to surface (m)	Volatile Organic Content (%)
1A	Dulais Valley 1	134.60	166.12	9.62
2B	Dulais Valley 2	134.60	155.83	7.05
3C	Smeathalls 1	10.03	229.34	14.14
4D	Smeathalls 2	10.03	219.89	9.0
5E	Wingfield 1	125.02	31.95	13.76
6F	Wingfield 2	125.02	54.63	11.86
7G	Edale 1	235.10	96.01	15.40
8H	Edale 2	235.10	99.06	14.37
9I	Kingsmill 1	116.12	216.76	15.48
10J	Kingsmill 2	116.12	725.42	20.65
11K	Milfordhall 1	17.55	325.02	9.00

From the RockEval pyrolysis evaluation average results for all the samples can be found in table 6.5. The quantity of organic matter in the samples indicated by the total organic carbon (TOC) ranges from 0.63 to 20.12%. All of these values are above 0.5%, thus showing that the amount of organic matter in the samples go from fair to very good. The thermo-labile hydrocarbons (S1) average value is 0.47mg/g, ranging from 0.03 to 1.31mg/g. The first two samples from Dulais Valley show the lowest content. Hydrocarbons from cracking of kerogen (S2) show an average of 7.88mg/g being in the “good” range. Only three of the samples are categorised to have poor potential, those from South Wales with the lowest values.

Table 6.5 Rock-Eval pyrolysis results from studied samples.

ID	S1	S2	PI	T_{max}	S3	TOC	HI	OI
1A	0.05	0.70	0.07	586	1.17	4.05	17	29
2B	0.03	0.21	0.14	393	0.40	0.63	33	63
3C	0.55	26.71	0.02	429	4.06	15.31	174	27
4D	0.19	8.92	0.02	438	0.91	3.79	235	24
5E	0.23	4.41	0.05	425	0.28	4.22	105	7
6F	0.24	9.92	0.02	437	0.27	3.35	296	8
7G	1.31	5.30	0.20	451	0.24	5.84	91	4
8H	1.08	3.03	0.26	437	0.32	4.56	66	7
9I	0.12	0.81	0.13	434	0.27	1.00	81	27
10J	1.15	21.55	0.05	431	6.37	20.12	107	32
11K	0.20	5.09	0.04	436	0.58	2.91	175	20

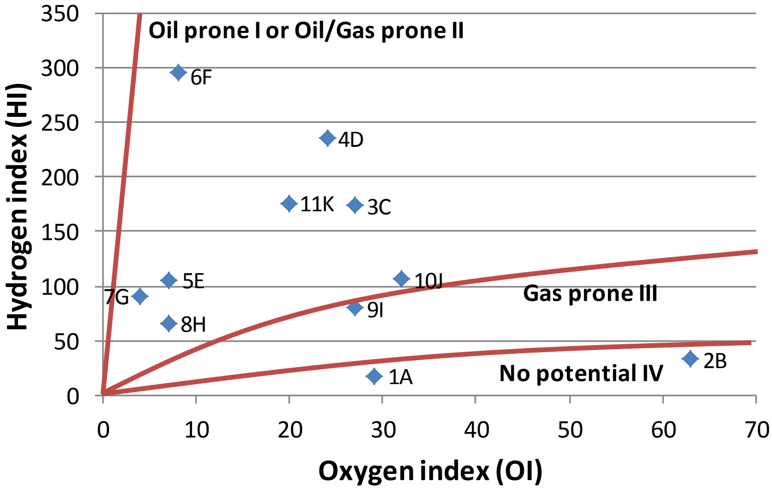

Figure 6.3 Hydrogen index vs. oxygen index plot (Modified Van Krevelen diagram).

Figures 6.3 and 6.4 show the two most widely used diagrams to interpret the origin of the organic matter in rocks. Figure 6.3 shows the hydrogen index versus the oxygen index. This provides a rough estimate on the type of organic matter present in the samples and what hydrocarbon they will mostly yield. Figure 6.4 is the hydrogen index versus T_{max}. This diagram is based on the amount of hydrogen the kerogen contains and the amount of energy needed to produce hydrocarbons from that type of kerogen under laboratory conditions [174].

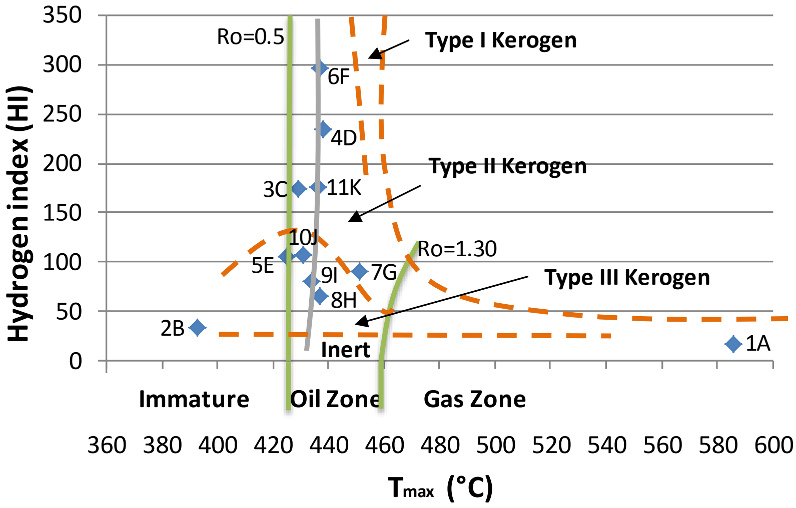

Figure 6.4 T_{max} vs HI plot.

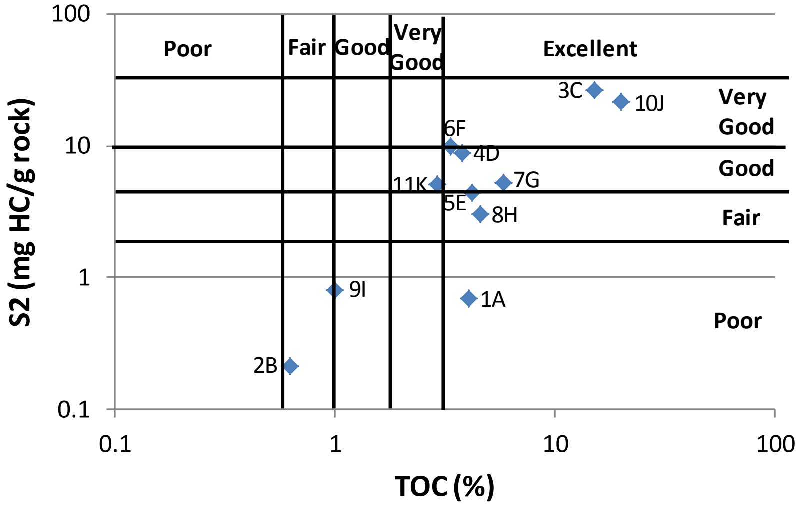

Figure 6.5 Source rock characteristics as interpreted by the relationship between the remaining hydrocarbon potential (S2) and TOC.

Rock Eval thermal maturity parameters, indicated by T_{max} and approximate vitrinite reflectance between 0.5 and 1.30 Ro%, suggest that most samples from the Bowland-Hodder area are located in the mature oil window with different kerogen types, figure 6.4. However, the samples from South Wales show inert, no potential specimens either from immature samples or post-mature rocks. Other RockEval parameters (S1, S2, HI) are quite low and indicate a poor source potential for the Dulais Valley region, contrary to those samples obtained from the Midlands, figure 6.3 and table 6.5. The source rock potential was also characterised, figure 6.5. Although the total organic carbon in the **1A** sample is excellent, its remaining hydrocarbon potential is poor. In the case of sample **2B**, it is clear that its poor characteristics show an immature deposit of rock.

Contrary to these findings, shale rocks in the Bowland-Hodder area denote a good potential for further exploitation of the resource.

Regarding element tracing analyses, comparisons between the South Wales samples and the Bowland-Hodder region were performed using the average value of the averages of the latter with the former, table 6.6.

The results showed a consistent presence of Iron Sulphide (FeS_2) or pyrite in all the samples, table 6.6, resembled in the content of Fe and S. One of the main concerns with this type of compound is that it is known to cause acid main drainage when exposed to oxygen and water. During the process of fracking, this element will be dissolved since water will be used for the hydraulic fracturing process and once the liquid flows back to the surface it will be exposed to the oxygen in the air. The three main problems associated with the release of acid to the main drainage are contamination of drinking water, detrimental effects on aquatic plants and animals, corrosion of infrastructure such as bridges, monuments, and buildings [175].

Table 6.6 Average element composition of all samples.

Element	Dulais Valley	Smeathalls	Wingfield	Edale	Milfordhall	Average Bowland-Hodder	Comparison
O	43.760	46.310	54.910	49.370	53.950	51.14	0.86
Si	20.360	18.200	20.470	23.560	20.610	20.71	0.98
C	16.030	21.250	5.830	15.350	7.280	12.43	1.29
Al	10.680	8.220	14.580	5.350	12.250	10.10	1.06
Fe	4.810	2.400	0.770	0.760	1.240	1.29	3.72
K	2.490	1.190	1.280	0.490	2.420	1.35	1.85
Mg	0.750	0.890	0.470	0.430	1.070	0.72	1.05
Ca	0.480	0.150	0.610	2.920	0.060	0.94	0.51
Na	0.210	0.170	0.002	0.050	0.230	0.11	1.86
P	0.140	0.000	0.000	0.120	0.030	0.04	3.73
Ti	0.130	0.090	0.340	0.040	0.320	0.20	0.66
Mn	0.110	0.040	0.000	0.010	0.020	0.02	6.29
S	0.050	1.090	0.740	1.550	0.060	0.86	0.06
Cu	0.000	0.000	0.000	0.000	0.460	0.12	0.00
Total	100.00	100.00	100.00	100.00	100.00	100.00	1.00

However, it is evident that the amount of Fe in the South Wales samples is much higher (i.e. more than three times) than those in the Bowland-Hodder region. On the other hand, S is at the lowest level, thus showing that the extraction of the shale in this region would be less damaging in terms of acid content coming from this molecule. Troilite (FeS) and Pyrite (FeS_2) were detected in some of the samples, as can be confirmed by the structured shape of the rocks and elemental mapping, figures 6.6 and 6.7. However, the samples in the Dulais Valley contain $CaPO_4$, $CaHPO_4$ or similar compounds, thus increasing the acidic elements in the sample. It is very likely that gypsum ($CaSO_4 \cdot 2H_2O$) is also present in the samples, with clear indication of Ca, S and oxygen in all of them, figure 6.8. All samples showed traces of K. Quartz (SiO_2) seems to be also one of the major components of the rocks, and these elements are present in a similar percentage in both regions. Finally, uranium is an element that seems to appear only in Milfordhall. Although it does not show traces in other boreholes, further considerations need to be evaluated in those sites where these naturally occurring radioactive materials are present, a problem that does not seem to affect the Dulais Valley.

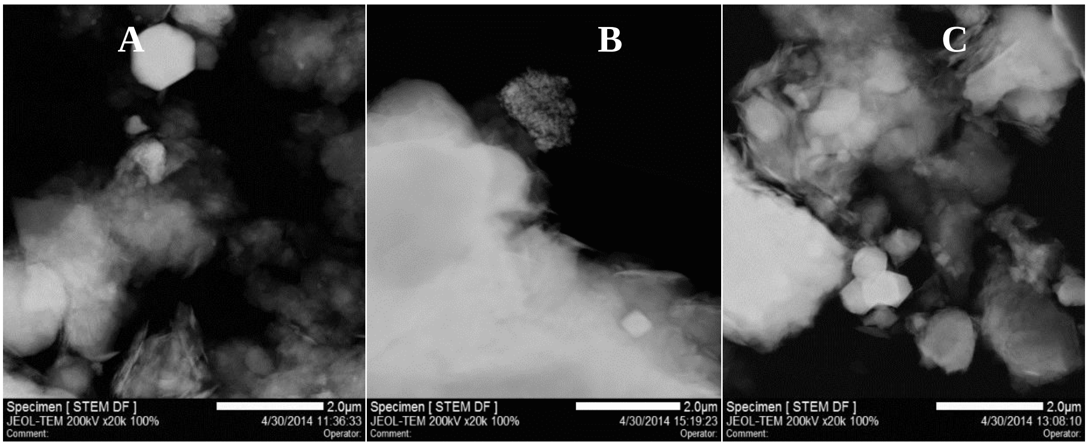

Figure 6.6 Traces of Troilite (FeS) and Pyrite (FeS_2) in samples A) 3C, B) 5E and C) 7G.

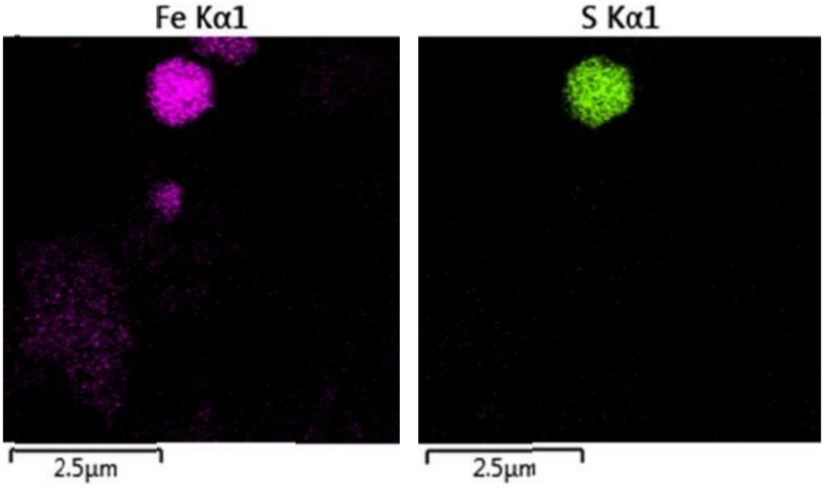

Figure 6.7 Mapping of sample. Traces of Troilite (FeS) in sample 3C.

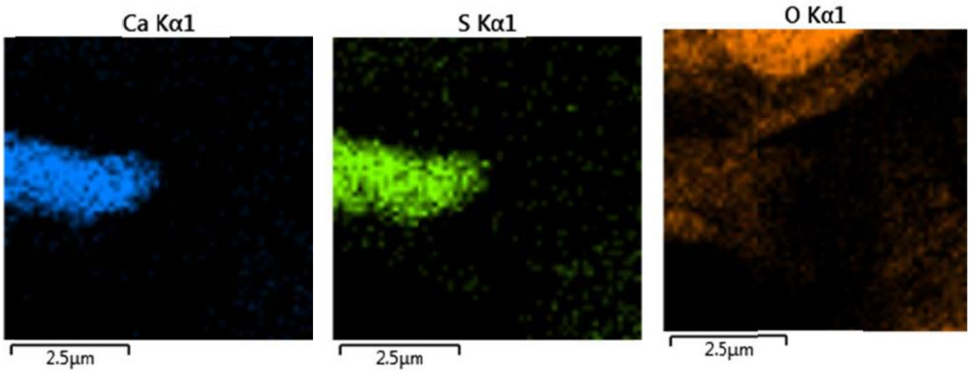

Figure 6.8 Mapping of sample. Traces of gypsum in sample 5E.

6.5 Conclusions

Several studies were performed to give an indication of the potential of the Dulais Valley in terms of producing shale gas. It was found that the resources in the region are low, with rocks that show a poor potential for the production of gas. Comparison with good sources coming from Yorkshire and the Midlands gave indication of very low potential for extraction in the Dulais Valley. In terms of element composition, the rocks seem to have higher levels of Fe. However, the low S indicates that these are not bounded as FeS or FeS_2, and probably a cleaner extraction could take place. This is also dependent on the amount of other molecules such as gypsum, which seem higher in South Wales. It can be concluded that this region possesses low potential, and although being included in the zone of onshore licenses, the benefits of exploitation might not be high. However, it is recognised that the amount of samples needs to be increased and more research is needed to define if the region of South Wales has good potential for the exploitation of the resource.

CHAPTER SEVEN

Simulation of Crack Propagation

7.1 Introduction

The mechanical characterisation of shale formation is considered as the main issue in modelling crack propagation. The non-uniform sedimentation during the shale formation process presents distinct types of patterns in shale. For that, the analysis done for a specific shale rock is not valid elsewhere, even along a wellbore [117].

In this chapter, the influence of pressure produced by the detonation tube on the shale rock in shale formation is investigated. A two-dimensional study using ANSYS Parameter Design Language (Mechanical APDL) was performed with shale rock properties to predict the pressure pulse generated by the detonation tube on a crack tip which assumed to be created by perforation.

7.2 Simulation of Crack Propagation

Many researches have been dedicated to simulating fracturing in shale gas extraction. However, simplifications adopted and the assumption made led to lack in provided information. Dealing with shale rock as an isotropic material, crack branching and natural fractures already found in the shale formation represent the major causes of deviation.

Hydraulic fracturing is the dominant way in fracturing process for shale gas extraction. Therefore, most of the researches conducted have dealt with hydraulic fracturing. The majority of these researches took into account only the influence of the crack neglecting the fluid effect. The fluid-crack interaction was included in recent few researches [176]–[178]. However, the current study will deal with dry fractures and the effect of pressure pulse generated by the detonation tube on the pre-crack generated from the perforating stage.

7.3 Fracture Mechanics

Fracture mechanics deal with the conditions under which cracks are formed and grown. Fracture mechanics analyse stress in the vicinity of a crack or flaw. They are basically based on the analytical procedure related to three variables, which are material properties, flaw size and shape, and applied stress [122]. Fracture process is summarised by Naman [179] in four steps. The first stage is related to the stress concentration in the vicinity of the defects. The second stage is related to the formation and initiation of the crack. In the present work, both previous stages are caused deliberately during the perforating stage of shale gas extraction. The real beginning of the crack starts with the third stage. In this stage, a successive propagation of the crack is attained until a certain distance called critical size is reached. In the fourth stage, a sudden propagation is caused.

Depending on the direction of applied load, three modes of fracture are recognised, as illustrated in figure 7.1:

a. **Mode I**: Opening mode, where the two crack surfaces are pulled apart in the $y-$direction, but the deformations are symmetric about the $x–z$ and $x–y$ planes,

b. **Mode II**: Shearing mode, the two crack surfaces slide over each other in the $x-$direction, but the deformations are symmetric about the x − y plane and skew symmetric about the $x–z$ plane.

c. **Mode III**: Tearing mode, the crack surfaces slide over each other in the $z-$direction, but the deformations are skew symmetric about the $x–y$ and $x–z$ planes.

The propagation of a crack may follow one of the above modes or a combination of them.

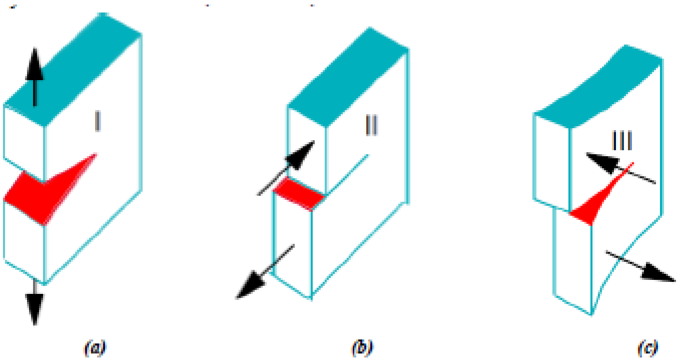

Figure 7.1 Modes of crack displacement [180]**.**

7.4 Stress Intensity Factor

The stress intensity, caused by a remote load or residual stresses, near the tip of a crack in fracture mechanics is predicted by a factor known as stress intensity factor (SIF), which is used to estimate the crack growth rate. This factor was first developed by G. Irwin in 1957 [121]. Stress intensity factor determination plays a central role in linear elastic fracture mechanic problems. The stress field near the crack tip rules fracture propagation.

The stress intensity factors can be calculated using stress and strain analysis or parameters that measure the energy released by crack growth. The calculation of the stress intensity factor (SIF) under the effect of the dynamic load and identifying its behaviour under the influence of dynamic load is a way to predict the emergence of a crack. The stress intensity factor is the quantity which dictates if or when the crack will propagate.

Application of cyclic load increases the crack length cumulatively. The nature of the problem in the present work led to focus on investigating Mode I stress intensity factor calculations at the tip of the crack. The stress near the crack tip, figure 7.2, is formulated as [122],

$$\sigma_x = \sigma\frac{\sqrt{a}}{\sqrt{2r}}cos\frac{\theta}{2}\left(1 - sin\frac{\theta}{2}sin\frac{3\theta}{2}\right),\quad \sigma_y = \sigma\frac{\sqrt{a}}{\sqrt{2r}}cos\frac{\theta}{2}\left(1 + sin\frac{\theta}{2}sin\frac{3\theta}{2}\right)$$

Equation 7.1

where σ is nominal stress in N/m^2 and a is crack length in m.

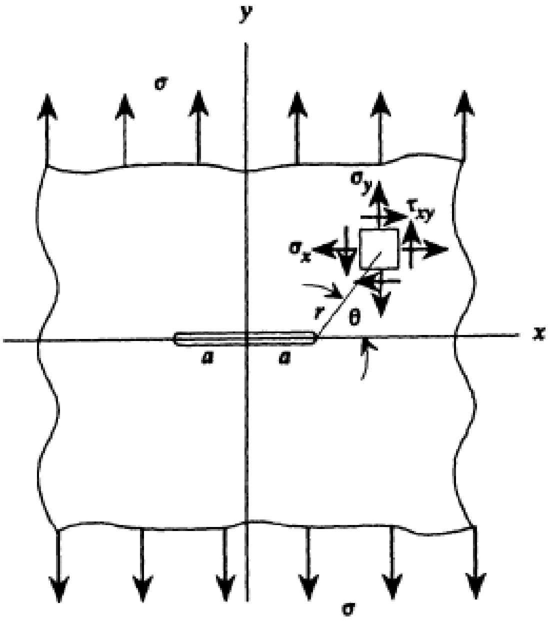

Figure 7.2 Distribution of stresses near a crack [122].

Thus, stress intensity factor of mode I (K_I) has been defined in the equation 2.17. There are three kinds of cracks, central, double-edge and single-edge crack. In this particular case, the crack was assumed to be single-edge crack, which is expected to be produced by perforation process, as illustrated in figure 7.3. Thus, assuming linear elastic fracture mechanics (LEFM) and plane strain problem, the constant C from equation 2.16 will be [122],

$$C = \sqrt{\frac{2w}{\pi a} \tan\left(\pi \frac{a}{2w}\right)} \frac{0.752 + 2.02(a/w) + 0.37[1 - \sin(\pi a/2w)]^3}{\cos(\pi a/2w)} \qquad \textbf{Equation 7.2}$$

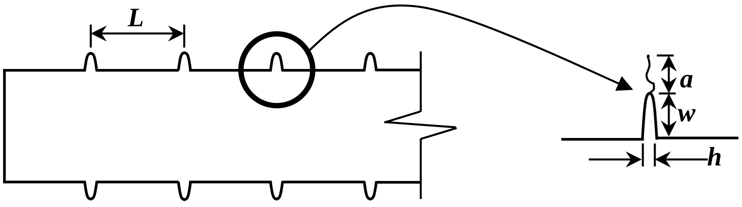

Figure 7.3 The shape of the assumed crack.

Critical intensity factor, also known as fracture toughness, is an important parameter that measures the ability of any material containing a crack to resist fracture. The critical intensity factor is a measured material property, found by loading standard specimens until crack extends. The crack growth occurs when the stress intensity factor surpasses the critical stress intensity factor [181].

7.5 Von Mises Stresses

The geometrical combination of normal and shear stresses acting at a particular location is called Von Mises stress. The material yields at a location when the Von Mises stress exceeds the yield strength, and ruptures at that location when it exceeds the ultimate strength. Von Mises stress is defined as [182]

$$\sigma_{VM} = \sqrt{\left(\sigma_x + \sigma_y + \sigma_z\right)^2 - 3\left(\sigma_x\sigma_y + \sigma_y\sigma_z + \sigma_z\sigma_x - \tau_{yz}^2 - \tau_{xz}^2 - \tau_{xy}^2\right)}$$

Equation 7.3

Von Mises yield criterion stated that a material can fail despite none of the individual component stresses exceeded the stress threshold for plastic deformation [182].

7.6 Numerical Setup

7.6.1 Geometry and Mesh Generation

The depth of vertical and length of horizontal drilling of any shale gas well depends mainly on the area subjected to exploration, figure 7.4. Generally, diameter of the well starts from 610mm at the ground surface to 140mm at the horizontal well, through three or four intermediate diameters [183]. The horizontal well then is perforated using shaped-charge perforator, shown in figure 7.5. The perforating gun detonates the shaped charge with a velocity that ranges from 7600m/s to 9100m/s, creating an impact pressure of 70GPa to 100GPa. The charge penetrates the casing and surrounding rocks with a diameter that ranges from 6mm to 18mm for 0.15m to 1.2m in the formation depending on the standoff of the perforating gun from the casing. A perforating gun usually shoots 12 to 18 shoots per meter (4-6 spf) [184].

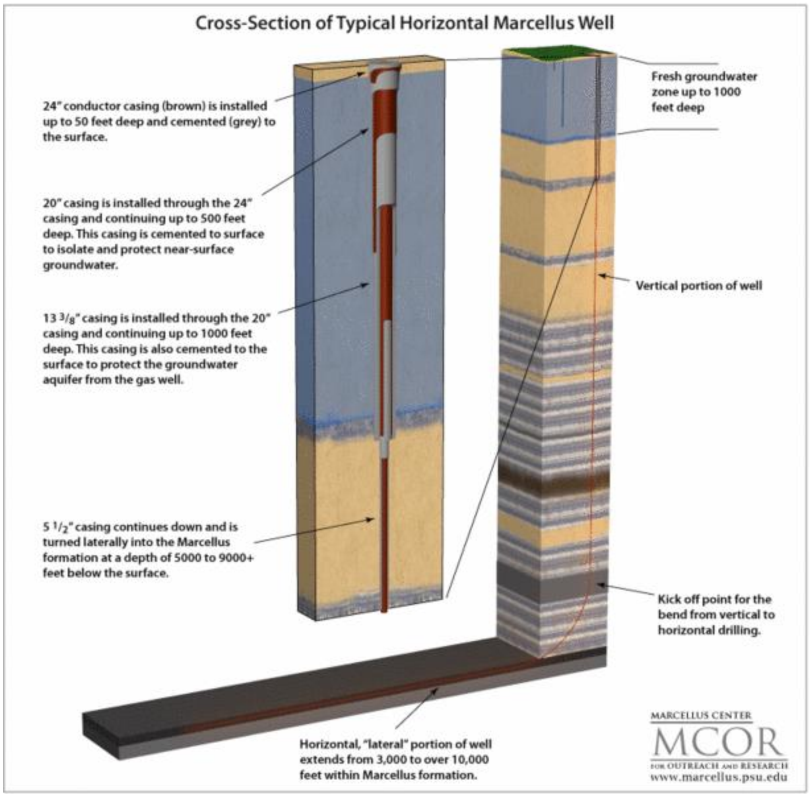

Figure 7.4 Typical shale gas well [183].

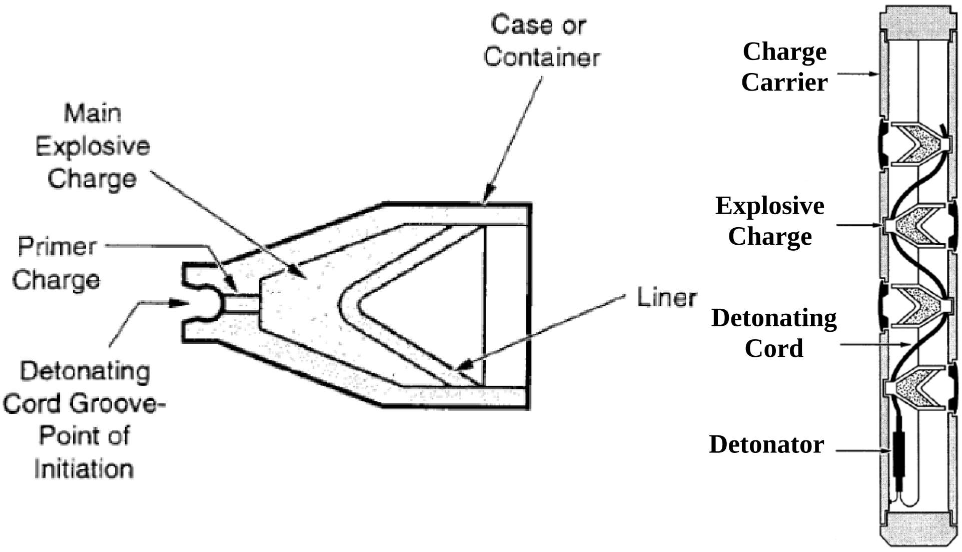

Figure 7.5 Sketch shows perforating gun (right) and shaped charge (left) [184].

The mesh was generated using "PLANE183" in ANSYS code, which is a 2-dimensional 8-node quadratic element, figure 7.6. The number of divisions is determined on the lines constructed the modelled body. The divisions then concentrated in the vicinity of the crack area using space ratio option. Space ratio is the nominal ratio of the last division size to the first division size.

To model the stress concentration around the crack tip, the crack tip point was chosen as a keypoint, this point was set where the mesh is concentrated and then refined to capture the crack propagation. A circle with a radius of one-eighth of crack length (a/8) is drawn around the crack tip point. The crack opening is set to be a/200, as recommended by the software. The element is degenerated to a triangular-shaped circumference around the keypoint and radially away [185]. Figure 7.7 shows the mesh around the crack tip area.

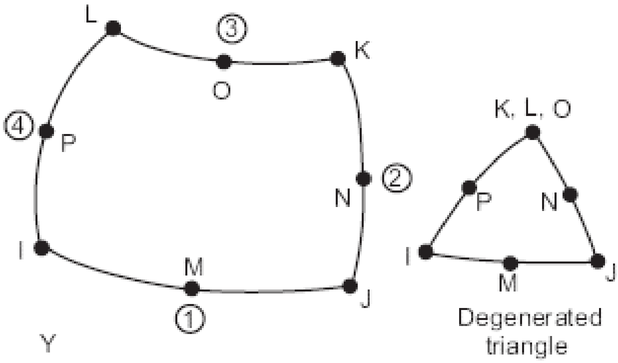

Figure 7.6 PLANE183 element geometry [185].

Table 7.1 Dimensions and mesh properties for the model.

Line	Length(m)	No. of divisions	Space ratio
Geometry height (L1)	0.11	110	-
Geometry length (L2)	4	4000	-
Space between holes (L3)	0.1	100	0.2
Perforating depth (w)	0.1	100	0.2
Perforating diameter (h)	0.01	20	0.2
Pre-crack length (a)	0.01	-	-

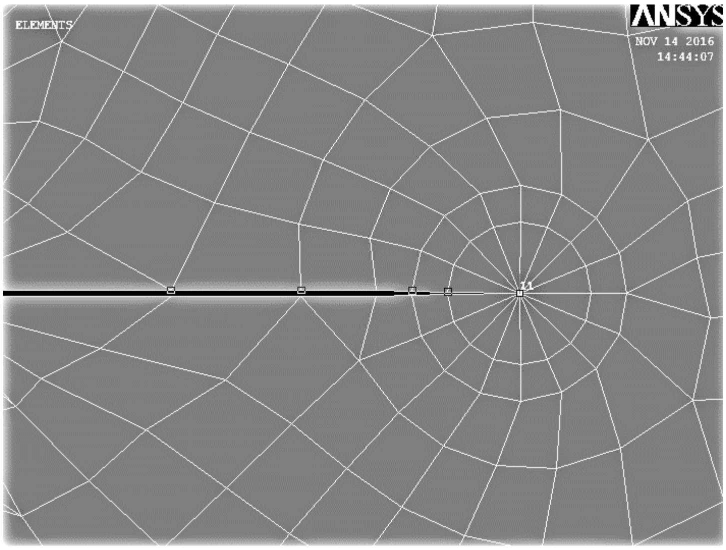

Figure 7.7 Mesh near the crack tip.

7.6.2 Boundary and Initial Conditions

The geometry used in the simulation is illustrated in figure 7.8. The dimensions of the hole generated by perforating have been taken from literature [184]. A pre-crack has been assumed to initiate as consequence of perforating. All these dimensions, illustrated in figure 7.3, are tabulated in table 7.1.

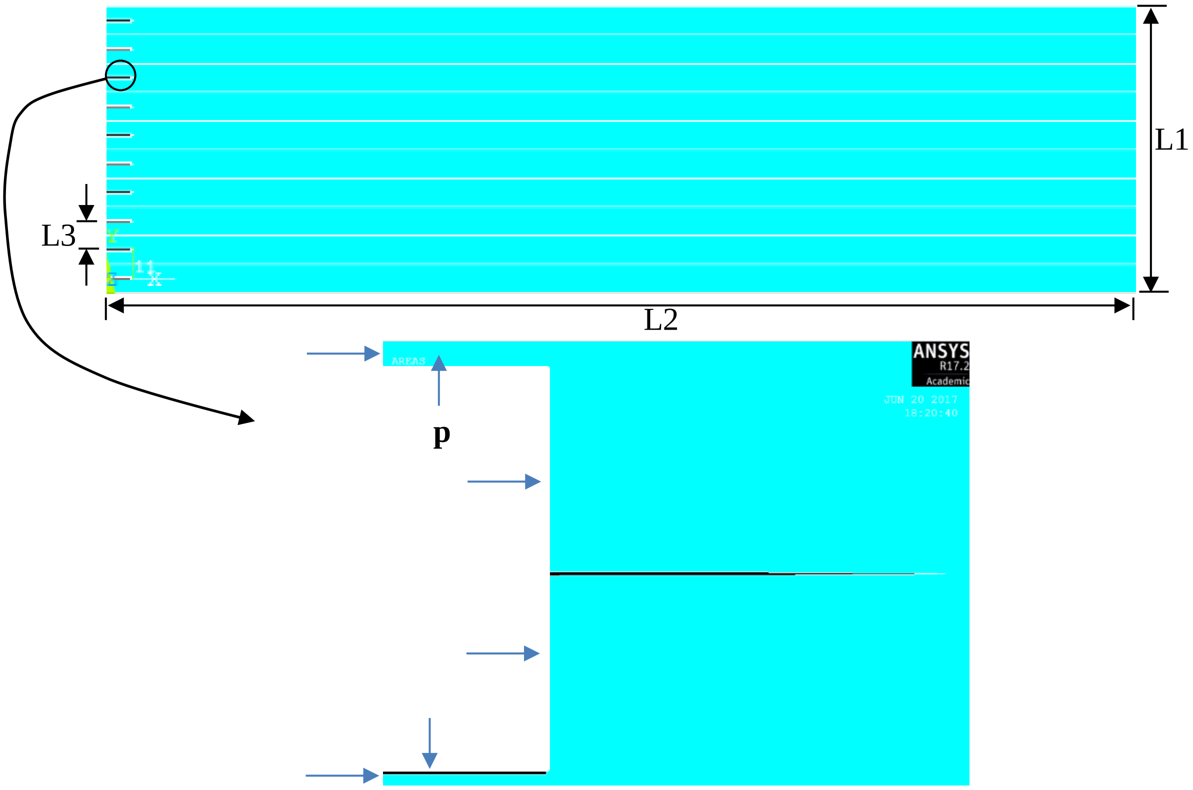

Figure 7.8 Simulated geometry.

The shale rock mechanical properties depend mainly on the conditions that the rock has been formed in and the compositions of the rocks, clay and organic matter (kerogen) [185]. Therefore, the mechanical properties of shale rock are not alike even along the same well, as mentioned previously. Mancos shale mechanical properties have been used in the present study [123], mainly because all the mechanical properties needed are found in this reference. Table 7.2 shows the input data used in the code for crack-plane orientations relative to bedding, assuming that the bedding plane was oriented along the x-axis.

Table 7.2 Shale rock mechanical properties [123].

Property	
Fracture Toughness (K_{IC})	0.21MPa.m$^{1/2}$
Tensile strength (σ_T)	4.54MPa
Modulus of elasticity (E)	11GPa
Poisson's Ratio (ν)	0.2

The model was loaded by applying a pressure pulse wave that exerts in all directions, as it is illustrated in figure 7.8. The magnitudes of pressure used here were (50, 70, 90) bar, to cover the pressure range achieved by the detonation tube.

7.7 Results and Discussion

One of the most powerful features of APDL is its ability to map any results data onto arbitrary path through the model. This enables user to perform many mathematical and calculation operations along this path to determine meaningful results: stress intensity factors around a crack tip, the stresses along the path, displacement, and so on. Another benefit is that it is possible to see, in the form of a graph or a tabular listing, how a result item varies along the path. To review results on a path, three steps must be followed. The first is defining the path attribute, the environment and the measured points. The second is defining the data which will be mapped through this path. The last one is interpolating results data along the path [186].

In the present work, four paths were chosen to find the stresses and stress intensity factors. Two horizontal, the first, crack tip path, starts from the crack tip and extends up to the end of the geometry. The other, edge path, starts from the beginning to the end of the geometry but at the level between two adjacent perforating holes. The other two paths are vertical, and they are parallel to the perforating base, vertical crack tip path at the level of the crack tips, and vertical edge path by the end of the geometry.

7.7.1 Single Hole Geometry

The first trials to simulate the crack propagation were done with a geometry that contains one hole. The hole was at the middle of a 20mm by 4m geometry. Because of the narrow layer dealt with, the displacement of the geometry in x-direction was very high. This means the wave will smash the first layer of surrounding rocks. Also, it is found that the stresses are more concentrated at the corners of perforating hole than at the assumed crack tip at the centre of the hole base. This indicated that the cracks will propagate from corners at an angle of 45^o. All of that led to work on a multi-hole geometry with ten successive holes.

7.7.2 Multi-Holes Geometry

This geometry consists of ten successive holes, the distance between the first/last hole and the edge of the geometry is 5mm, and the distance between any two adjacent holes is 10mm. The displacement in the geometry results from the deformation due to the exerted pressure wave pulse, the Von Mises stress, and the stress intensity factor for the three magnitudes of pressure found in chapter five.

7.7.2.1 Displacement

Figures 7.9 to 7.11 show the displacement in the x-direction for the three cases of applied pressure. The displacement increases with the increase of exerted pressure wave value. The increase in displacement increases the probability of rock crushing. Depending on the porosity in the shale formation, the displacement decays away from the surface affected by the wave. The deeper the crushed layer is, the more gas is allowed to flow out and the more likely to form cracks. In addition to the possibility of taking advantage of the produced fine particles as plugs to keep the cracks open.

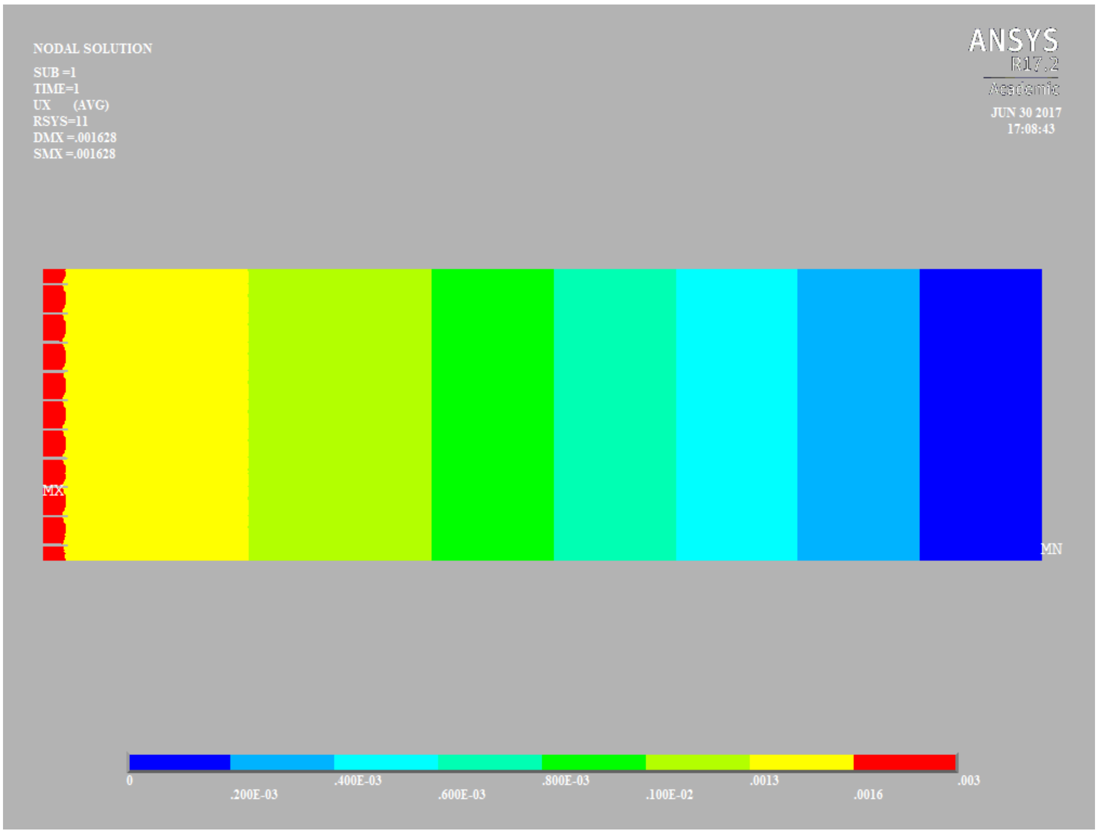

Figure 7.9 Displacement in the x-direction at p=50bar.

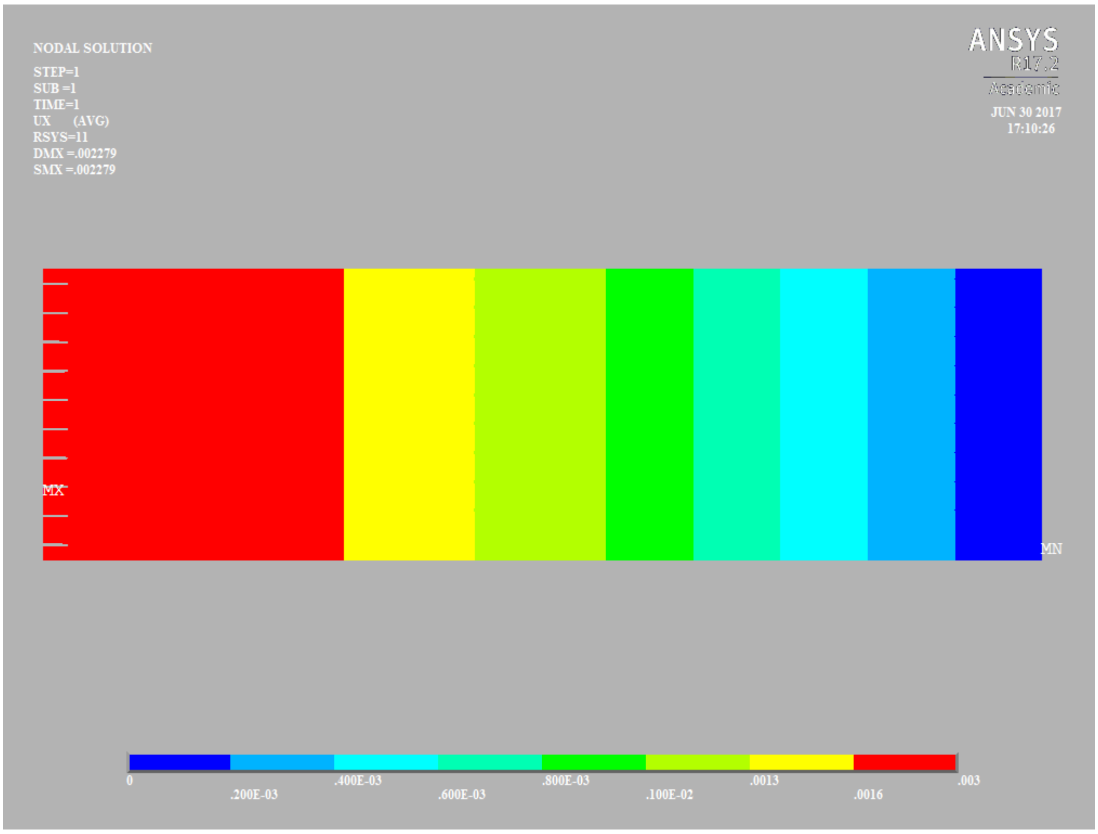

Figure 7.10 Displacement in the x-direction at p=70bar.

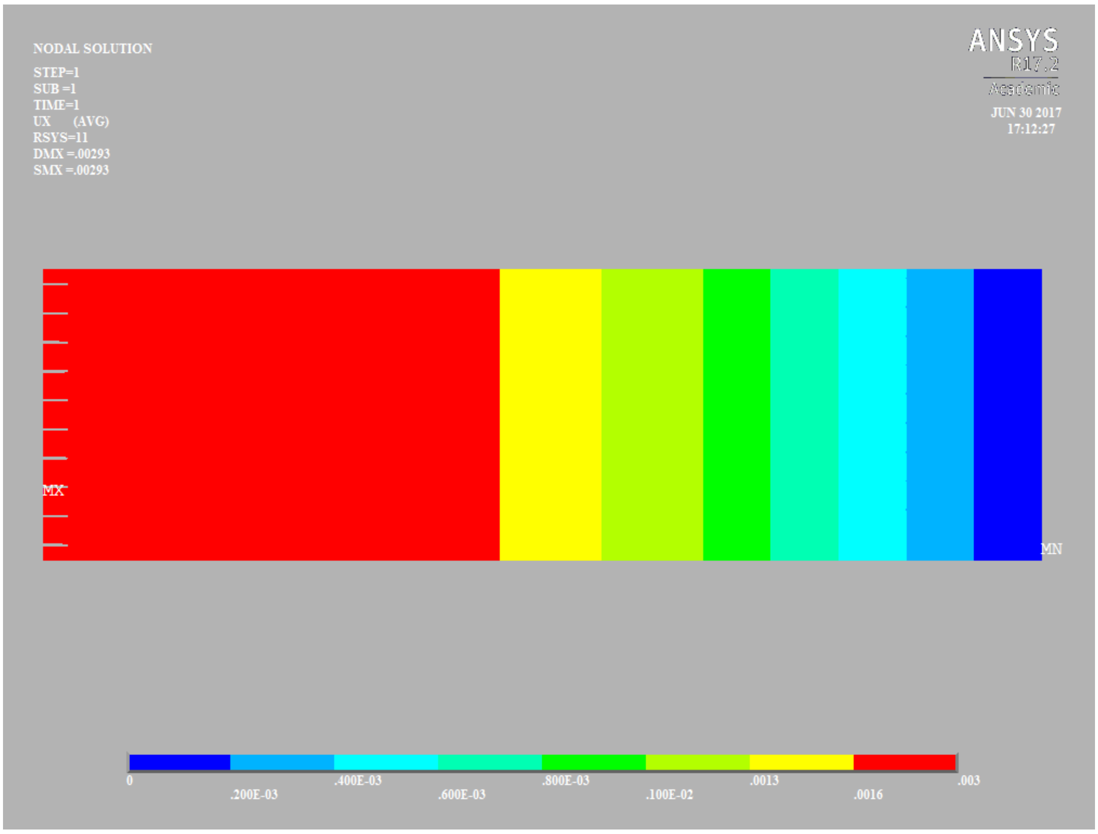

Figure 7.11 Displacement in the x-direction at p=90bar.

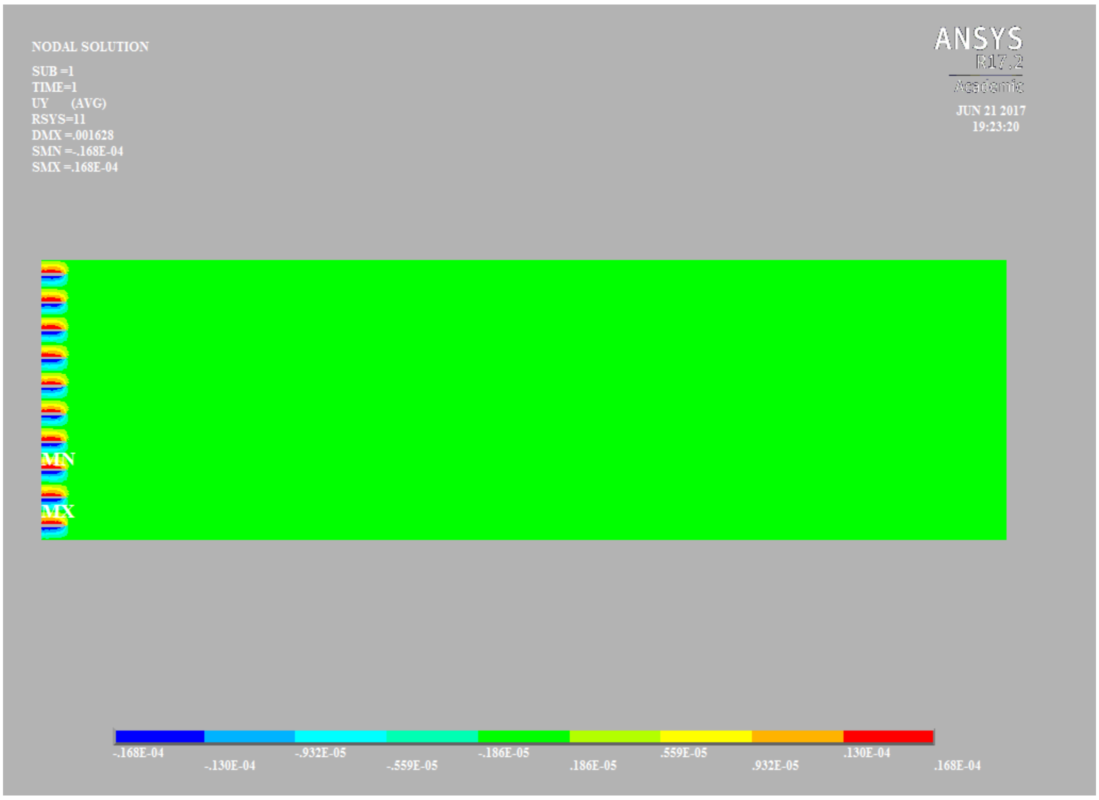

Figure 7.12 Displacement in the y-direction at p=90bar.

The displacement in the y-direction, shown in figure 7.12, is only 1% of the displacement in the x-direction, and its effect is confined to a narrow area located at the top of the perforating hole. Therefore, the y-direction displacement can be neglected.

7.7.2.2 Von Mises Stresses

One of the most commonly used criteria for elasticity is the Von Mises criterion. As it was mentioned previously, a material can fail despite the tensile strength reaches the yield point. Figures 7.13 to 7.15 show the Von Mises stress for the three cases of applied pressure. It is found that the area at the corners of perforating hole is highly influenced by the exerted load. On the other hand, the region slightly after the crack tip area is susceptible to compression stresses. As the shale rock is a layered material, it is assumed that the cracks will eventually propagate transversely, parallel to bedding [123]. Thus, it is believed that the cracks are propagating in the area between holes.

The Von Mises stress contours, shown in figures 7.13 to 7.15, show that the maximum equivalent stress concentrated at the corners are moving up and down away from the hole, to meet the stresses formed due to the exerted load on the adjacent hole in the area between the two holes.

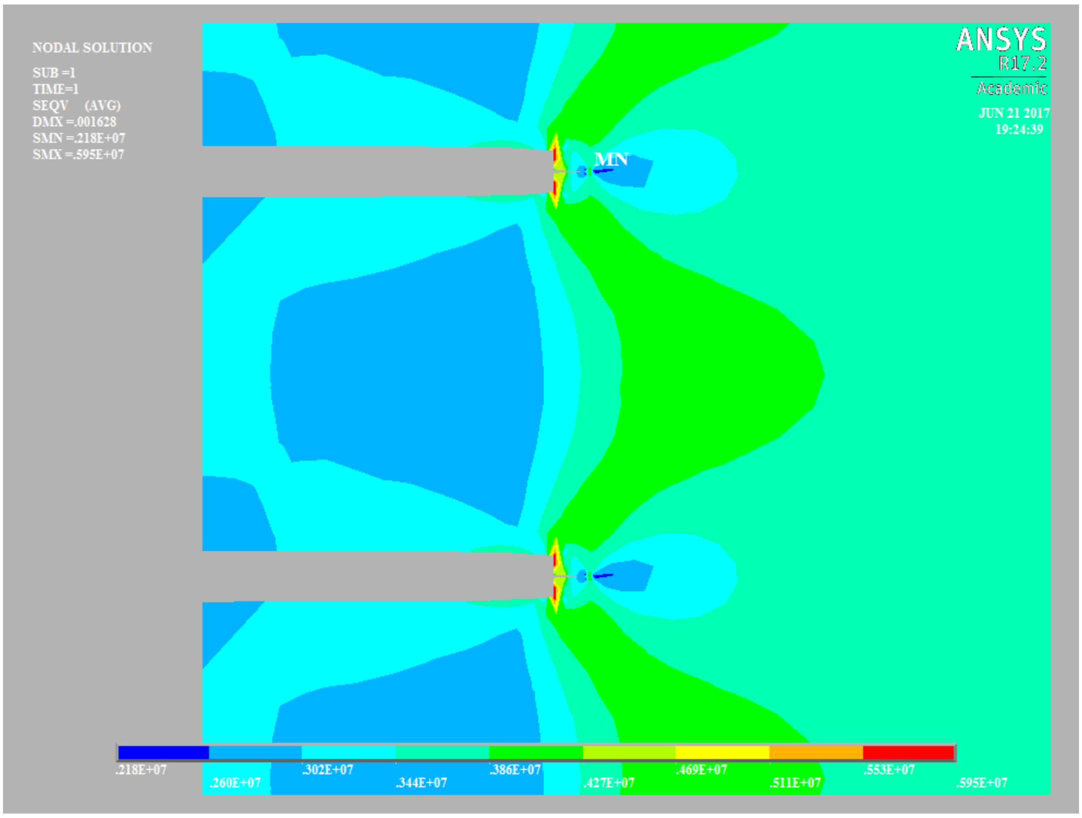

Figure 7.13 Von Mises stress at p=50bar.

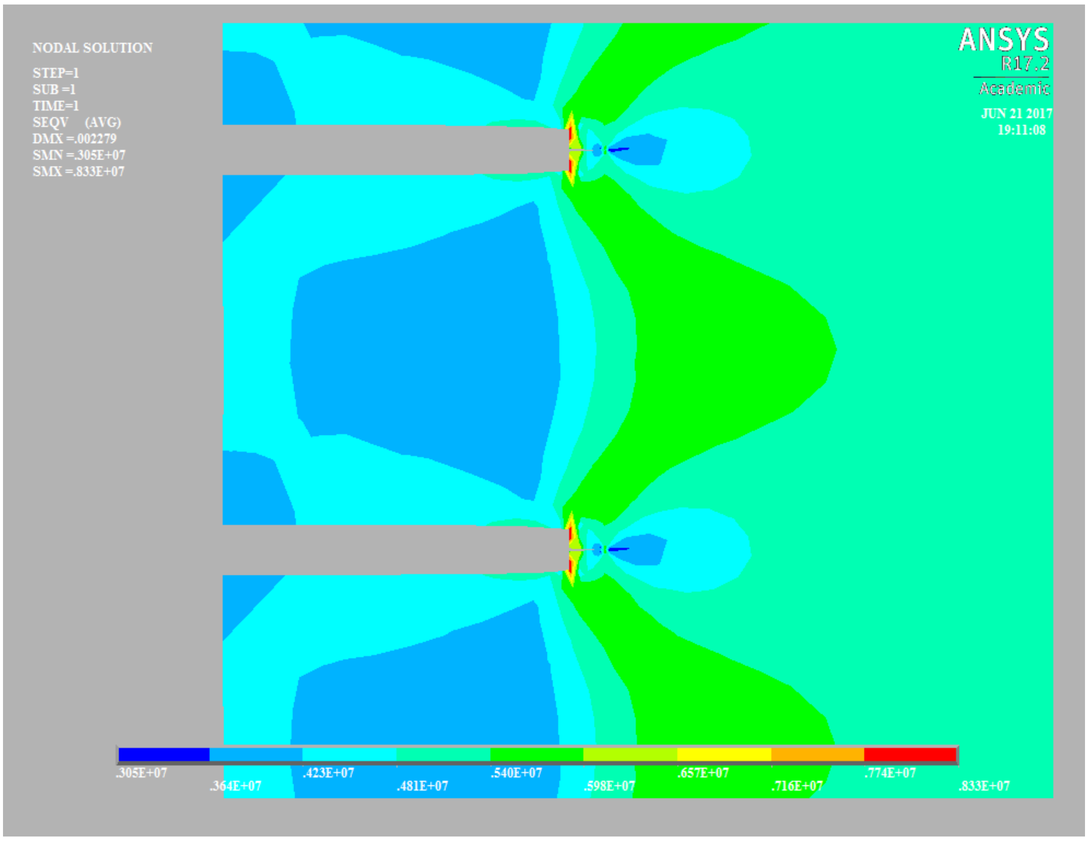

Figure 7.14 Von Mises stress at p=70bar.

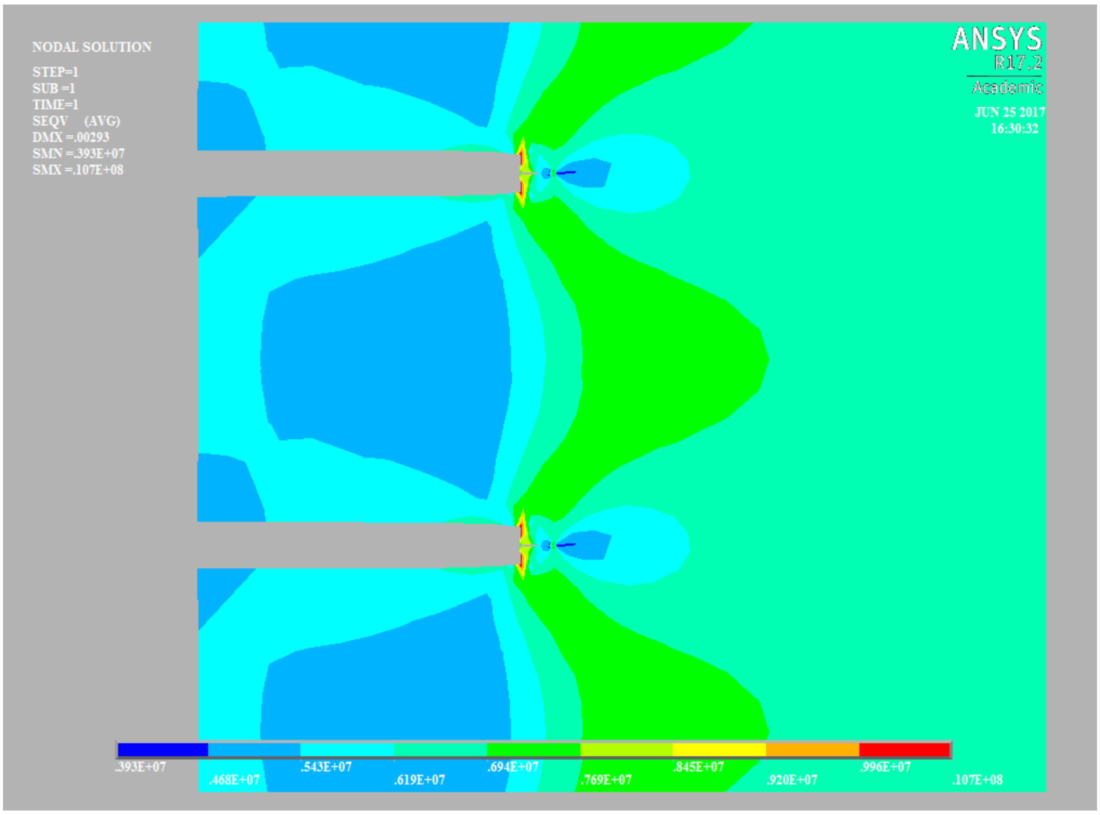

Figure 7.15 Von Mises stress at p=90bar.

7.7.2.3 Stress Intensity Factor

Stress intensity factor calculations are carried out under the three cases of pressure to examine the likelihood of the pre-crack to propagate. As the model was built in 2-dimensional system, mode III, tearing mode, is neglected. Also, mode II, shearing mode, is unlikely to occur due to the bedding nature of the rocks. Therefore, only mode I, opening mode, of stress intensity factors were presented in this part of the study. Stress is a quantity that is proportional to the forces causing a deformation, and stress intensity factor is directly proportional to the external forces applied. Hence, their behaviour was similar to some extent.

Figures 7.16 to 7.18 are the illustrative contours for stress intensity factors at the area surrounding the pre-crack for the three cases of applied pressure waves. Again, the maximum values of SIF were close to the perforating hole corners and moving in an inclined angle away from them. The contours indicate, once again, that the area between two holes from the crack tip level and away is more likely to grow cracks.

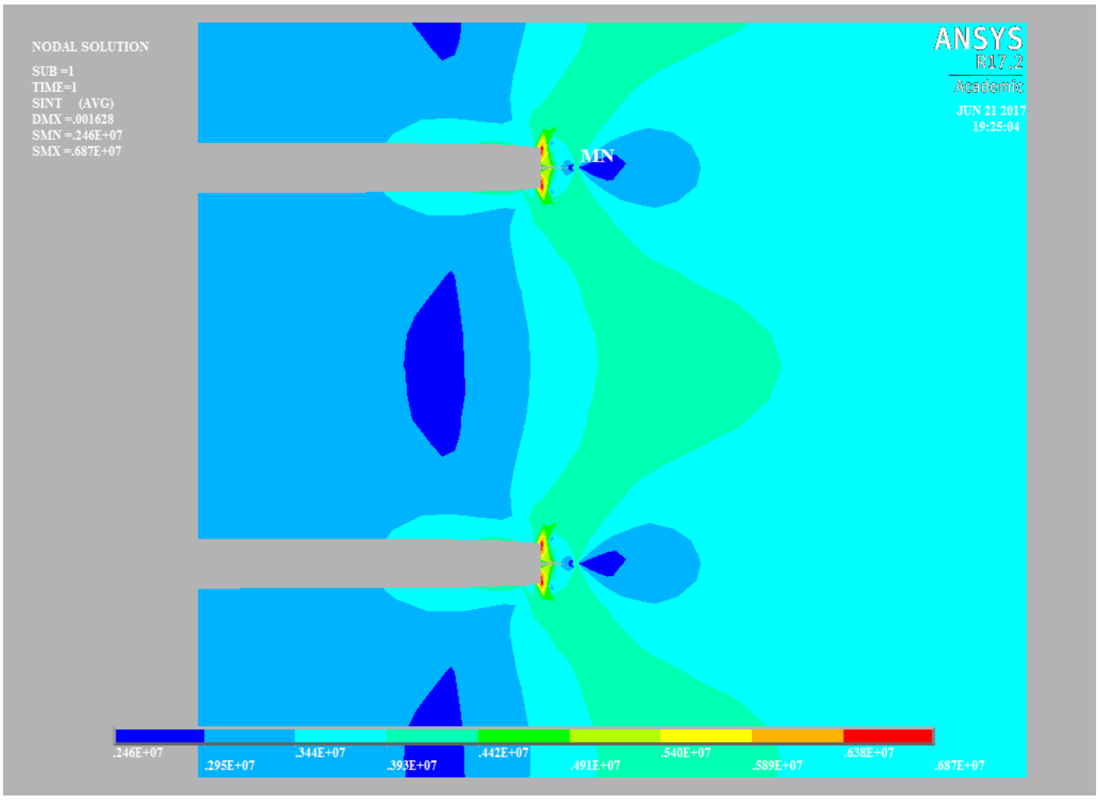

Figure 7.16 Stress intensity factor at p=50bar.

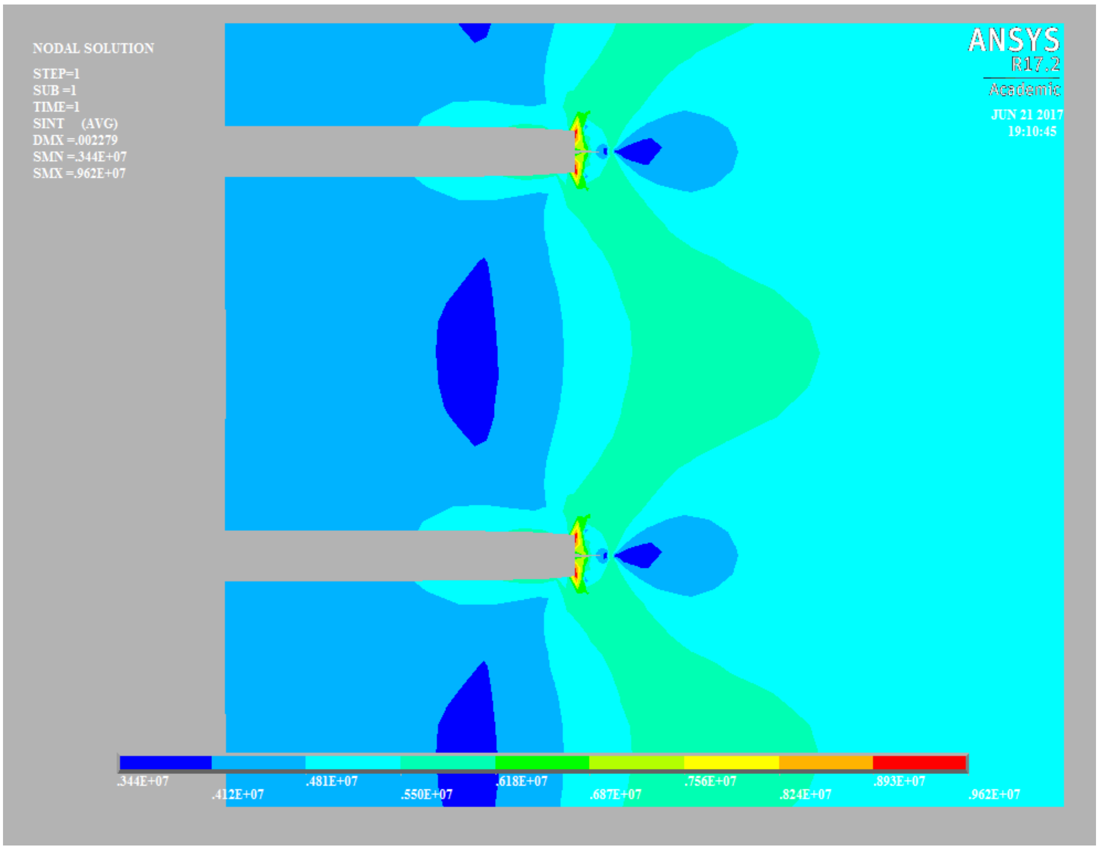

Figure 7.17 Stress intensity factor at p=70bar.

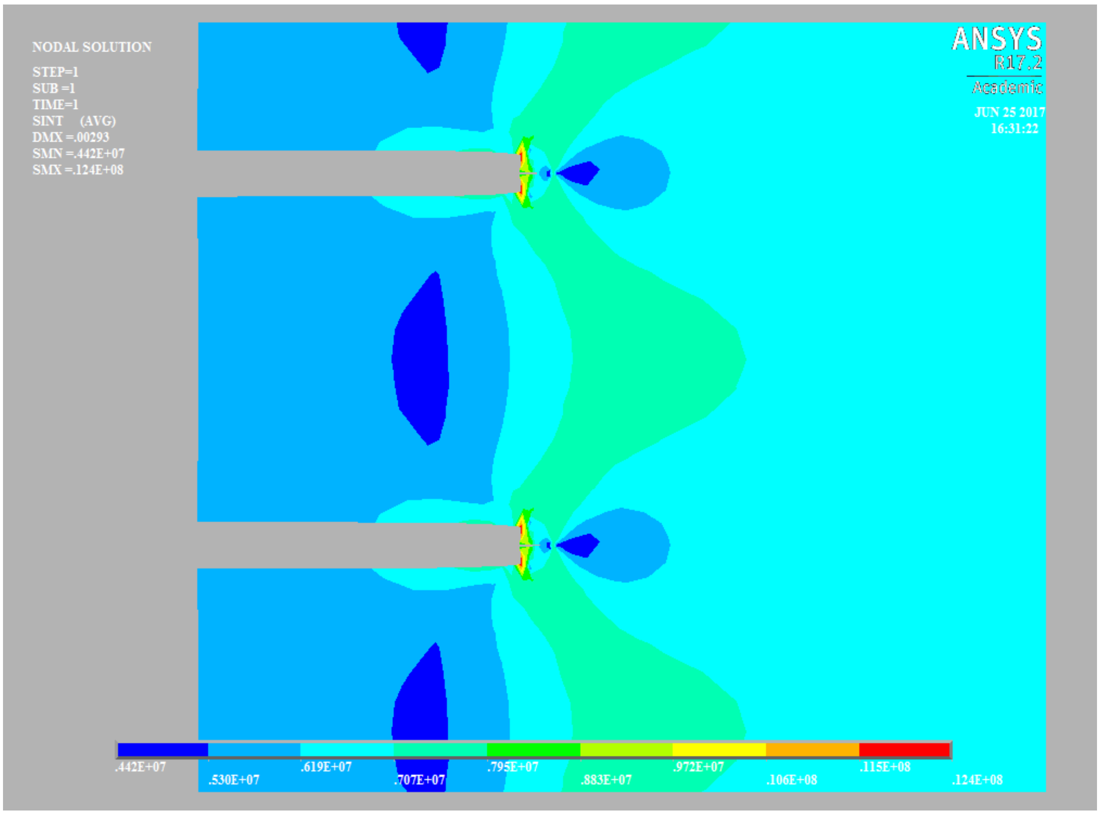

Figure 7.18 Stress intensity factor at p=90bar.

7.7.3 Results Along Paths

In order to compare among the three cases of applied pressure, stress intensity factors and Von Mises stress are measured along the four paths mentioned previously. The results are depicted with respect to the distance along the path to compare them with the fracture toughness and tensile strength of shale rock.

For all chosen paths, the results showed that the stress intensity factor is much higher than the fracture toughness of the material. This satisfies the linear elastic fracture mechanics (LEFM) theory threshold of crack growth for brittle materials, equation 2.16 [118], [122]. However, Von Mises stresses were found to exceed the shale rock tensile strength only when the exerted pressure is 70bar and 90bar. Yet, this is only achieved from a certain distance from the beginning of geometry, which ascertained the Von Mises stress distribution shown in figures 7.13 to 7.15.

7.7.3.1 Horizontal Crack Tip Path

This path is starting from the crack tip and ends at the other end of the geometry. The Von Mises stress and stress intensity factor are shown in figures 7.19 and 7.20, respectively. The Von Mises stress is found to be very high at the crack tip, then it decreases sharply due to the compression stresses, produced as a result of exerted load, in the vicinity of the crack tip. As a consequence, the SIF was high at the crack tip and low in the area around it. The stress gradually increases as the path moves away from the crack tip until it stabilises.

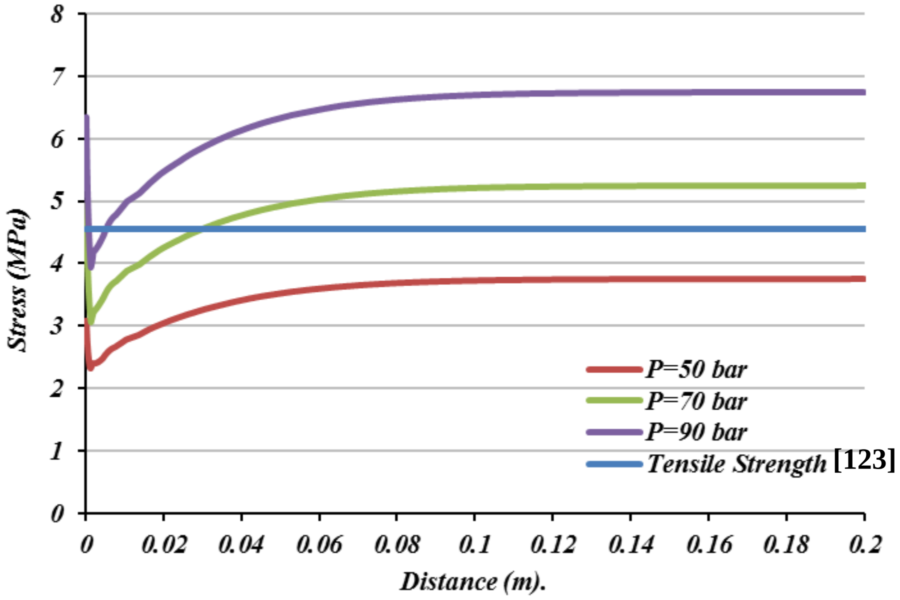

Figure 7.19 Von Mises stress for horizontal crack tip path.

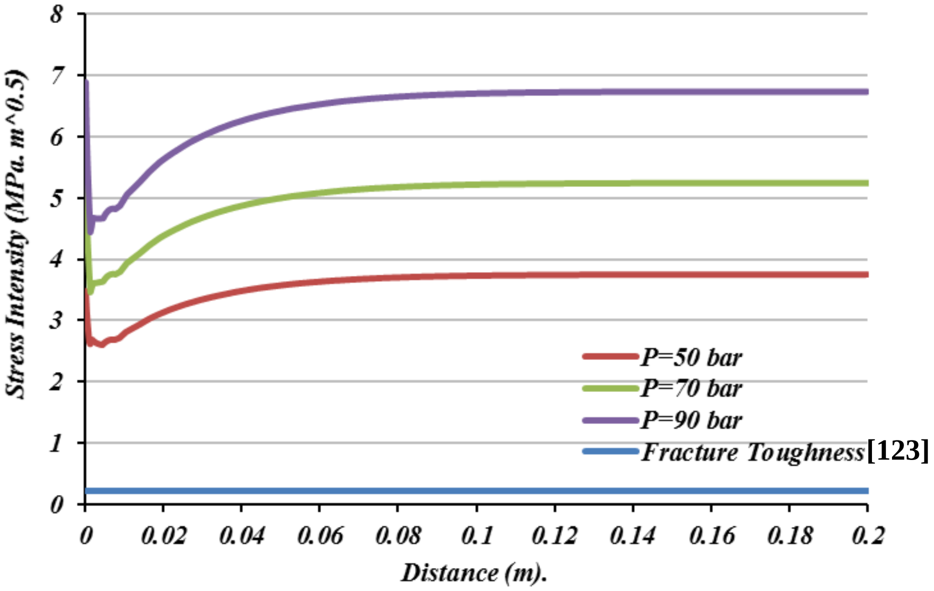

Figure 7.20 Stress intensity factor for horizontal crack tip path.

7.7.3.2 Horizontal Edge Path

This path starts from the left edge of the geometry and ends with the right one. The Von Mises stress and stress intensity factor are shown in figures 7.21 and 7.22, respectively. The stress decreases along the region between two holes until it reaches its minimum before the hole base. The equivalent stress starts to increase along the x-axis until it hits its maximum at x=0.14m, to face a slight drop followed by a uniform value along the remaining distance. Results demonstrated that the stresses varied at the area around the pre-crack. Thus, it is possible to predict the crack propagation with pressure pulse wave applied. The SIFs pass through the same distribution as stresses, the only difference was a sharper decline at the hole base area before a further increase.

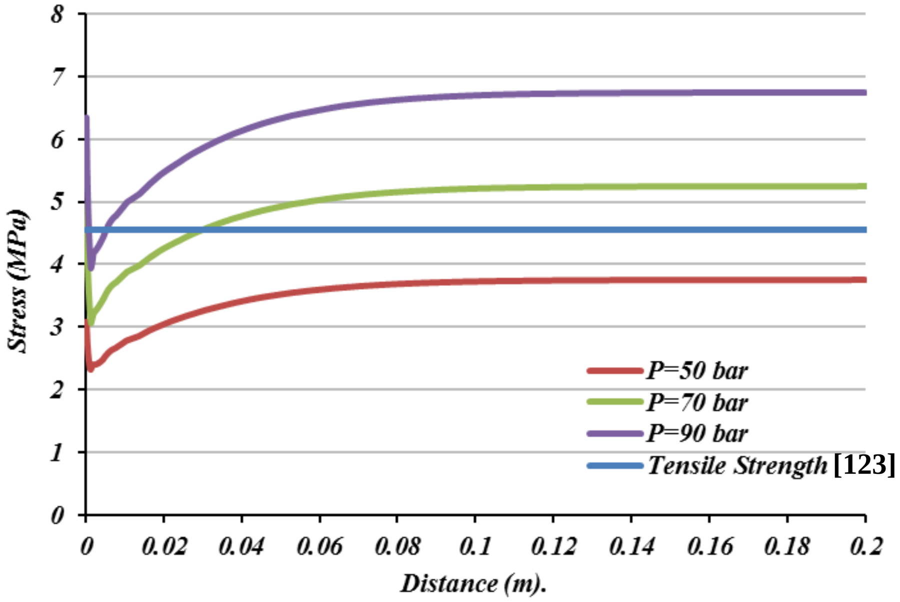

Figure 7.21 Von Mises stress for a horizontal edge path.

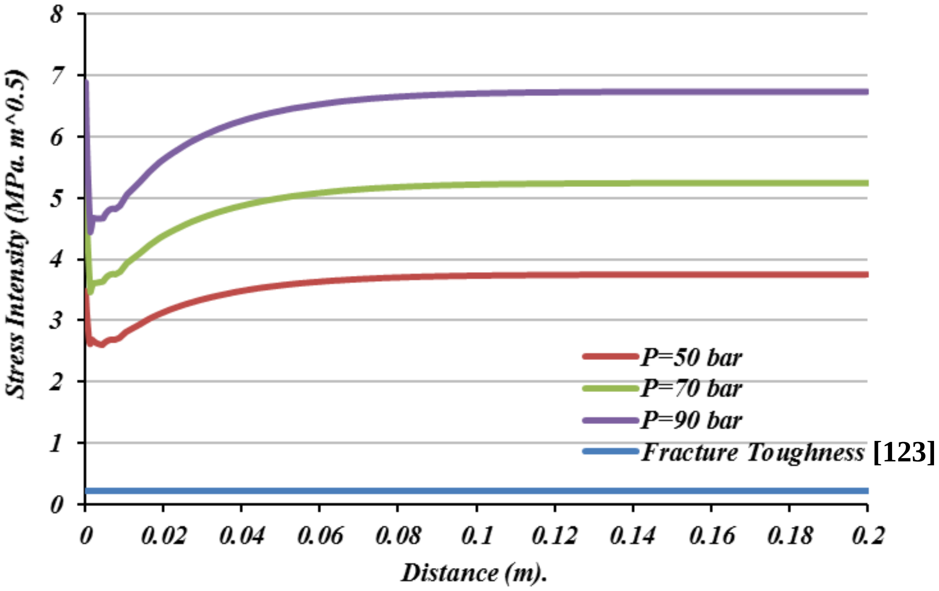

Figure 7.22 Stress intensity factor for a horizontal edge path.

7.7.3.3 Vertical Crack Tip Path

To predict the likelihood of propagation in the assumed pre-crack, a vertical path along the perforating base passing through the crack tips is taken into account. As it was stated above, the Von Mises stress yield for two cases of applied pressure, 70bar and 90bar, have exceeded the tensile strength, as illustrated in figure 7.23. Results showed that the stress acts symmetrically on both sides of the crack, which confirms that the crack propagates at an angle of 45°. The stress decreases immediately above/beneath the crack tip, followed by a small less sharp increase and lesser decrease. The stress then increases gradually until the mid-distance between two consecutive holes. The acuteness of fluctuations rises with the increases in applied pressure. The SIF, shown in figure 7.24, behaves in the same manner of stress with less sharpness.

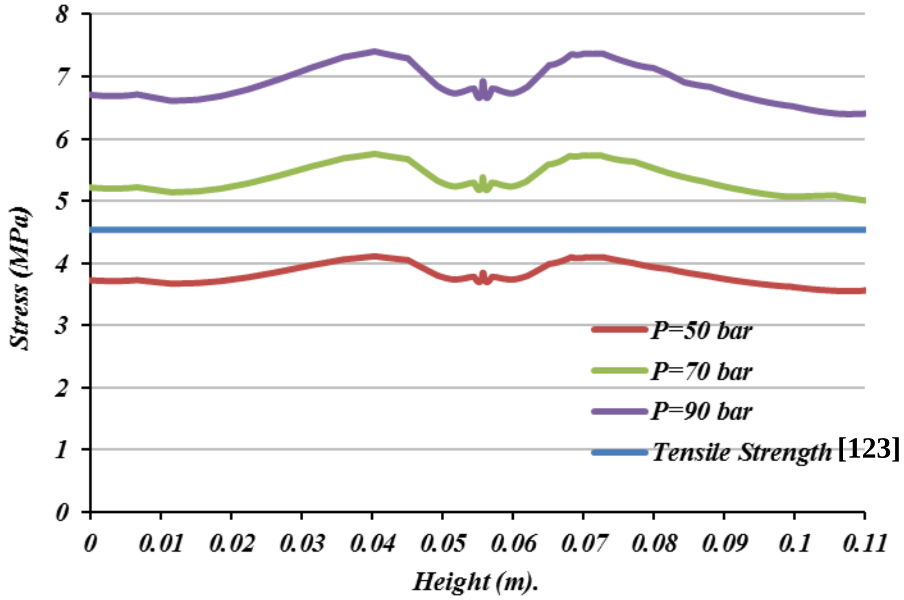

Figure 7.23 Von Mises stress for vertical crack tip path.

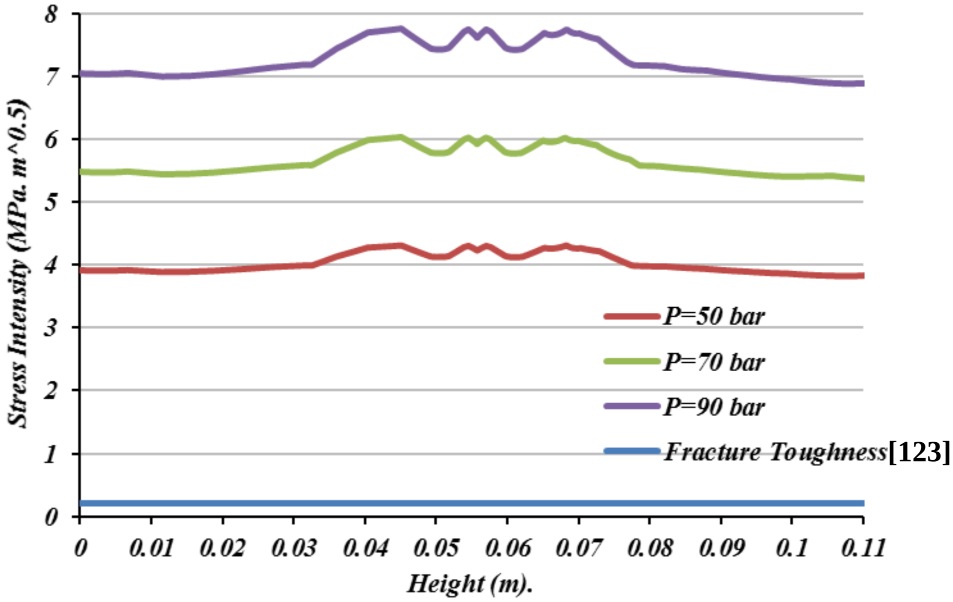

Figure 7.24 Stress intensity factor for vertical crack tip path.

7.7.3.4 Vertical Edge Path

The other vertical path was at the right end of the geometry, at about 3.90m from the crack tip. On this path, figures 7.25 and 7.26, no palpable change in stresses or SIF is found, which clarify the influence of crack on stress distribution.

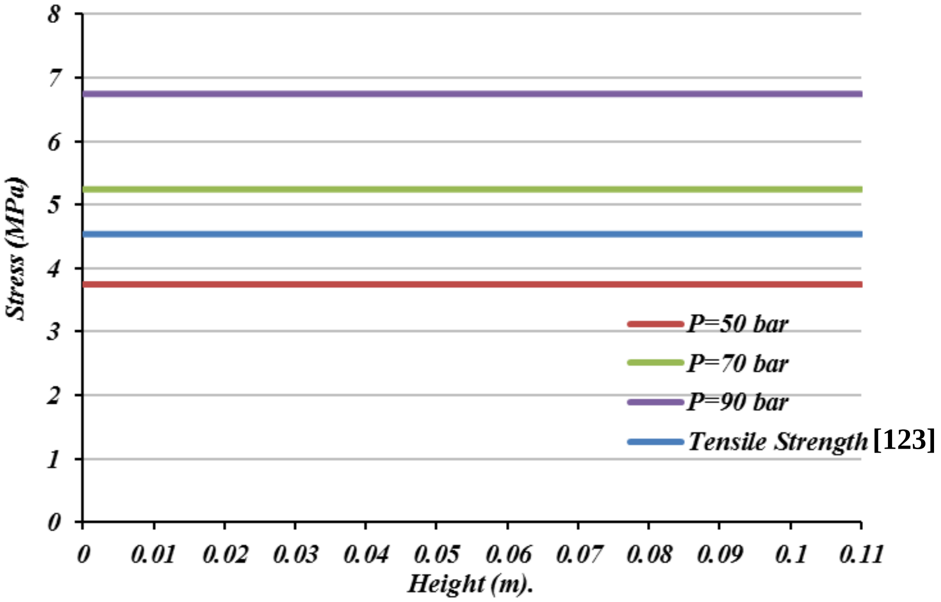

Figure 7.25 Von Mises stress for a vertical edge path.

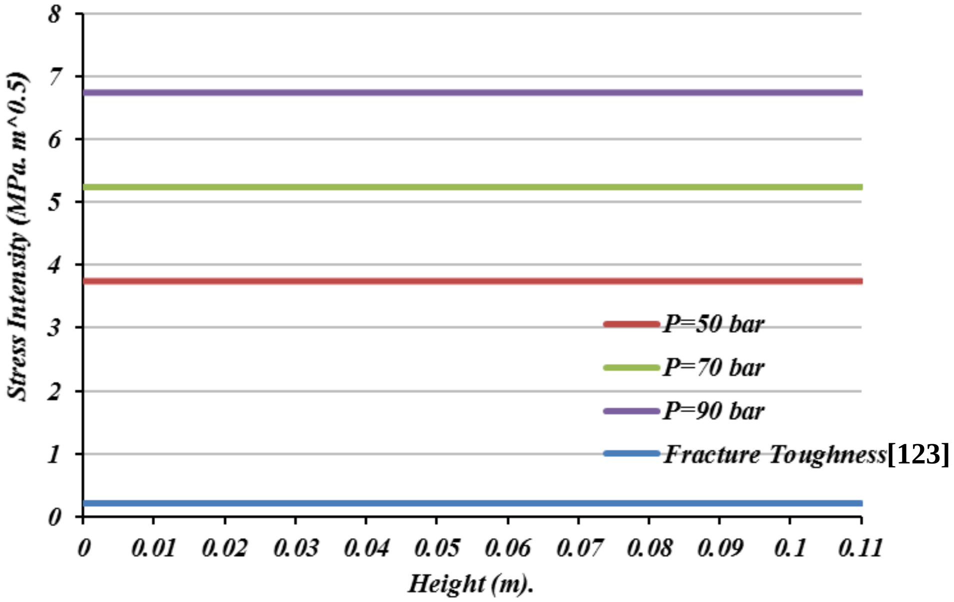

Figure 7.26 Stress intensity factor for a vertical edge path.

7.8 Conclusions

The simulation results show that the crack propagation model behaves reasonable and simulations with this model show promising results for two cases of pressure pulse waves obtained from deflagration to detonation transition simulations. Results demonstrated that stresses are concentrated at perforating hole base corners rather than the centre of it. Although it is impossible to predict the crack propagation angle, stress illustrative contour and stress distribution along the path vertical to the assumed crack tip showed that there is a high probability that the crack will propagate at an angle of 45°. However, it is believed that the orientation of the bedding will force the crack to propagate transversely. Figure 7.27 shows the prospective crack propagation path.

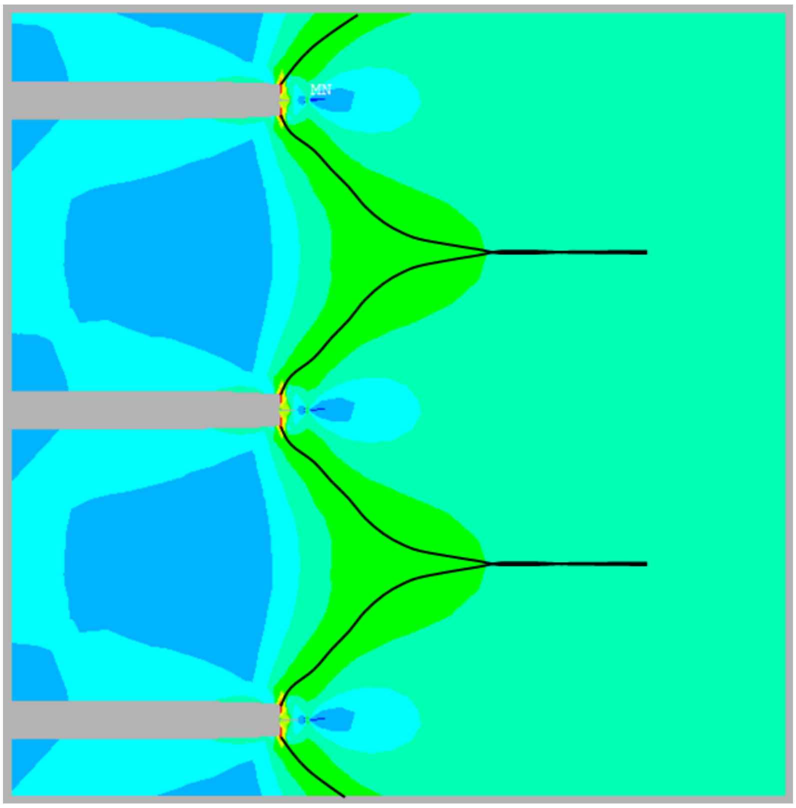

Figure 7.27 Prospective crack propagation path.

The stress intensity factor was found to satisfy the LEFM theory threshold of crack propagation for brittle material. This means that the likelihood of crack propagation is very high everywhere in the simulated geometry for all the three cases of applied loads. Also, results showed the clear influence of the proposed pre-crack on the stress and SIF. So that no changes were observed in stress or SIF along the vertical edge path.

7.9 Summary

ANSYS Parametric Design Language was used to find the effect of pressure pulse wave produced by the detonation tube simulated in chapter five. A 2-dimentional geometry of 0.11m ×4m with shale rock properties obtained from literature was used.

Ten perforating holes were assumed to create pre-cracks at the base of the hole. Three different pressure (50, 70, 90) bar were applied on the geometry to calculate the Von Mises stress and stress intensity factor all over the geometry. Also, four paths, two horizontals and two verticals, were used to investigate the stresses and SIFs behaviour along them.

Results showed that there is a high probability for crack to propagates as a result of applied load. The SIF was higher than the critical fracture toughness everywhere over the geometry for all the applied load cases. However, only two cases of pressure achieved equivalent stress as higher than the tensile strength of shale rock. One of the highest challenges in crack propagation studies is the direction that the crack will take. As this work is dealing with a natural rock formation, two factors will highly influence crack direction. The first is the orientation of the bedding and the second is the natural cracks that already exist in the formation. The stress and SIF distribution demonstrated that the crack more likely will propagate at an angle of 45°, which indicates there is a high chance that cracks from adjacent holes will intersect and take the same path.

CHAPTER EIGHT

General Discussions

8.1 The Importance of Shale Gas

Europe is the third largest energy consumer in the world, it is heavily dependent on imported natural gas. The three European Commission goals, economic competitiveness, security of supply and sustainability, are only applicable in case Europe produced its own fossil fuel. Shale gas is one of the scenarios that would decrease Europe dependence on imported gas. Although shale gas production is unlikely to give the energy security desired for the whole Europe, it will make a difference for the communities that will adopt it. In the light of the UK’s decreasing energy security due to depleting North Sea reserves and a want for energy dependence, the procurement of shale gas is becoming a critical issue.

The importance of shale gas extraction lies in two main topics, economic and environmental. The domestic shale gas production has two economic impacts on society, direct by reducing dependence on gas imports and indirect by creating employment for the local work force as well as its impact on energy market. The environmental aspect is that the use of natural gas together with or replacing of other fossil fuel lead to a reducing of harmful pollutant emissions.

However, the current highly risks recovery technique, hydraulic fracturing, led to explore for further techniques to recover shale. This has led engineers to design and produce new shale recovery techniques which are Non-Aqueous in their nature, reducing the overall environmental impact.

8.2 Proposed Appliance

The idea of the system is to use pulse detonation for the increase of pressure at variable frequencies in order to crack shale rock for gas recovery. The system is developed from the Explosion/Propellant Systems so that it is capable of improving the control of pressure wave characteristics, frequency, amplitude and location. The idea was to produce an extensive high-pressure wave at the base of the well bore using detonation. This technique might overcome both small distance fracturing for fracturing with dynamics loading and the environmental disadvantages of fracking, which could allow the propagation of longer localised cracks with higher extraction rates. Shale gas from the well will be used as the main fuel in combination with pure oxygen fed from the surface.

Deflagration to detonation transition involves initiating a deflagration, the flame then accelerates due to turbulence. Detonation phenomena is influenced by a number of factors, including the equivalence fuel air ratio, the diameter and length of the confinement tube and the presence of obstacles. In order to reduce the size of the system, detonation tubes would be equipped with specially shaped obstacles used to improve detonation, whilst a multiple ignition system might provide higher energy to the mixture to reduce the length of the transition process, topic left for future work. Experiments are held in a 21.2mm inner diameter seamless circular stainless-steel pipe with 1500mm length to achieve the deflagration to detonation transition.

The hazard and operability (HAZOP) study performed for initial bests divided the experimental rig into four parts. The first part consists of pipe lines delivering different fuel gases to the second part, a mixing chamber. Because of its violent reaction nature, oxygen will be delivered to the third part immediately, which is the main body where detonation is generated. The fourth part comprises measurement instruments and an exhaust tank. The detonation tube is operated in single shot mode.

To predict the viability of shale gas to detonate and thermophysical properties of detonated shale gas, which were the guide in choosing the detonation tube specifications, two numerical codes were used, GASEQ and CHEMKIN-Pro. Another software, OpenFOAM, was used to be the guide for the best obstacles configuration which could reduce the deflagration to detonation distance and increase the produced pressure wave.

8.3 Shale Gas Viability for Detonation

The three shale gas composition suggested by Stamford et al. [116] are used to numerically calculate the ability of shale gas to detonate. Pure oxygen is used to increase the chances of detonation and to increase the produced pressure pulse. The initial pressure and temperature are assumed to be 101.325bar and 300K respectively.

Using pure oxygen as oxidiser facilitated all the three shale gas scenarios detonation. Blends have exceeded the detonation speed threshold, which is 2300m/s as stated by literatures [93], [148], over fuel volume ratios ranging between 30% to 50%. Products dissociation associated with the use of pure oxygen led to shift the maximum detonation velocity to the rich side, achieving it at a fuel concentration of 47%.

Both GASEQ and CHEMKIN-Pro codes show similar pressure behaviour and the values correspond well. However, the higher detailed combustion reaction mechanism used with CHEMKIN-Pro has caused the pressure values to rise up to 5% higher than the corresponding calculated using GASEQ. Again, pure oxygen and the increase of hydrogen concentration in product species led to shift the maximum pressure to the rich side. As the off-stoichiometric mixtures burn cooler than stoichiometric mixtures, this would be an advantage as it makes system cooling easier. In addition to the ease of detonating oxyfuel mixtures, the presence of pure oxygen will increase the product pressure by about 50% at the maximum products pressure.

8.4 Viability Enhancement

It has been shown in many experiments that in smooth channels without obstacles only turbulent deflagration regimes can be achieved. The presence of obstacles in pipes containing moving flames exerts a strong influence on the flame propagation through causing rapid flame acceleration and increase the turbulence. Turbulence will increase the surface area of the flame and the transport of local mass and energy which will increase the local burning rate. Finally, a higher flow velocity in the unburned gas will trigger detonation.

A two-dimensional CFD simulations of the deflagration to detonation transition at stoichiometric conditions for hydrogen/air mixture using OpenFOAM toolbox were used to examine the obstacle geometry effect on deflagration to detonation transition and produced pressure waves. Hydrogen/air was used to reduce computational time while understanding the effects of different obstacles. The shape and layout of obstacles were found to have a significant effect on flame acceleration, and subsequent detonation propagation. The interaction of transverse pressure waves generated at the obstructions govern the propagation mechanism. The transverse waves, and its frequency appears to play a pivotal role in supporting the detonation wave.

Three kinds of obstacles were used here to increase the flame turbulence, rectangular, semi-circular and triangular cross-sections. Nine obstacles distributed along the tube at equal distance apart. The blockage ratio and location of obstacles were kept constant for every configuration. The run-up distance required for deflagration to transform into detonation and the produced pressure pulse were the two major features being explored to be enhanced here.

8.4.1 DDT Distance

The DDT distance, also known as predetonation distance, is the distance required for deflagration to transform into detonation. It is influenced by several factors, but the most dominant one is turbulence. The dimensions and shape of the obstacle surface have influenced the turbulence as well as the strength and shape of reflected waves.

Detonation has been achieved in all the three configurations, the difference was where and when it was triggered. The shortest DDT distances were achieved with the triangular obstacles, at 77% of total length of the tube. Yet, the pressure accomplished was the least among the three configurations, and it was reached by the end of the tube. For the rectangular obstacles, detonation was achieved at 79% of tube total length. The maximum pressure with these obstacles was achieved at the same time and place. Finally, detonation triggered almost by the end of tube, i.e. 95% of total length, showed the highest pressure among the three configurations.

The degree of induced recirculation produced by increasing drag due to sharp edges, in addition to the separation point and its effect on the induced vortex behind the obstacle were the main motives behind velocity leap in tubes with polygon obstacles. The Rayleigh-Taylor and the Kelvin-Helmholtz instabilities decreased with the absence of sharp edges in semicircular obstacles, in addition to the shorter recirculation zone prevented rapid flame speed development. Thus, detonation necessitated longer time and distance to be triggered with those configurations.

8.4.2 Pressure Pulse Wave

The semicircular obstacles recorded the highest pressure among the three configurations. The merge between progressive development of velocity and pressure along the tube and the consolidated reflected shocks by the end of tube thrusted the pressure at the exit. The absence of sharp edges reduced the induced vortex behind the obstacle which in turn reduced the turbulence and caused a moderate growth of flame propagation rate.

Although the pressure accomplished with rectangular obstacles was less than the pressure accomplished with semicircular obstacles, the length of tube to reach the maximum pressure was only 79% of the total length of the tube. This means the system could be shorter with rectangular obstacles. Another advantage of using rectangular obstacles is the time required to complete the combustion and reach detonation and maximum pressure. It is found that the tube with rectangular obstacles reaches the end of tube at 97% of the time required for triangular obstacles, while it is only required 85% for semicircular obstacles. On the other hand, the time required to hit maximum pressure was 95% with triangular obstacles and 89% for semicircular obstacles. This could create an opportunity to increase the pressure pulse frequency.

8.5 Shale Rocks

A very good potential of shale gas extraction has been found the region known as the Bowland-Hodder area. It is estimated that there could be 200tcf of gas hiding in the Bowland shale. Also, there is a good prospect for shale extraction in regions close to South Wales. Therefore, some works have been performed to determine the potential of shale gas production in the Dullais Valley, South of Wales. It was found through several tests using BS standard volatile analyses, Transmission Electron Microscopy and pyrolysis RockEval evaluation that the potential of extraction in this region is fair, with similar concentrations of pyrite but with low energy content compared to those resources located in the Midlands and Yorkshire.

The results of the volatile contents test showed that the shale rock samples may contain sufficient hydrocarbons for them to be source rocks. However, samples taken from South Wales region showed the lowest volatile organic contents percentage in the batch. This gave an indication of a poor/fair content of hydrocarbons in this region. The RockEval pyrolysis evaluation indicated that the amount of organic matter in the samples go from fair to very good. Yet, the samples from Dulais Valley showed the lowest content of the thermo-labile hydrocarbons (S1) and hydrocarbons from cracking of kerogen (S2). The amount of Fe in the South Wales samples is much higher than those in the Bowland-Hodder region. On the other hand, S is at the lowest level, thus showing that the extraction of the shale in this region would be less damaging in terms of acid content coming from this molecule.

In general, the tests showed that the rocks have poor potential for the production of gas, which means that this region possesses low potential for extraction. Also, the rocks seem to have higher levels of Fe. Nevertheless, the low S indicates that these are not bounded as FeS or FeS_2, and probably a cleaner extraction could take place. This is also dependent on the amount of other molecules such as gypsum, which seem higher in South Wales, thus setting non-aqueous pulse detonation techniques as a potential way to recover shale gas difficult to extract in Wales, with low S polluting potential.

8.6 Cracking Shale Rocks

In order to investigate the effect of pressure pulse generated by the detonation tube on a pre-crack generated by perforating, a 2-dimensional simulation was performed using APDL. At first, a single hole geometry was used, but results showed that the cracks are more likely to propagate at an angle of 45° at the perforating hole base. Therefore, a new ten successively holes geometry was studied.

Results showed that the layer close to the applied load will be displaced, which means that it will be smashed. The displacement decreases with the x-axis. The maximum Von Mises stresses were found to concentrate at the corners, while the region immediately after the crack tip is susceptible to compression stresses. Same behaviour was found for the stress intensity factor. According to that, it is believed that the cracks will propagate diagonally from the perforating hole base. However, the nature of the shale rocks will eventually force the cracks to propagate transversely, parallel to bedding.

The linear elastic fracture mechanics (LEFM) theory criterion of crack growth for brittle materials, which stated that crack propagates when the stress intensity factor exceeds the fracture toughness, was found to be achieved for all the applied pressure pulse waves. On the other hand, The Von Mises yield criterion, which stated that a material can fail despite none of the individual component stresses exceeded the stress threshold for plastic deformation, was found to be achieved only for two cases of the applied pressure pulse waves (70bar and 90bar).

8.7 Summary

The results of this work show the theoretical feasibility of using pulse detonation device to recover shale gas recirculate it for continuous operation. Various geometries have also shown different performance, leading to concepts that can be assumed in future work, i.e. initial triangular shape obstacles to reduce predetonation distance with circular obstacles to increase final pressure. Due to the properties of the wave, cracking will be produced with initial smashing of the rock, which leads to believe that reservoir of fair shale gas content can be exploited by these means, with an increase of porosity product of high temperature, combine with pressure for crack propagation, enabling good recovery of gas. Rocks in Wales can be potential receivers of this technology, with future research to be done on this topic.

CHAPTER NINE

Conclusions and Recommendations

9.1 Introduction

The high responsibility towards climate change and environmental improvement felt by Europe communities led to the cessation of shale gas exploitation. This was mainly because of the controversially hydraulic fracturing process (Fracking) and its influence on a great amount of water, as it will be mixed with an extensive list of manmade chemicals, and the likelihood of earthquakes and the damaging effects to the environment. All of this led to thinking of alternatives that can be considered as being environmentally friendly and improving the efficiency of creating and growing cracks in the shale formation.

The production of high-pressure waves at the base of the well bore by using pulse detonation could be a potential technique for shale gas extraction. However, most of the processes need to go from deflagration to detonation. This process basically occurs due to the intrinsic instability of flame surfaces. The presence of obstacles in the pipes causes rapid flame acceleration. Turbulence is the result of those obstacles. Turbulence, in turn, increases the local burning rate by increasing both the surface area of the flame and the transport of local mass and energy. This leads to higher flow velocity in the unburned gas. All of these actions, under appropriate conditions, will lead to detonation.

9.2 0-D & 1-D Numerical Analysis

Although a number of studies have been conducted on deflagration to detonation transition, very limited studies involved oxy-fuel cases. In this study, theoretical results, calculated by GASEQ and CHEMKIN-Pro codes, were employed to predict the detonation products behaviour over a wide range of total equivalence ratio of different shale gas compositions with pure oxygen. The aim was to work on the design of new systems capable of fracturing shale rock using these efficient processes.

Three shale gas scenarios proposed by Stamford and Azapagic [116] are used with pure oxygen to achieve the highest pressure in the detonation process. Also, hydrogen/air blends have been used for the purposes of comparison. Both codes showed good agreement with each other and with results obtained from the literature. The main findings of this work can be summarised as follows:

- The detonation velocity threshold for hydrocarbon/oxygen blend has been reached over fuel volume ratios ranging between 30% to 50%.
- The maximum pressure and velocity were achieved with a fuel volume fraction that exceeds 40% of the total hydrocarbon/oxygen mixture.
- Using pure oxygen with hydrocarbons increased the detonation velocity by about 16% more than the hydrogen/air mixture. However, both mixtures found to behave in the same manner over a volume percentage of fuel to total mixture ranging between 27% to 47%.
- Using pure oxygen made the pressure to reach its maximum on the rich side of stoichiometry. This in turn will produce less chemically reactive products which means that the mixture will burn cooler than stoichiometric mixtures.
- Finally, numerical results clearly demonstrated the possibility of detonating all the three shale gas scenarios as long as pure oxygen is used as oxidiser. Also, it was shown that the worst case, regarding the amount of methane, of shale gas composition was the best case of produced pressure, which is the main objective to be used in fracturing the shale formation.

9.3 2-D Numerical Analysis

A numerical simulation of detonation and deflagration to detonation transition using solver developed within the OpenFOAM CFD toolbox has been presented in this work. Numerical simulations have been carried out for a number of scenarios involving flame propagation and acceleration in obstructed channels. A grid size of about 0.5mm is used in these simulations. Three cross-section geometries of obstacles were used severally. In order to investigate the effect of geometry, the tube dimensions and obstacle locations and configurations kept constant.

The tube used was 1500mm length and 21.2mm inner diameter, nine obstacles were distributed evenly along the tube. The blockage ratio was maintained to be 47%. The observed deflagration to detonation transition phenomena caused by impact reflection on walls, transitions resulting from the turbulent flow between leading impulse and flame, and transitions triggered by shock-flame interaction. The following are the most important conclusion derived from this 2-dimensional numerical simulation work:

- It was impossible to achieve a deflagration to detonation transition within the tube when it is free of obstacles.

- The impact of the obstacles was explicit on the flame propagation even before their overlap, through the time required the flame to reach the first obstacle. The least time has been accomplished with the tube fitted with rectangular obstacles, which constituted 67.1% of the total residence time. This was 3% earlier than the triangular obstacles and up to 7% the semicircular one. Impact then extends along the tube so that the combustion in the tube with rectangular obstacles finished 3% earlier than the tube with triangular obstacles, but 15% earlier than the tube with semicircular obstacles.

- The presence of edges in obstacles played a pivotal role in the flame propagation and the location and time of transition. The sharp edge of triangular cross-section obstacle resulted in earlier separation for the flow behind the obstacle which influenced the induced vortex and the induced recirculation produced by increasing drag. As a result of all this, the shortest deflagration to detonation distance was achieved by the tube equipped with triangular obstacles.

- The longitudinal deformation of the flame passing through two opposite obstacle to the full tube diameter will induce turbulence resulting in two types of instability, the Rayleigh-Taylor instability and the Kelvin-Helmholtz instability. As the flame front passes the obstacle, it is deviated and folded up towards the leeward side of the obstacle to burn the fresh combustible mixture that still exists there. This will lead to flame deceleration before every obstacle and acceleration while passing through it. That was most obvious with semicircular obstacles due to its moderate acceleration along the tube.

- The detonation velocity threshold was exceeded by the end of the tube fitted with semicircular obstacles for a short time before the flame decelerates to leave the tube with less velocity. Detonation is achieved earlier and for longer time and distance in the tube equipped with rectangular obstacles. Yet, flames left the tube with a velocity less than the detonation velocity threshold. Once the detonation triggered in the tube fitted with triangular obstacles, which necessitated the least distance to be achieved among the three configurations, it endured to the end of the tube with a slight drop in flame velocity.

- The curvature surface of the semicircular obstacle and the progressive evolution of the flame along the tube, led to a dramatic increase in flame pressure when it merged with the consolidated reflected shocks by the end of the tube. Thus, the highest pressure was achieved with this configuration.

9.4 Geological Survey

As both global and domestic energy usage continue to rise so does the interest in alternative sources of fuel. For a number of years, the UK has been heavily reliant on natural gas to heat the residential sector, power industries and generate electricity. Over the recent decades gas consumption in the UK is risen quite dramatically, a trend which is set to continue. This has also met declining outputs from the North Sea, forcing most of the supplies to be sought from outside the country through either pipeline networks or LNG deliveries. This creates security of supply concerns if either of these supply routes are obstructed. It also leaves the country vulnerable to large price fluctuations. To combat this, many are looking to explore Britain's 'unconventional gas' reserves, particularly shale gas. Although shale gas in the UK is not as vast as in the USA, China or other countries, there is a considerable potential of several trillion cubic feet of the gas in the country. Being one potential candidate to fill the increasing demand of fuels in the UK, Wales has also started looking at its potential to contribute with this energetic revolution. Although some sites are mature enough at the north of Wales, those at the South are still under scrutiny. Therefore, some works performed to determine the potential of shale gas production in the Dullais Valley, South of Wales, is shown here. It was found through several tests using BS standard volatile analyses, Transmission Electron Microscopy and pyrolysis RockEval evaluation that the potential of extraction in this region is fair, with similar concentrations of pyrite but with low energy content compared to those resources located in the Midlands and Yorkshire. It was found the following:

- ❖ The resources in the region are low, with rocks that show a poor potential for the production of gas. Comparison with good sources coming from Yorkshire and the Midlands gave indication of very low potential for extraction in the Dulais Valley.

- ❖ In terms of element composition, the rocks seem to have higher levels of Fe. However, the low S indicates that these are not bounded as FeS or FeS_2, and probably a cleaner extraction could take place. This is also dependent on the amount of other molecules such as gypsum, which seem higher in South Wales. It can be concluded that this region possesses low potential, and although being included in the zone of onshore licenses, the benefits of exploitation might not be high.

- ❖ However, fair content of shale could still be recovered by using non-aqueous pulse detonation techniques that could ensure longer, localised crackes at high pressure, thus increasing porosity of the rock, while low S content will result in cleaner recovery using this technique.

9.5 Crack Propagation

The influence of pressure produced by the detonation tube on the rock in shale formation were investigated. A two-dimensional study using ANSYS Parameter Design Language were performed with shale rock properties to predict the pressure pulse generated by the detonation tube on a crack tip which assumed to be created by perforating. Three different pressure (50, 70, 90)bar were applied on the geometry to calculate the Von Mises stress and stress intensity factor all over the geometry. Also, four paths, two horizontals and two verticals, were used to investigate the stresses and SIFs behaviour along them.

The following conclusions were derived:

- ❖ The stress intensity factor created by pressure pulse as a load was higher than critical fracture toughness everywhere over the geometry for all the applied load cases. This satisfies the LEFM theory of crack propagation for brittle material. This means that the rocks are frackable under these pressures.

- However, only two cases of applied pressure achieved equivalent stress higher than the tensile strength of sale rock. This means only the 70bar and 90bar will satisfy the Von Mises yield criterion for plastic deformation.
- The stress and SIF distribution demonstrated that the crack more likely to propagate at an angle of 45°, which indicates there is a high chance that cracks from adjacent holes will intersect and take the same path. Yet, two factors will highly influence crack direction. Those factors are the orientation of the bedding and the natural cracks already exist in the formation.

9.6 Recommendations for Future Work

One of the main limiting aspects of the present work was the health and safety regulations of the university. Using ***PURE OXYGEN*** to generate ***DETONATION*** imposed us to go through an extensive study for all issues that might be caused by the designed system. However, this work has indicated directions for further experimental work with flame propagation and deflagration to detonation transition in confined space. The most obvious recommendations for further work will be:

- Using the designed and assembled rig to generate detonation using shale gas composition suggested by Stamford and Azapagic [116] with the three studied obstacles geometry.
- Study the effect of ignition position and timing on the transition process. The rig is designed to contain three spark plugs at a different position along the tube.
- Investigating the interactions between a flame front and the shock waves. This includes both rarefaction and compression waves that reach the flame front from both the burnt and unburnt side. These investigations should be performed with a high-speed camera and by use of Schlieren techniques.

- Further numerical analysis using the OpenFOAM code with changing the obstacles distribution and using different obstacle geometry at the same time. For example, remove the seventh to ninth triangular obstacles and mixing between the triangular and semicircular obstacle seeking both short deflagration to detonation transition distance and achieving high pressure.

- It is recommended to continue with the research of using low sulphur, fair shale gas content rocks, as these could be the potential basins where this technology could be profitable, environmental amicable and highly efficient for shale recovery.

- Investigating the effect of produced pressure on shale rock by putting a sample of rock at the exhaust of detonation tube and do the RockEval pyrolysis to find the quantity of gases left and compare it with results were obtained from not cracked samples.

- Applying the ANSYS code to investigate the influence of multi pressure pulse waves on a row of perforating holes and find the interaction between propagating cracks for adjacent holes.

References:

[1] Jilani, “Difference Between Oil and Gas,” *DifferenceBetween.net,* 2011. [Online]. Available: http://www.differencebetween.net/science/nature/difference-between-oil-and-gas/.

[2] M. Kumar, “Difference Between Oil and Natural Gas,” *DifferenceBetween.net,* 2009. [Online]. Available: http://www.differencebetween.net/object/difference-between-oil-and-natural-gas/.

[3] Energy Outlook, “Energy Outlook 2035,” 2014.

[4] P. Clark and C. Oliver, “EU energy costs widen over trade partners,” *THE FINANCIAL TIMES LTD,* 2014. [Online]. Available: http://www.ft.com/cms/s/0/2d259852-8201-11e3-87d5-00144feab7de.html#axzz3c8O1YBuP.

[5] Energy Information Administration, “Annual Energy Review 2010,” 2010.

[6] P. Di Justo, “The Energy Prescription : Switching to Renewables,” *WIRED MAGAZINE,* no. 15.10, 2007.

[7] NYSERDA, “NEW YORK ’ S OIL AND NATURAL GAS HISTORY,” *New York’s Natural Gas and Oil Resource Endowment,* pp. 8–11, 2006.

[8] P. Stevens, “The ‘Shale Gas Revolution’ : Developments and Changes,” 2012.

[9] Eurostat, “Energy production and imports,” 2015.

[10] Pöyry and Cambridge Econometrics, “Macroeconomic effects of European shale gas production,” 2013.

[11] Shale Gas Europe, “Shale Gas and The Economy,” *Shale Gas Europe,* 2014. [Online]. Available: http://www.shalegas-europe.eu/shale-gas-explained/shale-gas-and-economics/.

[12] Union of Concerned Scientists, “The Hidden Costs of Fossil Fuels,” *Union of Concerned Scientists,* 2016. [Online]. Available: http://www.ucsusa.org/clean-energy/coal-and-other-fossil-fuels/hidden-cost-of-fossils#bf-toc-0.

[13] Natgas, “Natural Gas and the Environment,” *NaturalGas.org,* 2013. [Online]. Available: http://naturalgas.org/environment/naturalgas/.

[14] B. Nordell, “Thermal pollution causes global warming,” *Glob. Planet. Change,* vol. 38, no. 3–4, pp. 305–312, 2003.

[15] J. T. Kiehl and K. E. Trenberth, “Earth’s Annual Global Mean Energy Budget,” *Bull. Am. Meteorol. Soc.,* vol. 78, no. 2, pp. 197–208, 1997.

[16] EIA, “Monthly Energy Review (MER), April 2015,” 2015.

[17] AEA, “Climate impact of potential shale gas production in the EU,” 2012.

[18] M. W. FONG, “A demonstration of acid rain,” *Asia-Pacific Forum Sci. Learn. Teach.,* vol. 5, no. 1, pp. 1–6, 2004.

[19] NAT GEO, “Acid Rain-Effects Felt Through the Food Chain,” *National Geographic,* 2015. [Online]. Available: http://environment.nationalgeographic.com/environment/globalwarming/.

[20] M. Therrien, “Formation and Origin of Smog,” *Ministère du Développement durable, de l’Environnement et des Parcs,* 2007. [Online]. Available: www.mddelcc.gouv.qc.ca/air/info-smog/fiche-formation_en.pdf.

[21] Y. Gong, Y. Wei, J. Cheng, T. Jiang, L. Chen, and B. Xu, “Health risk assessment and personal exposure to Volatile Organic Compounds (VOCs) in metro carriages - A case study in Shanghai, China,” *Sci. Total Environ.,* vol. 574, no. 1239, pp. 1432–1438, 2016.

[22] P. Stevens, “The ‘Shale Gas Revolution’: Hype and Reality,” 2010.

[23] WINGAS GmbH, “Natural gas and electricity,” *wingas,* 2015. [Online]. Available: https://www.wingas.com/en/raw-material-natural-gas/electricity-from-natural-gas.html.

[24] J. Bergström, “NOx Reduction using Reburning with Natural Gas NOx Reduction using Reburning with Natural Gas,” 1993.

[25] http://procom.kaist.ac.kr/, “Schematic of Reburning Technology.” [Online]. Available: http://procom.kaist.ac.kr/.

[26] C. Y. LEE and S. W. BAEK, “EFFECTS OF HYBRID REBURNING/SNCR STRATEGY ON NO $_X$ /CO REDUCTION AND THERMAL CHARACTERISTICS IN OXYGEN-ENRICHED LPG FLAME,” *Combust. Sci. Technol.*, vol. 179, no. 8, pp. 1649–1666, 2007.

[27] Department the Environment/ Malaysia, “BEST AVAILABLE TECHNIQUES GUIDANCE DOCUMENT ON POWER GENERATION,” 2014.

[28] US EPA, “Combined Heat and Power Partnership Basic Information,” 2015. [Online]. Available: http://www.epa.gov/chp/basic/.

[29] COGEN Europe, “What is cogeneration?,” *COGEN Europe*, 2015. [Online]. Available: http://www.cogeneurope.eu/what-is-cogeneration_19.html.

[30] C. Rayment and S. Sherwin, “Introduction to Fuel Cell Technology,” 2003.

[31] T. Huria, “Fuel Cell-Basics.” .

[32] R. Wilson, “Which Countries Produce The Most Fossil Fuels ?,” *The Energy Collective*, 2014. [Online]. Available: http://theenergycollective.com/robertwilson190/447121/who-produces-most-fossil-fuels.

[33] IEA, “Key World Energy STATISTICS 2014,” 2014.

[34] M. A. Cañete, “Energy efficiency : the invisible powerhouse of Europe,” *European Commission*, 2015. [Online]. Available: https://ec.europa.eu/commission/2014-2019/arias-canete/blog/energy-efficiency-invisible-powerhouse-europe-0_en.

[35] D. Buchan, “Can shale gas transform Europe ’ s energy landscape ?,” 2013.

[36] Iea, “Golden Rules for a Golden Age of Gas,” 2012.

[37] Total, “A lengthy preliminary phase of subsurface exploration,” *Total*. [Online]. Available: http://www.total.com/en/energies-savoir-faire/petrole-gaz/exploration-production/secteurs-strategiques/gaz-non-conventionnels/focus-gaz-de-schiste/des-techniques-de-production-specifiques/lengthy-preliminary-phase-subsurface-exploration?�bw=kludge1�.

[38] Marcellus Shale Coalition, “Natural gas production process: Exploration,” *Marcellus Shale Coalition*, 2014. [Online]. Available: http://marcelluscoalition.org/marcellus-shale/production-processes/exploration/.

[39] Shale Industry News and Shale Information, “Process of Fracking,” *Shale Stuff*, 2014. [Online]. Available: http://shalestuff.com/education/fracking/fracking.

[40] S. Davies, “Fracking: An ethical review,” 2014.

[41] Total, “PRODUCTION TECHNIQUES,” *Total*. [Online]. Available: http://www.total.com/en/energies-savoir-faire/petrole-gaz/exploration-production/secteurs-strategiques/gaz-non-conventionnels/focus-gaz-de-schiste/des-techniques-de-production-specifiques/production-techniques?�bw=kludge1�.

[42] L. Gandossi, “An overview of hydraulic fracturing and other formation stimulation technologies for shale gas production,” 2013.

[43] Society of Petroleum Engineers, “Fracturing fluids and additives,” *PetroWiki*. SPE International, 2014.

[44] S. S. Suthersan, *Remediation Engineering: Design concepts*. 1997.

[45] A. Rogala, K. Księżniak, and J. Hupka, “Perforating systems in shale gas recovery,” *PhD Interdiscip. J.*, 2013.

[46] T. Poinsot and D. Veynante, *Theoretical and Numerical Combustion*, Second ed. Edwards, USA, 2005.

[47] A. Silde and I. Lindholm, *On Detonation Dynamics in Hydrogen-Air-Steam Mixtures : Theory and Application to Olkiluoto Reactor Building*, no. February. 2000.

[48] M. Bertheldt, “Sur la vitesse de propagation des phenomenes explosifs dans les gaz,” *\cras, Paris*, vol. Q3, p. 18, 1881.

[49] E. Mallard and H. Le Chatelier, “Sur la vitesse de propagation de l’inflamnation dans lea melange explosifs,” *\cras, Paris*, vol. 93, p. 145, 1881.

[50] **H. Bertheldt and D. Vieille, "Sur la vitesse de propagation des phenomenes explosifs dans les gaz,"** ***Comptes Rendus l'Academie des Sci.,*** **vol. 94, p. 101, 1882.**

[51] **H. Le Chatelier, "Sur le development et la propagation de l'onde explosive,"** ***\cras, Paris,*** **vol. 130, p. 1755, 1900.**

[52] **S. Kerampran, D. Desbordes, and B. Veyssière, "Propagation of a flame from the closed end of a smooth horizontal tube of variable length," in** ***Proceedings of the 18th ICDERS,*** **2001.**

[53] **C. CLANET and G. Searby, "On the 'Tulip Flame' Phenomenon,"** ***Combust. Flame,*** **vol. 105, no. 1–2, pp. 225–238, 1996.**

[54] **H. Guénoche, "Flame propagation in tubes and in closed vessels," in** ***Non-Steady Flame Propagation,*** **G. H.Markstein, Ed. Pergamon Press, 1964, pp. 107–181.**

[55] **T. Bussing and G. Pappas, "An Introduction to Pulse Detonation Engines,"** ***Aiaa 94-0263,*** **1994.**

[56] **G. D. D. Salamandra, T. V. V. Bazhenova, and I. M. M. Naboko, "Formation of detonation wave during combustion of gas in combustion tube,"** ***Symp. Combust.,*** **vol. 7, no. 1, pp. 851–855, Jan. 1958.**

[57] **H. Kim, "Numerical Simulation of Transient Pulse Detonation Combustion Engine Process in Pulse Detonation Wave Engine," The University of Texas at Arlington, 1999.**

[58] **P. E. Hamlington, A. Y. Poludnenko, and E. S. Oran, "Interactions between turbulence and flames in premixed reacting flows,"** ***Phys. Fluids,*** **vol. 23, no. 12, 2011.**

[59] **D. L. Chapman, "On the rate o f explosion in gasses,"** ***Philosophical Magazine,*** **vol. 47, pp. 90–104, 1899.**

[60] **E. Jouguet, "Sur la propagation des réactions chimiques dans les gaz [On the propagation of chemical reactions in gases],"** ***J. Mathématiques Pures Appliquées, sixiéme série,*** **vol. 60, no. 1, pp. 347–425, 1905.**

[61] **Y. B. Zeldovich, "On the theory of the propagation of detonation in gaseous systems,"** ***Z. Exsperim. Theor. Fiz,*** **vol. 20, pp. 175–182, 1950.**

[62] **J. von Neumann, "Theory o f Detonation Waves,"** ***Off. Sci. Res. Dev. USA,*** **1942.**

[63] **W. Döring, "Über den Detonationsvorgang in Gasen,"** ***Ann. Phys.,*** **vol. 435, no. 6–7, pp. 421–436, 1943.**

[64] **W. Breitung, C. Chan, S. Dorofeev, A. Eder, B. Gelfand, M. Heitsch, R. Klein, A. Malliakos, E. Shepherd, E. Studer, and P. Thibault, "Flame Acceleration and Deflagration-to-DetonationTransition in Nuclear Safety," 2000.**

[65] **H. D. NG and J. H. S. LEE, "Direct initiation of detonation with a multi-step reaction scheme,"** ***J. Fluid Mech.,*** **vol. 476, pp. 179–211, 2003.**

[66] **G. O. Thomas, "Some observations on explosion development in process pipelines and implications for the selection and testing of explosion protection devices,"** ***Process Saf. Environ. Prot.,*** **vol. 86, no. 3, pp. 153–162, 2008.**

[67] **R. Porowski and a. Teodorczyk, "Experimental study on DDT for hydrogen–methane–air mixtures in tube with obstacles,"** ***J. Loss Prev. Process Ind.,*** **vol. 26, no. 2, pp. 374–379, Mar. 2013.**

[68] **D. I. Baklanov, S. V Golovastov, L. G. Gvozdeva, A. Kaltayev, and N. B. Scherbak, "Investigation of Transition of Deflagration to Detonation in Moving Mixtures of Combustible Gases,"** ***Dyn. Explos. React. Syst.,*** **2005.**

[69] **a Petchenko, V. Bychkov, V. Akkerman, and L. Eriksson, "Flame–sound interaction in tubes with nonslip walls,"** ***Combust. Flame,*** **vol. 149, no. 4, pp. 418–434, Jun. 2007.**

[70] **G. Ciccarelli, C. Johansen, and M. Kellenberger, "High-speed flames and DDT in very rough-walled channels,"** ***Combust. Flame,*** **vol. 160, no. 1, pp. 204–211, Jan. 2013.**

[71] **T. Ogawa, V. N. Gamezo, and E. S. Oran, "Flame acceleration and transition to detonation in an array of square obstacles,"** ***J. Loss Prev. Process Ind.,*** **vol. 26, no. 2, pp. 355–362, Mar. 2013.**

[72] **S. Sha, Z. Chen, X. Jiang, and J. Han, "Numerical Investigations on Blast Wave Attenuation by Obstacles,"** ***Procedia Eng.,*** **vol. 45, pp. 453–457, 2012.**

[73] S. Sha, Z. Chen, and X. Jiang, “Influences of obstacle geometries on shock wave attenuation,” *Shock Waves,* vol. 24, no. 6, pp. 573–582, Nov. 2014.

[74] J. Kindracki, P. Wolański, and Z. Gut, “Experimental research on the rotating detonation in gaseous fuels–oxygen mixtures,” *Shock Waves,* vol. 21, no. 2, pp. 75–84, Jan. 2011.

[75] D. Bradley, “Autoignitions and detonations in engines and ducts,” *Philos. Trans. R. Soc. A Math. Phys. Eng. Sci.,* vol. 370, no. 1960, pp. 689–714, 2012.

[76] B. Zhang, H. D. Ng, and J. H. S. Lee, “Measurement of effective blast energy for direct initiation of spherical gaseous detonations from high-voltage spark discharge,” *Shock Waves,* vol. 22, no. 1, pp. 1–7, Jan. 2012.

[77] G. Taylor, “and Spherical Detonation Fronts in Explosives,” vol. 235, no. August, pp. 235–247, 1949.

[78] W. C. F. Shepherd, “The Ignition of gas mixtures by impulsive pressures,” in *Third Symposium on Combustion and Flame and Explosion Phenomena,* 1948, pp. 301–316.

[79] M. Aminallah, J. Brossard, and A. Vasiliev, “29.cylindrical detonation in methane oxygen nitrogen mixture.pdf,” *AIAA Progress in Astronautics and Aeronautics,* vol. 153. p. 203, 1993.

[80] H. Matsui and J. H. Lee, “Influence of electrode geometry and spacing on the critical energy for direct initiation of spherical gaseous detonations,” *Combust. Flame,* vol. 27, pp. 217–220, Aug. 1976.

[81] T. R. Meyer, J. L. Hoke, M. S. Brown, J. R. Gord, and F. R. Schauer, “Experimental Study of Deflagration-To-Detonation Enhancement Techniques in a H2/Air Pulsed-Detonation Engine,” *Aiaa,* vol. AIAA-2002-, pp. 1–11, 2002.

[82] R. K. Zipf, V. N. Gamezo, M. J. Sapko, W. P. Marchewka, K. M. Mohamed, E. S. Oran, D. A. Kessler, E. S. Weiss, J. D. Addis, F. A. Karnack, and D. D. Sellers, “Methane-air detonation experiments at NIOSH Lake Lynn Laboratory,” *J. Loss Prev. Process Ind.,* vol. 26, no. 2, pp. 295–301, 2013.

[83] P. Wolanski, C. W. Kauffman, M. Sichel, and J. A. Nicholls, “Detonation of methane-air mixtures,” *Symp. Combust.,* vol. 18, no. 1, pp. 1651–1660, 1981.

[84] B. Vanderstraeten, D. Tuerlinckx, J. Berghmans, S. Vliegen, E. V. t Oost, and B. Smit, “Experimental study of the pressure and temperature dependence on the upper flammability limit of methane/air mixtures,” *J. Hazard. Mater.,* vol. 56, no. 3, pp. 237–246, 1997.

[85] M. P. Moyle, R. B. Morrison, and S. W. Churchill, “Detonation characteristics of hydrogen-oxygen mixtures,” *AIChE J.,* vol. 6, no. 1, pp. 92–96, 1960.

[86] G. Thomas, G. Oakley, and R. Bambrey, “An experimental study of flame acceleration and deflagration to detonation transition in representative process piping,” *Process Saf. Environ. Prot.,* vol. 88, no. 2, pp. 75–90, 2010.

[87] F. Ettner, K. G. Vollmer, and T. Sattelmayer, “Numerical Simulation of the Deflagration-to-Detonation Transition in Inhomogeneous Mixtures,” *J. Combust.,* vol. 2014, pp. 1–15, 2014.

[88] C. Jimenez, J. Quinard, J. Grana-Otero, H. Schmidt, and G. Searby, “Unsteady response of hydrogen and methane flames to pressure waves,” *Combust. Flame,* vol. 159, no. 5, pp. 1894–1908, 2012.

[89] A. M. Khokhlov, E. S. Oran, and J. C. Wheeler, “A theory of deflagration-to-detonation transition in unconfined flames,” *Combust. Flame,* vol. 108, no. 4, pp. 503–517, 1997.

[90] E. S. Oran and V. N. Gamezo, “Origins of the deflagration-to-detonation transition in gas-phase combustion,” *Combust. Flame,* vol. 148, no. 1–2, pp. 4–47, 2007.

[91] G. Ciccarelli and S. Dorofeev, “Flame acceleration and transition to detonation in ducts,” *Prog. Energy Combust. Sci.,* vol. 34, pp. 499–550, 2008.

[92] J. E. Shepherd, “Detonation in gases,” *Proc. Combust. Inst.,* vol. 32 I, no. 1, pp. 83–98, 2009.

[93] K. Kailasanath, “Liquid-Fueled Detonations in Tubes,” *Journal of Propulsion and Power,* vol. 22, no. 6. pp. 1261–1268, Nov-2006.

[94] F. B. Cramer, “The onset of detonation in a droplet combustion field,” *Symp. Combust.*, vol. 9, no. 1, pp. 482–487, Jan. 1963.

[95] J. M. Powers, D. S. Stewart, and H. Krier, “Theory of two-phase detonation-Part I: Modeling,” *Combust. Flame*, vol. 80, no. 3–4, pp. 264–279, 1990.

[96] S. B. Dorofeev, V. P. Sidorov, M. S. Kuznetsov, I. D. Matsukov, and V. I. Alekseev, “Effect of scale on the onset of detonations,” *Shock Waves*, vol. 10, no. 2, pp. 137–149, 2000.

[97] J. E. Shepherd, “Structural Response of Piping to Internal Gas Detonation,” *J. Press. Vessel Technol.*, vol. 131, no. 3, p. 31204, 2009.

[98] A. Eder, C. Gerlach, and F. Mayinger, “Experimental Observation of Fast Deflagrations and Transition to Detonations in,” in *Symposium on Energy Engineering in the 21st Century (SEE2000)*, 2000, pp. 1296–1304.

[99] W. Rudy, R. Porowski, and A. Teodorczyk, “Propagation of hydrogen-air detonation in tube with obstacles,” *J. Power Technol.*, vol. 91, no. 3, pp. 122–129, 2011.

[100] Kirk-Othmer, “Encyclopaedia of Chemical Technology.” Wiley, New York, p. 431, 1995.

[101] a Teodorczyk, “Fast deflagrations and detonations in obstacle-filled channels,” *J. Power Technol.*, 1995.

[102] E. Dziemińska and A. K. Hayashi, “Auto-ignition and DDT driven by shock wave-Boundary layer interaction in oxyhydrogen mixture,” *Int. J. Hydrogen Energy*, vol. 38, no. 10, pp. 4185–4193, 2013.

[103] J. Alcock, L. Shirvill, and R. Cracknell, “Compilation of Existing Safety Data on Hydrogen and Comparative Fuels,” 2002.

[104] W. Liu, “Numerical Investigation into Fast Deflagration and Its Transition to Detonation in Smooth Tube,” in *Proceedings of the European Combustion Meeting*, 2015, pp. 3–8.

[105] K. Chatrathi, D. Ph, J. E. Going, B. Grandestaff, F. Corporation, S. Street, and B. Springs, “Flame Propagation i n Industrial Scale Piping,” *Process Saf. Prog.*, vol. 20, no. 4, 2001.

[106] S. Kundu, J. Zanganeh, and B. Moghtaderi, “A Review on Understanding Explosions from Methane-Air Mixture,” *J. Loss Prev. Process Ind.*, vol. 40, 2016.

[107] H. D. Ng, Y. Ju, and J. H. S. Lee, “Assessment of detonation hazards in high-pressure hydrogen storage from chemical sensitivity analysis,” *Int. J. Hydrogen Energy*, vol. 32, no. 1, pp. 93–99, 2007.

[108] M. Kaneshige and J. E. Shepherd, “Detonation Database: Explosion Dynamics Laboratory Report FM97-8,” 1997.

[109] N. S. Titova, S. A. Torokhov, I. V Chechet, O. N. Favorskii, and A. M. Starik, “Kinetic Analysis of the Mechanisms of Ignition and Combustion of Blended Fuels Comprising Hydrocarbons and Hydrogen,” in *25th ICDERS*, 2015, pp. 1–6.

[110] R. Porowski and A. Teodorczyk, “Cellular structure of detonation wave in hydrogen-methane-air mixtures,” *J. Power Technol.*, vol. 91, no. 3, pp. 130–135, 2011.

[111] B. Zhang, L. Pang, and Y. Gao, “Detonation limits in binary fuel blends of methane/hydrogen mixtures,” *Fuel*, vol. 168, pp. 27–33, 2016.

[112] E. Schultz, E. Wintenberger, and J. Shepherd, “Investigation of Deflagration to Detonation Transition for Application to Pulse Detonation Engine Ignition Systems,” *Proc. 16th JANNAF Propuls. Symp.*, vol. 1, no. c, pp. 175–202, 1999.

[113] V. N. Gamezo, R. K. Zipf, M. J. Sapko, W. P. Marchewka, K. M. Mohamed, E. S. Oran, D. A. Kessler, E. S. Weiss, J. D. Addis, F. A. Karnack, and D. D. Sellers, “Detonability of natural gas-air mixtures,” *Combust. Flame*, vol. 159, no. 2, pp. 870–881, 2012.

[114] R. K. Zipf, V. N. Gamezo, K. M. Mohamed, E. S. Oran, and D. a. Kessler, “Deflagration-to-detonation transition in natural gas–air mixtures,” *Combust. Flame*, vol. 161, no. 8, pp. 2165–2176, Aug. 2014.

[115] J. Lee, “Dynamic Parameters of Gaseous Detonations,” *Annu. Rev. Fluid Mech.*, vol. 16, no. 1, pp. 311–336, Jan. 1984.

[116] L. Stamford and A. Azapagic, “Life cycle environmental impacts of UK shale gas,” *Appl. Energy*, vol. 134, pp. 506–518, Dec. 2014.

[117] G. E. King, “Thirty Years of Gas Shale Fracturing: What Have We Learned?,” in *SPE Annual Technical Conference and Exhibition*, 2010.

[118] G. Hattori, J. Trevelyan, C. E. Augarde, W. M. Coombs, and A. C. Aplin, “Numerical Simulation of Fracking in Shale Rocks: Current State and Future Approaches,” *Arch. Comput. Methods Eng.*, vol. 44, no. March, pp. 1–37, 2016.

[119] A. A. Griffith, “The Phenomena of Rupture and Flow in Solids,” *Philosophical Transactions of the Royal Society A: Mathematical, Physical and Engineering Sciences*, vol. 221, no. 582–593. pp. 163–198, 1921.

[120] A. A. Griffith, “The Theory of Rupture,” in *Proceedings of the First International Congress for Applied Mechanics*, 1924, pp. 55–63.

[121] G. R. Irwin, “Analysis of Stresses and Strains Near the End of a Crack Traversing a Plate,” *Journal of Applied Mechanics*, vol. 24, no. September. pp. 361–364, 1957.

[122] W. D. Pilkey, *Formulas for stress, staind, and structural matrices*. 1994.

[123] M. R. Chandler, P. G. Meredith, N. Brantut, and B. R. Crawford, “Fracture toughness anisotropy in shale,” *J. Geophys. Res. B Solid Earth*, vol. 121, no. 3, pp. 1706–1729, 2016.

[124] A. Moradi, B. Tokhmechi, V. Rasouli, and M. Fatehi Marji, “A Comprehensive Numerical Study of Hydraulic Fracturing Process and Its Affecting Parameters,” *Geotech. Geol. Eng.*, vol. 35, no. 3, pp. 1035–1050, 2017.

[125] Y. J. Zeng, X. Zhang, and B. P. Zhang, “Stress redistribution in multi-stage hydraulic fracturing of horizontal wells in shales,” *Pet. Sci.*, vol. 12, no. 4, pp. 628–635, 2015.

[126] X. Zeng and Y. Wei, “Crack deflection in brittle media with heterogeneous interfaces and its application in shale fracking,” *J. Mech. Phys. Solids*, vol. 101, pp. 235–249, 2017.

[127] DSEA-DOSR, “EXPLOSIVES LEGISLATION,” in *EXPLOSIVES REGULATIONS*, Edition 4., no. 9, Intergovernmental Panel on Climate Change, Ed. Cambridge: Cambridge University Press, 2013, pp. 1–30.

[128] W. Rose, “The Application of Human Factors through the Assessment and Improvement of Behavioural Safety to Improve Safety Performance in Small to Medium Sized Enterprises the requirements of Edinburgh Napier University in the Faculty of Engineering , Computing & Cr,” Edinburgh Napier University, 2012.

[129] Mike Lihou, “Hazard & Operability Studies (HAZOP),” *Lihou Technical & Software Services*, 2015. [Online]. Available: http://www.lihoutech.com/hazop1.htm#design_intent. [Accessed: 01-Jan-2015].

[130] C. H. Bay, “Hazardous Industry Planning: Safety and HAZOP Guideline,” 2008.

[131] G. Mckay, *PROCESS SAFETY MANAGEMENT AND RISK HAZARD ANALYSIS*. 2012, pp. 0–54.

[132] Pqri, “Hazard & Operability Analysis (HAZOP),” *Risk Manag. Train. Guid.*, pp. 1–9, 2014.

[133] A. Y. Z. Au and G. W. Gould, “A structured brainstorming approach to the assessment of emergency response,” *ICHEME Symp. Ser.*, no. 141, pp. 233–245, 1997.

[134] DOE - Department of Energy, *DOE-HDBK-1100-2004 Chemical Process Hazards Analysis*. 2004.

[135] E. A. L. ROBERTS, “Improvement in method of increasing capacity of oil-wells. U.S. Patent No. 59,936,” 1866.

[136] J. S. Miller and R. T. Johanren, “FRACTURING OIL SHALE WITH EXPLOSIVES FOR IN SITU RECOVERY,” *Adv. Chem. Ser.*, vol. 151, 1976.

[137] fti Controlling Pressure & Vacuum, “Stainless Steel Tube,” 2014. [Online]. Available: www.ftipv.com.

[138] HAM-LET Adcanced Control Technology, “Compression Tube Fittings LET-LOK.” .

[139] “flashback-arrester.” [Online]. Available: http://www.flashback-arrester.com/. [Accessed: 15-Nov-2016].

[140] HAM-LET Adcanced Control Technology, “HAM-LET Valves & Fittings.” .

[141] HAM-LET Adcanced Control Technology, “THREE-PIECE BALL VALVES H-500

SERIES.” .

[142] KISTLER measure. analyze. Innonate, “Piezoelectric Pressure Sensors (IEPE),” 2015. [Online]. Available: www.kistler.com.

[143] Morely C, “Gaseq chemical equilibrium program.” 2005.

[144] S. Gordon and B. J. McBride, “Computer Program for Calculation of Complex Chemical Equilibrium Compositions Application,” *NASA RP-1311,* 1994.

[145] Reaction-Design, “CHEMKIN-Pro.” .

[146] Reaction Design, “Fuel Models for Accurate Simulation,” no. October. 2012.

[147] G. P. Smith, D. M. Golden, M. Frenklach, N. W. Moriarty, B. Eiteneer, M. Goldenberg, C. T. Bowman, R. K. Hanson, S. Song, J. William C. Gardiner, V. V. Lissianski, and Z. Qin, “GRI-MECH.” .

[148] S. Gordon and B. J. McBride, “Computer Program for Calculation of Complex Chemical Equilibrium Compositions, Rocket Performance, Incident and Reflected Shocks and Chapman-Jouguet Detonations,” *NASA Rep. SP-273,* 1971.

[149] Reaction Design, “Chemkin Theory Manual,” no. December, pp. 1–386, 2010.

[150] J. H. S. Lee and C. M. Guirao, “Gasdynamic Effects of Fast Exothermic reactions,” in *Fast Reaction in Energetic Systems,* C. Capellos and R. F. Walkers, Eds. D. Reidel Publishing Company, Dordrecht, 1981, pp. 245–313.

[151] OpenFOAM Foundation, *Open ∇FOAM User Guide Version 2.3.0,* no. February. 2014.

[152] Wikipedia, “Godunov’s scheme,” *wikipedia.* .

[153] S. M. Salim and K. C. Ong, “Performance of RANS, URANS and LES in the Prediction of Airflow and Pollutant Dispersion,” *Proc. World Congr. Eng. Comput. Sci.,* vol. II, pp. 263–274, 2013.

[154] S. B. Pope, *Turbulent Flows.* 2000.

[155] G. Iaccarino, A. Ooi, P. A. Durbin, and M. Behnia, “Reynolds averaged simulation of unsteady separated flow,” *Int. J. Heat Fluid Flow,* vol. 24, no. 2, pp. 147–156, 2003.

[156] A. Sadiki, A. Maltsev, B. Wegner, F. Flemming, A. Kempf, and J. Janicka, “Unsteady methods (URANS and LES) for simulation of combustion systems,” *Int. J. Therm. Sci.,* vol. 45, no. 8, pp. 760–773, 2006.

[157] Ansys, *Ansys fluent 12.0 Theory Guide,* no. April. 2009.

[158] A. P. Singh, V. RatnaKishore, S. Minaev, and S. Kumar, “Numerical investigations of unsteady flame propagation in stepped microtubes,” *RSC Adv.,* vol. 5, no. 122, pp. 100879–100890, 2015.

[159] B. Fan, Z. Ying, Z. Chen, and J. Ye, “Observations of flame behavior during flame-obstacle interaction,” *Process Saf. Prog.,* vol. 27, no. 1, pp. 66–71, 2008.

[160] A. Chaudhuri, A. Hadjadj, O. Sadot, and G. Ben-Dor, “Numerical study of shock-wave mitigation through matrices of solid obstacles,” *Shock Waves,* vol. 23, no. 1, pp. 91–101, 2013.

[161] Petroleum.co.uk, “Petroleum - Formation - The Chemistry of Petroleum Formation,” 2014. [Online]. Available: http://www.petroleum.co.uk/chemistry-of-petroleum-formation.

[162] H. Terrel, “British Shale Gas: more holes for Blackpool, Lancashire?,” *World Oil 234,* p. 23, 2013.

[163] I. J. Andrews, “The Carboniferous Bowland Shale gas study: geology and resource estimation,” *Br. Geol. Surv. Dep. Energy Clim. Chang. London, UK,* p. 64pp, 2013.

[164] Department of Energy and Climate Change, “Preparing for the 14th round of onshore oil and gas licences,” *Department of Energy and Climate Change,* 2013. .

[165] A. K. Varma, B. Hazra, and A. Srivastava, “Estimation of Total Organic Carbon in shales through color manifestations,” *J. Nat. Gas Sci. Eng.,* vol. 18, pp. 53–57, 2014.

[166] Y. A. A. Almashramah, “Maturity of kerogen , petroleum generation and the application of fossils and organic matter for paleotemperature measurements,” 2011.

[167] ISO 562, “Hard coal and coke -- Determination of volatile matter,” *ISO*, 2010.

[168] A. Miranda-gonzalez, “Shale Gas in Mexico : A New Frontier,” 2014.

[169] M. J. Kotarba, J. L. Clayton, D. D. Rice, and M. Wagner, “Assessment of hydrocarbon source rock potential of Polish bituminous coals and carbonaceous shales,” *Chem. Geol.*, vol. 184, no. 1–2, pp. 11–35, 2002.

[170] K. E. Peters, “Guidelines for evaluating petroleum source rock using programmed pyrolysis,” *AAPG Bull.*, vol. 70, no. 3, pp. 318–329, 1986.

[171] D. Mani, D. J. Patil, A. M. Dayal, S. Kavitha, M. Hafiz, N. Hakhoo, and G. M. Bhat, “Gas potential of Proterozoic and Phanerozoic shales from the NW Himalaya, India: Inferences from pyrolysis,” *Int. J. Coal Geol.*, vol. 128–129, pp. 81–95, 2014.

[172] L. Nuñez-Betelu and J. I. Baceta, “Basics and application of Rock-Eval/TOC pyrolysis: an example from the uppermost Paleocene/lowermost Eocene in the Basque Basin, Western Pyrenees.,” *Munibe. Ciencias Nat.*, vol. 46, pp. 43–62, 1994.

[173] H.-J. Wang, A. Mutina, and R. Kausik, “High field nuclear magnetic resonance observation of gas shale fracturing by methane gas,” *Energy & Fuels*, p. 140423081101009, 2014.

[174] P. L. Kenfack, P. Ricard, N. Ngaha, G. E. Ekodeck, and G. Ngueutchoua, “Mineralogic Characterization and Petroleum Potential of Clays (Shales) of the N ’ Kapa Formation (Paleocene-Eocene) in the Douala Sedimentary,” vol. 2012, no. September, pp. 696–709, 2012.

[175] International Gas Union, “Shale Gas: The Facts about the Environmental Concerns,” *International Gas Union*, 2012. [Online]. Available: http://www.igu.org.

[176] V. P. Nguyen, H. Lian, T. Rabczuk, and V. Phu, “Modelling hydraulic fractures in porous media using flow cohesive interface elements,” *Eng. Geol.*, vol. In Press, 2017.

[177] G. Hattori, J. Trevelyan, C. E. Augarde, W. M. Coombs, and A. C. Aplin, “Numerical Simulation of Fracking in Shale Rocks : Current State and Future Approaches,” *Arch. Comput. Methods Eng.*, vol. 24, no. 2, pp. 281–317, 2017.

[178] X. Lei, S. Zhang, T. Guo, and B. Xiao, “New Evaluation Method of the Ability of Forming Fracture Network in Tight Sandstone Reservoir,” *Int. J. Environ. Sci. Dev.*, vol. 6, no. 9, pp. 688–692, 2015.

[179] N. Recho, *Fracture Mechanics and Crack Growth*. 2012.

[180] L. S. M. A. Al-ansari, “Calculating Stress Intensity Factor (Mode I) for Plate with Central Crack : Review and Comparison between Several Techniques of Calculations,” *Asian Trans. Eng.*, vol. 2, no. 5, pp. 44–56, 2012.

[181] M. Bak, “Fracture Mechanics Using Workbench,” no. July. CAE Associates, 2013.

[182] K. N. Hoque, “Analysis of structural discontinuities in ship hull using finite element method,” 2016.

[183] shale gas information platform, “The Basics - Water Protection.” [Online]. Available: http://www.shale-gas-information-platform.org/categories/water-protection/the-basics.html.

[184] B. Hansen, “Casing Perforating Overview,” *Devon Energy Corporation*. .

[185] E. Rybacki, A. Reinicke, T. Meier, M. Makasi, and G. Dresen, “What controls the mechanical properties of shale rocks? ? Part I: Strength and Young’s modulus,” *J. Pet. Sci. Eng.*, vol. 135, pp. 702–722, Nov. 2015.

[186] T. A. Stolarski, Y. Nakasone, and S. Yoshimoto, *Engineering Analysis With ANSYS Software*. Elsevier Butterworth-Heinemann, 2006.